Quantitative Analysis of Ocular Microcirculation Images in Human Health and Disease

BY

MAZIYAR MOHAMMADTALAB KHANSARI
M.S., University of Illinois at Chicago, 2014
B.S., Azad University, 2010

THESIS

Submitted as partial fulfillment of the requirements
for the degree of Doctor of Philosophy in Bioengineering
in the Graduate College of the
University of Illinois at Chicago, 2017

Chicago, Illinois

Defense Committee:

Prof. Mahnaz Shahidi, Advisor, Ophthalmology & Visual Sciences
Prof. Norman P. Blair, Ophthalmology & Visual Sciences
Prof. William O'Neill, Chair, Bioengineering
Prof. Thomas Royston, Bioengineering
Prof. Richard Penn, Bioengineering

AKNOWLEDGMENTS

I would like to express my sincere gratitude to my advisor Prof. Mahnaz Shahidi for the continuous support of my PhD study and related research, knowledgeable advices, motivation and patience. I also want to thank my thesis committee (Dr. William O'Neill, Dr. Norman P. Blair, Dr. Richard Penn and Dr. Thomas Royston) for their unwavering support and assistance. Their guidance and insights have significantly helped me accomplish my research goals and become an effective researcher. Furthermore, I would like to thank the staff at the department of ophthalmology and visual sciences at the University of Illinois at Chicago, who have helped me with data collection and worked tirelessly to meet the deadlines. Finally, I would like to thank my family: my parents Aniss and Sobhan, my sister Shahrzad without whom this work would have been impossible.

MK

CONTRIBUTIONS OF AUTHORS

Specific contributions made by authors for parts of the current thesis which have been published in peer-reviewed journals were as following.

- Khansari, Maziyar M., Justin Wanek, Anthony E. Felder, Nicole Camardo and Mahnaz Shahidi. "Automated assessment of hemodynamics in the conjunctival microvasculature network." IEEE transactions on medical imaging 35, no. 2 (2016): 605-611.

  M. Khansari: Concept/design, data collection, data analysis/interpretation, manuscript preparation.

  J. Wanek: Concept/design, data collection, manuscript preparation.

  AE. Felder: Concept/design, Data collection.

  N. Camardo: Data collection.

  M. Shahidi: Concept/design, data collection, data analysis/interpretation, manuscript preparation.

- Khansari, Maziyar M., Justin Wanek, Michael Tan, Charlotte E. Joslin, Jacob K. Kresovich, Nicole Camardo, Norman P. Blair and Mahnaz Shahidi. "Assessment of Conjunctival Microvascular Hemodynamics in Stages of Diabetic Microvasculopathy." Scientific Reports 7 (2017).

  M. Khansari: Concept/design, data collection, data analysis/interpretation, manuscript preparation.

  J. Wanek: Concept/design, data collection, manuscript preparation.

M. Tan: Data collection.

C.E. Joslin: Data analysis/interpretation.

J.K. Kresovich: Data analysis/interpretation.

N. Camardo: Data collection.

N. P. Blair: Data analysis/interpretation, manuscript preparation.

M. Shahidi: Concept/design, data analysis/interpretation, manuscript preparation.

- Khansari, Maziyar M., William O'Neill, Richard Penn, Felix Chau, Norman P. Blair and Mahnaz Shahidi. "Automated fine structure image analysis method for discrimination of diabetic retinopathy stage using conjunctival microvasculature images." Biomedical optics express 7, no. 7 (2016): 2597-2606.

  M. Khansari: Concept/design, data collection, data analysis/interpretation, manuscript preparation.

  W. O'Neill: Concept/design, manuscript preparation.

  R. Penn: Manuscript preparation.

  F. Chau: Data Collection.

  N. P. Blair: Data analysis/interpretation, manuscript preparation.

  M. Shahidi: Concept/design, data analysis/interpretation, manuscript preparation.

- Maziyar M., Khansari, William O'Neill, Jennifer Lim and Mahnaz Shahidi. "Method for quantitative assessment of retinal vessel tortuosity in optical coherence

tomography angiography applied to sickle cell retinopathy." Biomedical Optics Express 8, no. 8 (2017): 3796-3806.

M. Khansari: Concept/design, data collection, data analysis/interpretation, manuscript preparation.

W. O'Neill: data analysis/interpretation, manuscript preparation.

J. Lim: Manuscript preparation

M. Shahidi: Concept/design, data analysis/interpretation, manuscript preparation.

TABLE OF CONTENTS

LIST OF TABLES

LIST OF TABLES (continued)

LIST OF TABLES (continued)

LIST OF FIGURES

LIST OF FIGURES (continued)

LIST OF FIGURES (continued)

LIST OF FIGURES (continued)

LIST OF FIGURES (continued)

LIST OF FIGURES (continued)

LIST OF FIGURES (continued)

LIST OF ABBREVIATIONS

2D	Two Dimensions
CCD	Charged Coupled Device
CI	Confidence Interval
D	Diameter
DBP	Diastolic Blood Pressure
DR	Diabetic Retinopathy
DM	Distance Measure
FA	Fluorescein Angiography
FAZ	Foveal Avascular Zone
FLD	Fisher's Linear Discriminate
FWHM	Full Width at Half Maximum
GLMM	Generalized Linear Mixed Model
HbA1c	Glycated Hemoglobin
HCT	Hematocrit
HR	Heart Rate
Ip	Inflection Points
KLD	Kullback-Leibler Divergence
KS	Kolmogorov-Smirnov
LA	Centerline Length
LC	Chord Length
MAP	Mean Arterial Pressure
MRI	Magnetic Resonance Imaging
NC	Normal Control
NDR	No Diabetic Retinopathy
NPDR	Non-Proliferative Diabetic Retinopathy
OCT	Optical coherence Tomography
OCTA	Optical Coherence Tomography Angiography
OLS	Ordinary Least Square
PDR	Proliferative Diabetic Retinopathy
Q	Blood Flow
RBC	Red Blood Cell
ROI	Region of Interest
SBP	Systolic Blood Pressure
SCD	Sickle Cell Disease
SCR	Sickle Cell retinopathy
SD	Standard Deviation
STI	Space Time Image
TSA	Time Series Analysis
V	Axial Blood Velocity
VEGF	Vascular Endothelial Growth Factor
VTI	Vessel Tortuosity Index
WSR	Wall Shear Rate
WSS	Wall Shear Stress

SUMMARY

The vascularized ocular tissues are conjunctiva which covers the outer layer of the eye and the retina which is located in the back of the eye. Conjunctival microvascular hemodynamic alterations due to systemic and vascular diseases have been reported. However, previous qualitative or semi-automated methods were limited for quantifying hemodynamics in a large number of vessels within the microvascular network. Due to the high physiological variability and vessel density, there is a need for an automated image processing technique for quantitative and comprehensive assessment of hemodynamics in the conjunctival microvascular network. Additionally, assessment of alterations in the conjunctival and the retinal vascular pattern provides a means for computerized disease diagnosis and discrimination. Techniques have been developed for discriminating systemic and ocular diseases using retinal vascular images. Nevertheless, a method for discriminating stages of disease based on conjunctival microvascular images has not been reported previously. Finally, increased retinal vessel tortuosity is known to be among early indicators of various retinopathies. However, previous techniques for quantitative assessment of retinal vessel tortuosity are limited in that their findings are not always consistent with the visual perception of tortuosity or might be scale dependent. Therefore, the goal in this research study was to develop and apply image processing techniques for detection of hemodynamic, vascular pattern, and morphological alterations due to systemic and vision-threatening diseases.

I. INTRODUCTION

Conjunctiva is a densely vascularized tissue located on the surface of the eye and is available for non-invasive imaging. Direct visualization of human microcirculation within the conjunctival arterioles and venules have provided a means for studying hemodynamic alterations due to systemic and vision-threatening diseases (1-9). Current available methods for assessment of conjunctival microvascular hemodynamics are semi-automated which may be subjective and not efficient for quantifying large number of microvessels within the network (10-14). Therefore, quantitative and automated techniques that can provide comprehensive assessment of conjunctival microvascular network can be useful to better understand pathophysiology of the tissue in health and disease. Additionally, studying intra-visit and inter-visit variability of conjunctival microvascular hemodynamics is crucial to determine sensitivity of the measurements for discriminating between true alterations from random fluctuations. Intra-visit variability of conjunctival microvascular hemodynamics was reported (15). Nevertheless, no previous study has reported inter-visit variability of the hemodynamics under health and disease conditions.

Previous studies of conjunctival microcirculation in diabetic subjects showed alterations such as vasodilation, abnormal blood flow and hemorrhages in the microvascular network (8, 9, 16-18). In fact, majority of previous studies determined a severity index (SI) based on presence of hemodynamic alterations in the conjunctival microvasculature of diabetes subjects. Indeed, it was shown that the SI is useful for diagnosis and monitoring of the disease (8, 9, 17). However, hemodynamic alterations in

the conjunctival microvascular network at progressive stages of diabetic retinopathy (DR) have not been reported previously.

This thesis presents an automated image processing method for quantitative and comprehensive assessment of hemodynamics in the conjunctival microvascular network. The method provided measurements of microvascular diameter (D), blood velocity (V), blood flow (Q), wall shear rate (WSR) and wall shear stress (WSS) in different size microvessels. Furthermore, inter-visit variability of conjunctival hemodynamic measurements in normal and subjects with clinical DR was studied using the automated method. Finally, the method was utilized for detecting conjunctival microvascular hemodynamic alterations at stages of increasing diabetic microvasculopathy based on DR.

Recently, a method was proposed providing fine structure analysis of brain magnetic resonance imaging (MRI) images and performed better than specialists in discriminating subjects with dementia from normal controls (NC) (19). The method provided an opportunity for discriminating DR stage based on ocular images. In diabetic subjects, discrimination of DR stages using conjunctival microvascular images have not been reported, instead images of retinal vasculature have been mainly used for detecting stages of DR (20-25). Additionally, the automated method can become useful for discrimination of subclinical DR based on retinal images since no specific microvasculopathies are directly visible at this stage.

We will validate in this thesis, application of the fine structure analysis for classification of conjunctival microvascular images and utilized it for automatic DR stage

discrimination. Additionally, performance of the method was compared against experienced retinal specialists for discriminating stages of DR based on conjunctival microvascular images. Finally, the fine structure analysis method was used for detecting subclinical DR from retinal images.

Retinal vessel tortuosity alteration is among early signs of many retinopathies including DR and retinopathy of prematurity (26). Additionally, previous studies have shown increased tortuosity in the retinal vasculature due to various pathologies (27-31), and correlation between retinal vascular tortuosity and demographics such as age and hematocrit (HCT) level (32). Nevertheless, available tortuosity indices may be scale dependent or do not always match with visual perception of tortuosity (33). Additionally, quantitative assessment of retinal vessel tortuosity alterations due to sickle cell retinopathy (SCR) in the parafoveal and perifoveal regions based on optical coherence tomography angiography (OCTA) has not been reported previously.

In this thesis, we developed and validated a novel vessel tortuosity index (VTI) by extracting local and global featured from retinal vessel centerlines. Variation of local angle changes, number of critical points, ratio of vessel length to its chord length for the entire vessel and between the inflection points (Ip) were used for VTI computation. An image processing pipeline was developed for VTI quantification in retinal vasculature imaged by OCTA and was used for detecting tortuosity alterations in the parafoveal and perifoveal regions due to SCR.

II. BACKGROUND

1. Conjunctiva

Conjunctiva is located on the surface of the eye and covers the sclera as shown in Figure 2.1 (Left). The main function of the conjunctiva is lubricating the eye through production of mucus and tears. Additionally, the conjunctiva contributes to the immune system by precluding entrance of microbes into the eyes. The blood supply to the conjunctiva is provided primary by the ophthalmic artery and/or external carotid artery (34). The tissue is densely vascularized and easily accessible for studying of human microcirculation. Conjunctival microvasculature can be categorized into arterioles, venules and capillaries based on direction of blood flow, providing an opportunity for studying each one independently. In fact, the tissue is one of the limited locations through the body that can provide direct visualization of capillary beds. Figure 2.1 (Right) shows example image of conjunctival microvascular image in a NC subject.

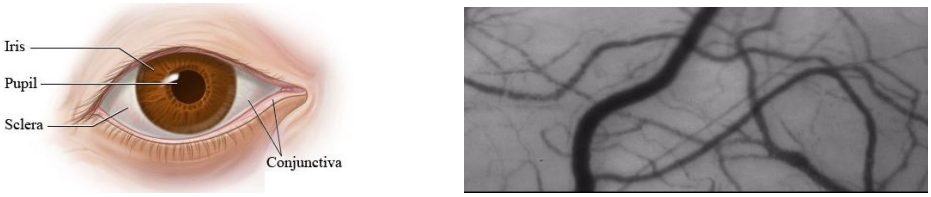

Figure 2.1. Schematic view of the eye displaying location of the conjunctiva on the surface of the eye (Left) (acquired from https://myhealth.alberta.ca). Example of conjunctival microvasculature image in a healthy human subject (Right).

2. Conjunctival Microvascular Hemodynamics

Conjunctival microcirculation can be readily assessed due to ease of accessibility of the tissue. The primary hemodynamic descriptors of the conjunctival arterioles and venules are D and V. It was shown previously that D can be reliably measured using full width at half maximum (FWHM) of intensity profiles, established perpendicular to the vessel centerline (13). As described previously, V can be determined by tracking movement of red blood cells (RBC) along the vessel centerline across registered image sequences using spatial-temporal image (STI) technique (13). The STI shows variation of intensity values along the centerline over time due to RBC movements. The slope of prominent bands in the STI can be used to determine V.

Based on the measurement of D and V, average cross-sectional velocity (V_s) can be calculated as shown in Equation (2.1) (35, 36). Erythrocytes deform by passing through narrow capillaries when the ratio of D to RBC diameter (D_c) is equal to 0.6, and hence allows considering equal values for V and V_s (37). The same consideration can be made for microvessels with smaller D to the point that erythrocytes cannot pass through the microvessel. However, for larger diameter microvessels, V_s can be approximated based on experimental studies that were described elsewhere (36, 37).

$$V_s = \begin{cases} V & \frac{D}{D_c} \leq 0.6 \\ 1.58\left(\frac{V}{1-e^{-\sqrt{\frac{2D}{D_c}}}}\right) & \frac{D}{D_c} > 0.6 \end{cases} \tag{2.1}$$

Based on D and V_s, Q and WSR can be computed as shown in Equations (2.2) and (2.3), respectively. Finally, WSS can be determined based on Equation (2.4) by considering the effect of blood dynamic viscosity (η) (13, 38).

$$Q = V_s \frac{\pi D^2}{4} \tag{2.2}$$

$$WSR = \frac{8V_s}{D} \tag{2.3}$$

$$WSS = \eta WSR \tag{2.4}$$

Therefore, using fluid dynamics equations and experimental results from previous studies (36, 37), conjunctival microvascular hemodynamics can be assessed providing quantitative information regarding microcirculation within the network.

3. Retina

The retina is part of the brain which lies on the back of the eye and contains multiple cell layers (39). Choroid layer is behind the retina and contains a vasculature network for oxygen and nutrition delivery to the tissue. The pigment epithelium layer is attached to the choroid and contains a single layer of cells. This layer provides nutrition and remove wastes from photoreceptor cells which are responsible for converting the light into electrical signal. The horizontal cell layer is connected to the photoreceptors to improve integration of the information from multiple photoreceptors, and hence improves the visual acuity. Bipolar cell layer is located beneath the horizontal cells to pass the information from photoreceptors to other retinal layers. Finally, ganglion layer is located near the retinal surface. Cells at this layer extend to form optic nerves and transfer the information to the brain. Figure 2.2, shows a sagital and a coronal views of human eye

displaying locations of the retina and the optic nerve head. The retina is a highly metabolic tissue requiring high level of nutrition and oxygen to be delivered by its vasculature (42). In fact, the tissue has the highest oxygen consumption rate through the body and disruption in blood supply to the retina will result in vision loss within a few minutes (43). Blood supply to retina is provided mainly through choroidal blood vessels and the central retinal artery from the optic nerve head (40, 41). Studying retinal vasculature and metabolism can increase our understanding of systemic and vision-threatening diseases, provide diagnostic biomarkers and contribute to development of new therapeutic treatments (44).

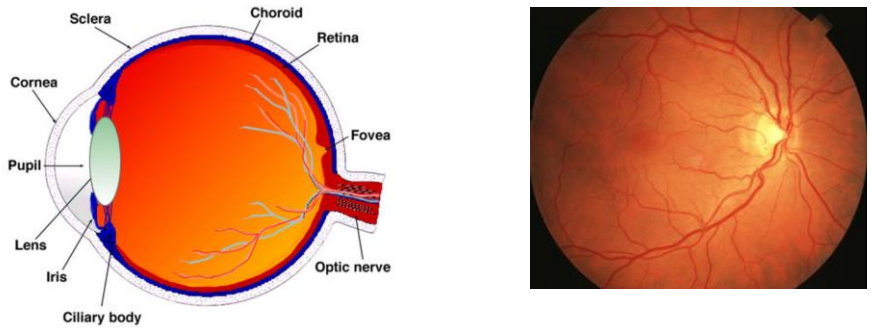

Figure 2.2. Gross anatomy of the eye with major tissues labeled (Left) (acquired from http://webvision.med.utah.edu/book/part-i-foundations/gross-anatomy-of-the-eye). Coronal view of the retina displaying retinal vasculature and optic nerve head (Right) (acquired from Retinal STARE database).

4. Fine Structure Analysis

Fine structure analysis is an automated image discrimination method based on mathematical and statistical models (19). The method was described previously and showed good potential for dementia detection based on brain MRI images. The method uses all the information in the image rather than specific alteration which makes it suitable for diagnosis of diseases in which specific alterations are not readily visible by conventional clinical means. Images are considered as solutions to partial differential equations such as the one in Equation (2.5). Additionally, an ordinary least square (OLS) format of the equation can be obtained by using a Kronecker matrix-to-vector transformation (45). Therefore, pixels of each image were shifted by 1 or 2 pixels row-wise, column-wise and along the diagonal to provide 8 unique combination of the raw image. Each of the shifted images was vectorized to create a 1D vector and formed one column of a matrix. A model image ($y_{i,j}$) was defined as weighted sum of the shifted images as shown in Equation (2.5).

$$y_{i,j} = \sum_{k=0}^{2} \sum_{l=0}^{2} b_{k,l} y_{i-k,j-l} + u_{i,j} \tag{2.5}$$

where $y_{i,j}$ is the modeled image, $y_{i-k,j-l}$ are the shifted images, b_{kl} are coefficients to be estimated, and $u_{i,j}$ is a 2D random process error with zero mean. The OLS regression was performed to compute coefficients b_{kl} by minimizing the variance of $u_{i,j}$.

Computed OLS coefficients for images in each group were assembled into matrices. Fisher's Linear Discriminate (FLD) analysis was performed to compute a projection vector (v) which projects b_{kl} parameters of each image onto a scalar z-projection axis. The maximum separation of sample means of projections was obtained

with v which satisfied the FLD eigenvector identity (46). For 2 comparison groups of images, N_1 and N_2 subjects, let their respective OLS coefficients be assembled in matrices B_1 and B_2. The "pooled sample" or combined matrix B_p is B_1 stacked on B_2. For an n by k matrix B with n samples of k parameters let B_m be B with its column sample means subtracted. Then the estimated covariance matrix of B is $\Omega = B_m^T B_m/(n-1)$. The optimizing projection vector v satisfies the eigenvector identity of the B_1, B_2, and B_p covariance matrices was computed using Equation (2.6).

$$(n_1\Omega_p - n_2\Omega_1 - n_3\Omega_1)v = \Upsilon_1(n_2\Omega_1 + n_3\Omega_2)v \tag{2.6}$$

where γ_1 is the only non-zero eigenvalue, $n_1 = N_1+N_2-1$, $n_2 = N_1-1$, and $n_3 = N_2-1$. The FLD vector v maximizes the absolute difference between the sample means of 2 groups normalized by the sum of the covariance of each group.

The Kolmogorov–Smirnov (KS) test was used to verify that z-projections in each group were normally distributed (46), hence allowing the use of Kullback-Leibler discrimination (KLD) statistics which is a special case of the Neyman-Pearson log-likelihood ratio hypothesis test. Applied to 2 normally distributed z-projection density functions, $f_1(z)$ and $f_2(z)$, KLD statistics are values of a discrimination function L(z) given by Equation (2.7).

$$L_{1,2}(z) = \text{Ln}\left(\frac{f_1(z)}{f_2(z)}\right) = \text{Ln}\left(\frac{s_2}{s_1}\right) + \frac{(z-m_2)^2}{2s_2^2} - \frac{(z-m_1)^2}{2s_1^2} \tag{2.7}$$

where m_i and s_i, i = 1,2 are sample means and standard deviations (SD) of the hypothesized z-projection distributions. If the groups are perfectly separated, L1 values for all cases in group 1 will be positive and L2 values for all cases in group 2 will be

negative and $L_{2,1} = -L_{1,2}$. Misclassified group 1 z-projections have negative L1 values and misclassified group 2 z-projections have positive L2 values. The larger L1 value is for a group 1 the more likely it is a true positive and the smaller L2 value is for a group 2 the more likely it is a true negative. In this thesis, the fine structure analysis was used for discrimination of stages of DR based on conjunctival and retinal vascular images.

5. Tortuosity

Retinal vessels are generally straight or mildly curved in normal subjects. However, under certain pathologies, the vessels become twisted with many turns (26). It was shown previously that tortuosity is among early alterations due to many retinopathies such as DR and hypertension (27, 33). Figure 2.3, shows examples of retinal vasculature in a NC and a subject with DR, depicting presence of tortuous retinal vasculature due to the disease. Studies of tortuous vessels have been reported qualitatively which are limited due to subjectivity and high inter-observer variability (47). Therefore, quantitative methods are invoked to summarize information regarding tortuosity of retinal vessels.

Quantitative measures of retinal vessel tortuosity have been performed on vessel centerlines by applying mathematical formula to extract information (26-31, 33, 48, 49). Regardless of the approach, any tortuosity index needs to correlate with visual perception of tortuosity. It should be invariant to rigid transformations such as rotation, scaling and mirroring. Also, a quantitative measure of tortuosity should increase with increase in magnitude and increase in frequency of centerline twists.

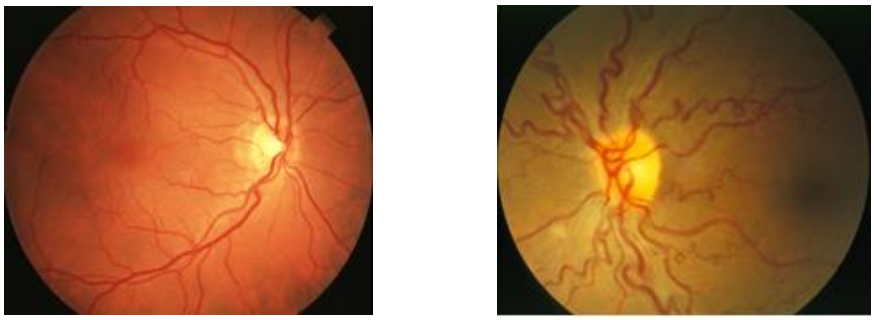

Figure 2.3. Examples of retinal vasculature in a NC (Left) and a subject with DR (Right) displaying presence of highly tortuous vessels due to the pathology.

Figure 2.4 shows chord length of a simulated vessel centerline and location of Ip and critical points that can be used to summarize information regarding tortuosity of the centerline. The distance measure (DM) as shown in Equation (2.8) is the ratio of centerline length (L_A) to chord length (L_C) of a vessel segment, and has been widely used for detection of tortuosity alterations (50-52). Methods based on combination of DM and number of Ip have been proposed as shown in Equations (2.9) and (2.10) to improve DM and provide a more reliable tortuosity index (33, 53).

$$DM = \frac{L_A}{L_C} \tag{2.8}$$

$$ICM = (Ip + 1)\frac{L_A}{L_C} \tag{2.9}$$

$$T = \frac{Ip-1}{Ip}\sum_{i=1}^{Ip}\left[\frac{L_{A_{si}}}{L_{C_{si}}} - 1\right] \tag{2.10}$$

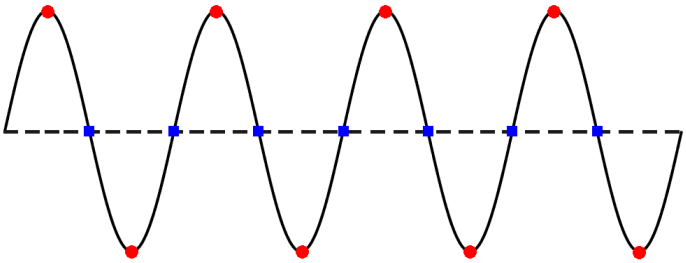

Figure 2.4. An example of a simulated vessel centerline displaying vessel chord (dashed line), location of critical points (red circle) and locations of inflection point (blue squares) that can be used to summarize information regarding tortuosity of retinal vasculature.

Examples of tortuosity indexes based on integral of curvature are shown in Equations (2.11) and (2.12), indicating integral measures of k over D domain as representative of variations in the direction of vessels (26, 54).

$$T_C = \int_{\min(D)}^{\max(D)} |k(l)| dl \tag{2.11}$$

$$DCI = \int_{\min(D)}^{\max(D)} \left|\frac{d_k(l)}{dl}\right|^2 dl \tag{2.12}$$

Finally, tortuosity indices based on sum of changes in the angles between centerline points are shown in Equations (2.13) and (2.14) (55, 56). N in Equation (2.13) is number of sample points, n and θ are predefined fixed factor and the angle between lines connecting consecutive pairs of sample points, respectively.

$$MAC = \frac{1}{N-2n} \sum_{i=1}^{n} \theta\,(i) \tag{2.13}$$

$$TN = \sum_{i=1}^{n} (\theta \geq \frac{\pi}{6}) \tag{2.14}$$

Tortuosity can also be calculated based on combination of local and global features to better match with observer's perception of tortuosity. For example, combination of number of critical points and angle variations with DM can potentially provide a more sensitive measure of tortuosity while remaining invariant to rigid transformations. Such an approach has been thought to be useful for detection of tortuosity alterations in diseases such as SCR, in which nonspecific tortuosity alterations were reported previously (57, 58). It is important to note that quantification of retinal vessel tortuosity has been mainly performed based on 2D images. However, tortuosity includes curvature in z direction which cannot be readily determined due to limitation of 2D image acquisition.

III. QUANTITATIVE AND COMPREHENSIVE ASSESSMENT OF HEMODYNAMICS IN THE CONJUNCTIVAL MICROVASCULAR NETWORK AND INTER-VISIT VARIABILITY OF THE HEMODYNAMIC MEASUREMENTS

1. An Automated Image Processing Technique for Quantitative and Comprehensive Assessment of Hemodynamics in the Conjunctival Microvascular Network

The contents of this chapter have been published as: Khansari, Maziyar M., Justin Wanek, Anthony E. Felder, Nicole Camaro and Mahnaz Shahidi. "Automated assessment of hemodynamics in the conjunctival microvasculature network." IEEE transactions on medical imaging, 35, no. 2 (2016): 605-611.

Introduction

The bulbar conjunctiva is a densely vascularized tissue covering the sclera of the eye. It is one of a limited number of locations in the human body where RBC movement within the microcirculation can be directly and non-invasively visualized. Due to this characteristic, the conjunctival microcirculation has been utilized to assess microvascular alterations due to systemic disorders, such as sickle cell disease (1-4), Alzheimer's disease (5), hypertension (6), hypotension (7), and diabetes mellitus (8, 9). Furthermore, previous studies have found correlations between conjunctival microvascular hemodynamics and cerebral blood flow in dogs (59), and alterations in the conjunctival

microcirculation in subjects with unilateral stroke (60), and during internal carotid artery surgery (61). Hence, quantification of conjunctival microvasculature hemodynamics may be of value for evaluating microvascular alterations in other tissues of the body.

Several commercial instruments designed for evaluation of the retinal circulation have been modified for assessment of hemodynamic properties of the conjunctival microvasculature, including the Heidelberg Retinal Flowmeter (10), and Retinal Functional Imager (11). However, these instruments do not provide absolute measurements of retinal blood flow (10), or evaluate vessel caliber (11). Other techniques such as Orthogonal Polarization Spectral Imaging (12), slit lamp biomicroscopy (13, 14, 36), and intravital microscopy (3, 62), utilize semi-automated image analysis algorithms to measure blood velocity and diameter of microvessels, but require selection of vessels of interest, which may be subjective and time consuming.

Due to the large number of microvessels and physiologic variability of blood flow in the conjunctival microvascular network, there is a need for an automated image analysis method to comprehensively and quantitatively assess hemodynamics. Recently, a study evaluating the number of vessels required to reliably characterize the hemodynamic properties of the conjunctival microvasculature was published, reporting the need to obtain measurements in more than 15 venules (63). In the current study, a fully automated algorithm is reported that provides a comprehensive hemodynamic assessment of the conjunctival microvascular network.

Materials and Methods

Subjects

The study was approved by an institutional review board of the University of Illinois at Chicago. The study was explained to subjects and informed consents were acquired in accordance to tents of Declaration of Helsinki. Conjunctival microvasculature imaging was performed in 15 healthy subjects (age; was 61±11 years) without any history of ocular or systemic diseases. Each subject contributed to the study by one eye which was selected based on availability and quality of the images. Subjects were seated while their head and chin were stabilized using a head and a chin support. An external fixation target was introduced to the fellow eye to minimize eye movement during image acquisition. Imaging was performed at several temporal conjunctival regions. In a separated group of 5 subjects, repeated imaging was performed in one conjunctival region.

Image acquisition

Conjunctival microvascular imaging was performed using a previously described non-invasive optical imaging instrument (EyeFlow) (13). The system comprised a slit lamp biomicroscope coupled to a digital charged coupled device (CCD) camera (Prosilica GT, AVT, Exton, PA) for recording RBC movement within conjunctival microvasculature. The magnification of the system was 5.1X and the camera active sensor size was 8.8 mm×6.6 mm. The fill factor and quantum efficiency were 100% and approximately 50%, respectively. The conjunctiva was illuminated using an external

light source passed through a green filter with a wavelength of 540 nm. Several 1-second image sequences were acquired at a rate of 50 frames per second and an exposure of 20 ms. Each image consisted of 1360×550 pixels where each pixel was equal to 1.25 μm on the object plane.

Image processing and analysis

The automated method for assessment of conjunctival microvascular images consisted of multiple image processing steps as shown in Figure 3.1.1. In summary, image registration was performed to compensate for eye movement, image segmentation was performed for vessel detection, centerline extraction and bifurcation detection was used for identifying individual vessel segments. Finally, diameter measurement, blood flow detection, and axial blood velocity measurement were performed for each vessel segment. The image processing steps were implemented in MATLAB (release 2014a, Mathworks, Inc., Natick, MA, USA) with image processing toolbox version 9.0. Detail description of each step is provided in the following.

Image Registration

Image sequences were processed to remove frames corresponding to blinks and correct for eye movement by image registration. Image frames were first examined for the presence of saturated pixels, which were removed by automated cropping of the image frames to the largest rectangular area with non-saturated pixels. For each image, a sharpness score was quantified by calculating the average magnitude of the horizontal and vertical intensity gradients, which were calculated by determining pixel-to-pixel intensity changes. To eliminate frames with insufficient sharpness due to blinks and

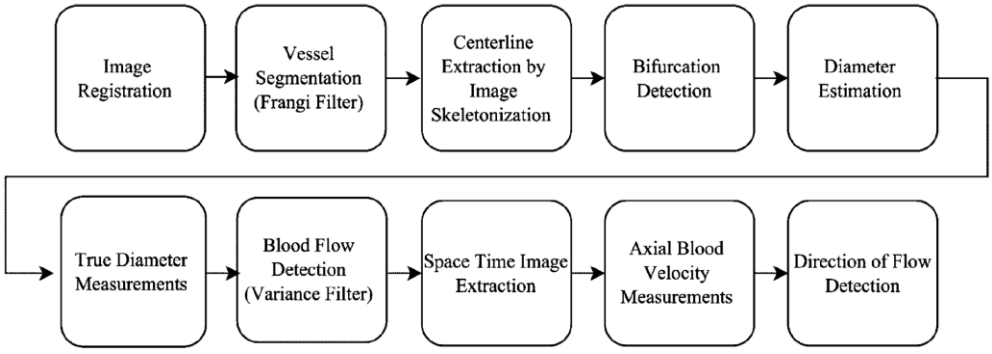

Figure 3.1.1. Flow chart depicting steps for automated image registration, vessel segmentation and hemodynamic measurements of the conjunctival microvascular network.

rapid eye motion, the longest consecutive series of image frames that had sharpness scores above a threshold were extracted. This threshold was computed for each image sequence as the mean minus half the SD of the sharpness scores. A reference frame was then assigned based on the highest sharpness score and the remaining frames were automatically registered to this frame by translation using the MATLAB function *imregister*. This intensity-based image registration function uses an optimization algorithm to find the best transform to align 2 images. The minimum and maximum numbers of consecutive automatically registered image frames were 6 and 40, respectively.

Vessel Segmentation

Vessel segmentation was performed using Frangi filtering on the time-averaged image generated from the registered images. This filtering method involved computing

eigenvalues of the Hessian matrix over multiple image scales σ_{min} and σ_{max} (blur levels) for the detection of vessel-like structures within the image, as described previously (64). Briefly, a vesselness measure (V_o) was derived for each pixel based on the normalized and sorted eigenvalues (λ_1 and λ_2) of the Hessian matrix computed over multiple image scales (σ) as shown in Equation (3.1.1).

$$V_0(\sigma) = \begin{cases} 0 & \text{if } \lambda_2 > 0 \\ \exp\left(-\frac{R_B^2(\sigma)}{2\beta^2}\right) & \left(1 - \exp\left(-\frac{S^2(\sigma)}{2C^2}\right)\right) \end{cases} \quad (3.1.1)$$

where $R_B(\sigma) = \lambda_1(\sigma)/\lambda_2(\sigma)$, $S(\sigma) = (\lambda_1(\sigma) + \lambda_2(\sigma))^{0.5}$, and β and C were constants set to the value of 1. A vesselness image was then generated by assigning the maximum vesselness measure over the image scales to each pixel, as indicated in Equation (3.1.2).

$$V_0 = \text{MAX}_{\sigma_{min} \le \sigma \le \sigma_{max}} \{V_0(\sigma)\} \quad (3.1.2)$$

To eliminate user interaction, the minimum (σ_{min}) and maximum (σ_{max}) image scales were set to 1 and 7, respectively. To increase computation efficiency, σ varied between σ_{min} and σ_{max} using only odd values. By varying σ in steps of 2 rather than 1, the computation time for Frangi filtering was reduced by approximately a factor of 2. The vesselness image was then binarized using an empirically derived threshold value of 0.1, thereby providing segmentation of the conjunctival vessels. This binary image was further processed by counting the number of connected pixels in each binary object and removing objects smaller than 50 pixels in size. To fill holes in the vessels and smooth edges, a single step morphological closing operation was also performed using a disk shape structuring element with a radius of 4 pixels.

An example of a mean conjunctival microcirculation image, derived by averaging 12 registered images is shown in Figure 3.1.2A. Vessel segmentation results obtained by Frangi filtering using a threshold of 0.1 and the minimum and maximum image scales of 1 and 7, respectively, are shown in Figure 3.1.2B. The final binary image after removing small objects and morphological closing is shown in Figure 3.1.2C. As shown in Figure 3.1.2, Frangi filtering was able to detect small and large caliber microvessels of the conjunctival microvasculature.

Centerline Extraction and Bifurcation Detection

To extract centerlines and detect bifurcations of the vessel segments, several steps were performed. An iterative morphological thinning algorithm (65), was used to create a skeleton image by shrinking the segmented vessels to single lines corresponding to the centerlines of the vessel segments. Small spurs created during the thinning procedure were removed by determining the number of connected neighbor pixels in a 3×3 kernel for each pixel in the centerline. The spurs were removed by repeatedly (20 times) eliminating pixels that only had one connected neighbor, thereby removing spurs less than 20 pixels in length. A value of 20 pixels was selected since this is approximately equal to the radius of the largest conjunctival vessels, and the length of spurs should not exceed the radius of the vessels. Intersection points of the vessel centerlines at crossovers and bifurcations were detected to obtain the centerlines associated with each vessel segment. The intersection points were found by first performing convolution of the skeleton image with a 3×3 unity kernel, then multiplying the result by the skeleton image and detecting pixel locations that had a value greater than

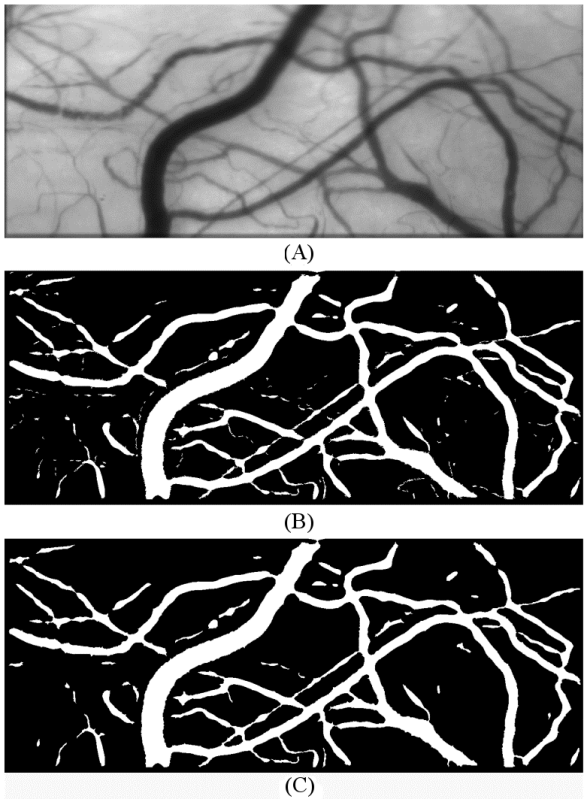

Figure 3.1.2. (A) Mean conjunctival microcirculation image generated by averaging consecutive registered image frames; (B) Vessel segmentation by Frangi filtering of the mean image. (C) After removing small objects and a morphological closing operation.

three (66). Finally, centerlines of the vessel segments were labeled automatically based on the number of connected pixels of each centerline. The lengths of the vessel segments were between 21 and 1078 pixels.

Images of the conjunctival microcirculation displaying the detected centerlines after morphological thinning and spur removal are shown in Figure 3.1.3A and Figure 3.1.3B, respectively. Vessel intersection and bifurcation points are displayed in Figure 3.1.3C. In this example, 45 vessel segments in the conjunctival network were identified

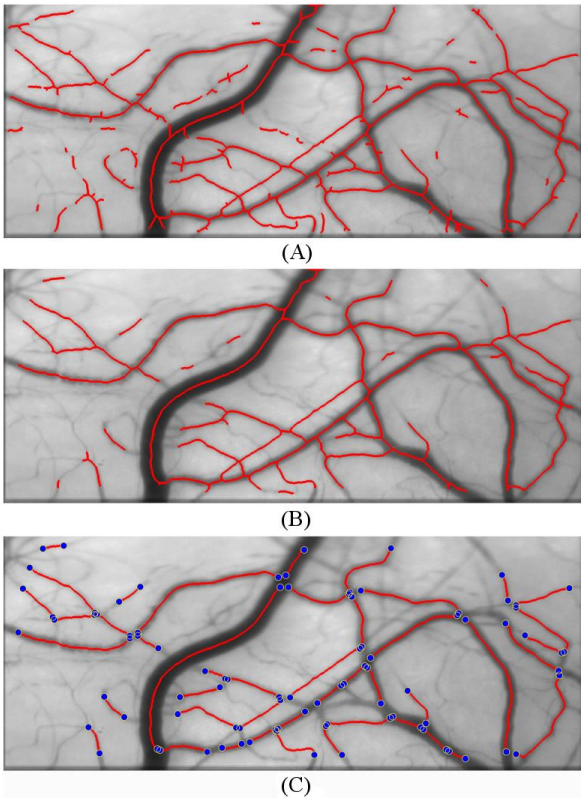

Figure 3.1.3. Conjunctival microcirculation image displaying detected centerlines after (A) morphological thinning, (B) spur removal, (C) detection of bifurcations and intersection points (blue dots).

after centerline extraction and bifurcation detection. Hemodynamic properties of the vessel segments were then evaluated individually, as described below.

Diameter Measurement

Diameter (D) and boundaries of vessel segments were automatically determined by calculating the FWHM of intensity profiles of lines perpendicular to the vessel centerline, as previously described (67). For each vessel segment, the length of the

perpendicular lines was set to 3 times an approximated vessel diameter value, which ensured the perpendicular lines extended beyond the vessel walls by approximately 1 diameter length in both directions. The approximated vessel diameter was determined by plotting 3 perpendicular lines with a length of 80 pixels (100 microns) at 3 equally spaced points along each vessel centerline on the final binary image. The perpendicular lines were established automatically by calculating the line normal to the centerline direction, which was determined based on linear regression of 5 local vessel centerline points. The perpendicular line was computed by the negative inverse of the slope of the best fit regression line. The number of pixels (length) on the 3 perpendicular lines within the vessel segment on the binary image were counted using Bresenham algorithm (68), then averaged to approximate the vessel diameter. To determine the true vessel diameter and vessel boundaries, intensity profiles of lines perpendicular to the vessel centerline were established by averaging intensity data every 5 pixels (microns) along the centerline on the mean registered image. This spacing was empirically determined to reduce noise in the intensity profiles but allow sufficient number of measurements along the vessel length, thereby increasing the reliability of diameter measurements. FWHM of the intensity profiles were calculated using a previously described method (13), thereby determining the vessel diameter. Vessel diameter measurements were then averaged to generate a mean D for each vessel segment.

Blood Flow Detection

Variance filtering was performed on each vessel segment in the registered image sequence to identify vessels that had detectable blood flow. In general, vessels with

detectable blood flow had centerline pixels with large temporal variance due to the motion of RBC as compared to surrounding tissue. To evaluate the local temporal variation, the SD of intensity for each pixel along the centerline was computed as a function of time over which the registered images were acquired. These values were then averaged to calculate the mean SD of intensity values along the vessel segment (μ_{vessel}). Similarly, the mean SD of intensity values of non-vessel pixels ($\mu_{background}$) was computed over time with the exclusion of vessel pixels detected by Frangi filtering. The standard deviation of the SD values ($\sigma_{background}$) were computed to determine a threshold value ($Th_{background} = \mu_{background} - \sigma_{background}$). Vessel segments with a μ_{vessel} greater than $Th_{background}$ were considered to have detectable blood flow and were included for axial blood velocity measurement.

Figure 3.1.4A displays an example of a conjunctival microcirculation image with 2 selected vessel segments. Figure 3.1.4B shows the SD of intensity values plotted as a function of length for the vessel indicated by the blue centerline. In this vessel, μ_{vessel} was lower than $Th_{background}$, indicating the lack of discernable blood flow. In contrast, Figure 3.1.4C shows the SD of intensity values plotted as a function of length for the vessel indicated by the red centerline. The mean SD (μ_{vessel}) exceeded $Th_{background}$, indicating detectable blood flow.

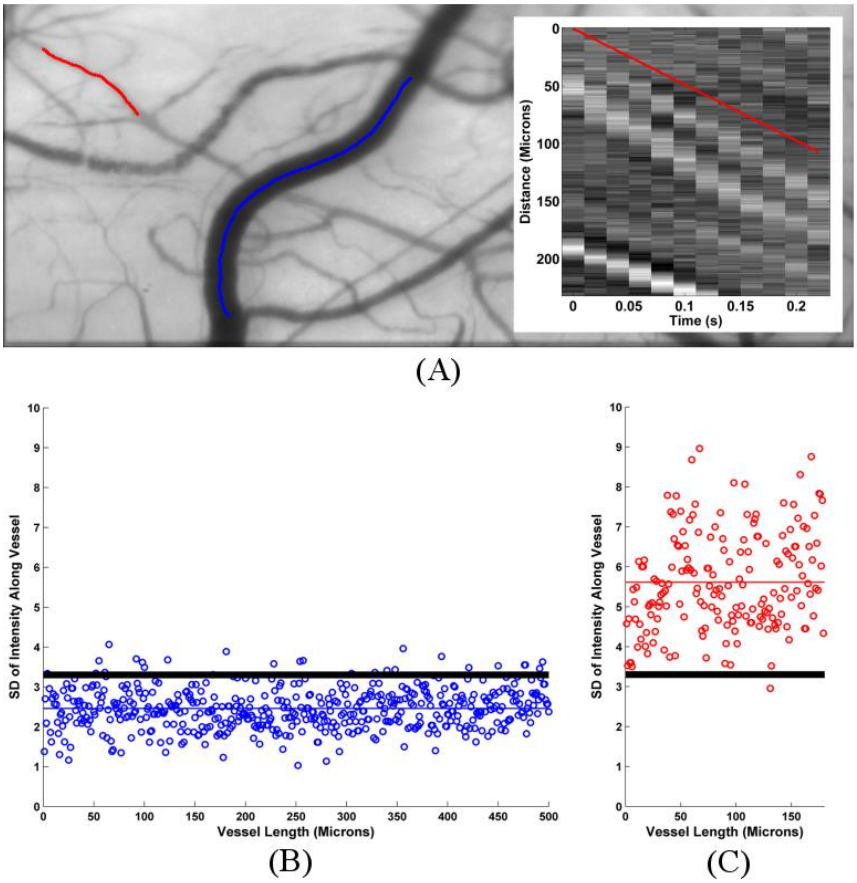

Figure 3.1.4. (A) Conjunctival microcirculation image displaying the centerlines of 2 selected vessel segments. (B) SD of intensity values plotted as a function of length for the vessel indicated by the blue centerline. Mean SD (μ_{vessel}) (blue horizontal line) is lower than the threshold ($Th_{background}$) (black horizontal line), indicating the lack of discernable blood flow. (C) SD of intensity values plotted as a function of length for the vessel indicated by the red centerline. Mean SD (μ_{vessel}) (red horizontal line) is greater than the threshold ($Th_{background}$) (black horizontal line), indicating detectable blood flow. Figure 3.1.4 (A) Insert: Spatial-temporal image (STI) generated for the vessel segment indicated by the red centerline. The red line superimposed on the STI displays the calculated slope based on the prominent bands in the STI.

Axial Velocity Measurement/Direction of Flow

Axial blood velocity (V) was measured in each vessel segment by tracking the motion of RBC along the centerline in consecutive registered image frames. Tracking was performed by creating a STI that displayed the intensity variation along the length of the vessel segment as a function of time. Axial blood velocity was derived by determining the slope of the prominent bands in the STI which was automatically determined by 1D cross-correlation between intensity data in the columns of the STI image. For pairs of columns in the STI, 1D cross-correlation was performed, and the shift in position of the aggregated RBC between columns (RBC_{shift}) was estimated based on the maximum of the cross correlation, as shown in Equation (3.1.3).

$$RBC_{shift} = \text{argmax}\ \{(f * g)\ (i)\} \tag{3.1.3}$$

where $*$ denotes the cross-correlation operator, f and g are the intensity signals along the vessel centerline in 2 adjacent columns of the STI, and i indicates the lag in position of one intensity signal with respect to the other. The slope of the STI (velocity) was obtained by averaging the RBC_{shift} values derived from the column pairs, then dividing by the time increment (20 ms) between image frames. A line with the calculated slope was superimposed on the STI for visual verification by the user. An example of a STI for one vessel segment is shown as an insert in Figure 3.1.4A.

Blood flow (Q) and wall shear rate (WSR) were computed based on D and V measurements using formulas previously published by Koutsiaris *et al* (36). Flow direction in each vessel segment was determined based on the sign of the slope of the prominent bands in the space time images. Figure 3.1.5 displays an example of vessel

diameter and axial blood velocity measurements derived from a registered image sequence. The detected boundaries of the vessels are shown in blue. The magnitude and direction of axial blood velocity are depicted by color-coded arrows. Vessels were classified as arterioles or venules by visualizing the direction of blood velocity within the vessel and determining whether blood collected into another vessel (venules) or diverged into vessel branches (arterioles).

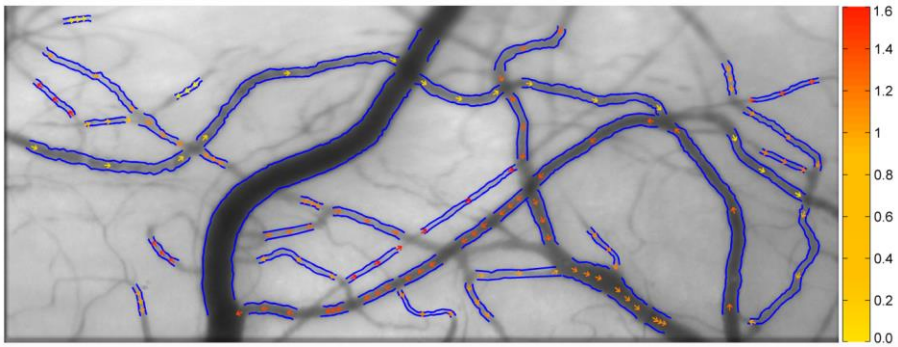

Figure 3.1.5. Conjunctival microcirculation image displaying vessel boundaries (blue lines) and the magnitude and direction of axial blood velocity (color-coded arrows). Color bar represents velocity in units of mm/s.

Statistical analysis

Statistical analyses were performed using SPSS software (version 22, SPSS, Chicago, IL, USA). Multiple measurements at different locations along the same microvessel were removed to obtain one measurement per microvessel. Measurement repeatability was assessed by the mean SD of repeated measurements averaged over all

subjects. Hemodynamic measures were averaged over each subject and compared between arterioles and venules using paired t-tests. Arterioles and venules were categorized into 1 of 4 diameter groups based on the 25%, 50%, and 75% quartiles of diameter measurements in all vessels, yielding cut points at 11 μm, 16 μm, and 22 μm. Hemodynamic measures obtained in each diameter group were averaged per subject and compared among diameter groups with one-way ANOVA. Relationships between hemodynamic measures and D were determined by linear regression analysis. Significance was accepted at $P<0.01$ to correct for multiple comparisons.

Results

Repeated measurements were obtained in 43 microvessels of 5 subjects (8 to 10 microvessels per subject). Repeatability (SD) of conjunctival D and V measurements were 0.7 μm (range: 0.6-1.0 μm) and 0.17 mm/s (range: 0.11-0.21 mm/s), respectively.

Conjunctival D and V measurements were obtained in a total of 204 arterioles. On average, measurements were obtained in 14 arterioles per subject (range: 3-27). The minimum and maximum of conjunctival D measurements were 5.9 μm and 42.9 μm, respectively. Conjunctival V ranged between 0.08 mm/s and 2.5 mm/s in arterioles.

Conjunctival D and V measurements were obtained in a total of 836 venules. On average, measurements were obtained in 56 venules per subject (range: 14-87). The minimum and maximum D measurements were 6.0 μm and 51.6 μm, respectively. Conjunctival V ranged between 0.07 mm/s and 3.4 mm/s in venules.

TABLE 3.1.1

CONJUNCTIVAL HEMODYNAMIC DESCRIPTORS.

Vessel Type	N	D (μm)	V (mm/s)	Q (pl/s)	WSR (s^{-1})
Arterioles	15	15±3	0.63±0.17	86±33	320±132
Venules	15	18±2	0.54±0.13	140±55	190±46
P-value		<0.001	0.046	0.003	0.001

The mean and SD of conjunctival hemodynamic measures in arterioles and venules in all subjects are listed in Table 3.1.1. Conjunctival D and Q were significantly higher in venules than arterioles ($P \leq 0.003$). Conjunctival V was lower in venules than arterioles, but this difference was marginally significant (P=0.05). Conjunctival WSR was significantly lower in venules than arterioles (P=0.001).

Mean and SD of conjunctival hemodynamic measures in arterioles and venules, categorized by diameter groups, are provided in Table 3.1.2 and Table 3.1.3, respectively. Conjunctival V was not statistically different among diameter groups in arterials (P=0.1), but increased with larger diameter groups in venules (P<0.001). As expected, in both arterioles and venules, Q increased with larger diameter groups (P<0.001). WSR was higher in the small diameter group in both arterioles and venules (P<0.001). Conjunctival V was linearly correlated with D in venules (P<0.001), but not in arterioles (P=0.6). Q and WSR were correlated with D in both arterioles and venules (P<0.001).

TABLE 3.1.2

CONJUNCTIVAL HEMODYNAMIC DESCRIPTORS IN ARTERIOLES, STRATIFIED BY DIAMETER GROUPS.

Diameter Groups (μm)	N	D (μm)	V (mm/s)	Q (pl/s)	WSR (s^{-1})
<11	13	9±1	0.70±0.3	40±27	488±194
11-16	13	14±1	0.62±0.2	69±26	279±99
16-22	13	19±1	0.54±0.2	111±45	163±77
>22	10	26±3	0.87±0.5	299±155	193±117
P-value		<0.001	0.125	<0.001	<0.001

TABLE 3.1.3

CONJUNCTIVAL HEMODYNAMIC DESCRIPTORS IN VENULES, STRATIFIED BY DIAMETER GROUPS.

Diameter Groups (μm)	N	D (μm)	V (mm/s)	Q (pl/s)	WSR (s^{-1})
<11	14	9±1	0.41±0.1	23±7	281±65
11-16	15	14±1	0.44±0.1	51±16	194±57
16-22	15	19±1	0.50±0.1	103±26	147±38
>22	15	28±2	0.80±0.4	356±181	162±87
P-value		<0.001	<0.001	<0.001	<0.001

Discussion

Due to physiological variations in microvascular blood flow, comprehensive assessment of a large number of microvessels is required to fully characterize the hemodynamic properties of the conjunctival microvascular network. In the current study, an automated image analysis method for quantitative assessment of hemodynamics in the conjunctival microvasculature network was reported.

In conjunctival venules of similar diameter, blood velocity measurements were in agreement with our previous published values obtained semi-automatically (1), and values reported by Jiang *et al* (14), but were slightly lower than values reported by Koutsiaris *et al* (69), which may be attributable to differences in techniques. The maximum velocity that can be measured by our system is estimated to be approximately 3.8 mm/sec, based on tracking movement of aggregated RBC along a 0.3 mm vessel segment over 4 consecutive image frames acquired at 50 Hz.

Previous studies have reported pulsation in conjunctival arterioles (70, 71). In these studies, a significantly larger number of frames were acquired at a higher frame rate which allowed measurements of velocity variations in arterioles during a complete cardiac cycle. However, in the current study, this velocity variation was not observed in the STI (as evident by the presence of linear rather than curved bands), which is likely attributed to the limited imaging time interval. Although image sequences were acquired over a 1 second time interval, the number of consecutive image frames that could be registered was limited by eye motion and blinks. Therefore, velocity measurements were obtained from different intervals of the cardiac cycle over an average time interval of 0.3

sec, which was less than a complete cardiac cycle. Lack of synchronization of image acquisition with the cardiac cycle may have increased the variability of velocity measurements. However, within subject variability was reduced by averaging data obtained in multiple same size vessels in each subject.

Currently available techniques for assessment of hemodynamics in conjunctival microvasculature utilize manual or semi-automated methods (13, 14, 36, 62), that necessitate user input and interaction. Therefore, application of these techniques to evaluate a large number of microvessels may be inefficient and time consuming. In contrast, fully automated vessel segmentation and blood flow detection by our method allows rapid and objective measurements of conjunctival hemodynamic properties in both arterioles and venules within the conjunctival microvascular network.

Assessment of microvascular hemodynamics has been reported in non-ocular tissues, including nail fold (72), sublingual mucosa (73), and buccal mucosa (74), with the use of CapiScope, a commercially available device. Although, this device is capable of automated blood vessel diameter measurements, evaluation of blood velocity requires manual drawing of a line along a target vessel. Automated hemodynamic assessment of human sublingual microcirculation was demonstrated (75), but there are no reports of automated assessment of the conjunctival microvasculature network. The automated method for vessel segmentation and blood flow detection presented in the current study allows quantitative assessment of hemodynamics in the conjunctival microvascular network and can be potentially applied to microcirculation images of other tissues. Due to the inherent heterogeneity in hemodynamics of the microcirculation, this method is

well suited for detection of microvascular hemodynamic abnormalities and advancing our understanding of microvascular pathophysiology.

2. Inter-Visit Variability of Conjunctival Microvascular Hemodynamic Measurements in Healthy and Diabetic Retinopathy Subjects

Introduction

The bulbar conjunctiva is a vascularized mucus membrane covering the outer layer of the eye. Conjunctiva has gained attention in literature due to the ease of accessibility and visibility of blood flow within the microvascular network. Conjunctival microvasculopathy and hemodynamic responses to systemic diseases such as Alzheimer's disease (5), hypertension (6), hypotension (7), diabetes (8, 16, 17, 76), and sickle cell disease (1, 3, 4, 77), have been reported. Additionally, a recent study showed a significant decrease in conjunctival blood flow, vessel density, and non-perfused areas in brain dead compared to normal subjects (78). Furthermore, abnormal conjunctival microcirculation was reported during internal carotid artery surgery (79).

The study of conjunctival microvasculature may help elucidate information relevant to the study of microcirculation in other human organs. Conjunctival microvascular complications due to diabetes have been reported (8, 16, 76), similar to those reported in the retina (80, 81). Additionally, conjunctival blood flow has shown to be correlated with sublingual microcirculation in rats (82), and with cerebral blood flow in dogs (59).

Imaging modalities including orthogonal polarization spectral imaging (12), slit-lamp stereomicroscope (13, 14, 36, 83), and intravital microscopy (3, 62), have been developed for assessment of conjunctival microvascular hemodynamics. Furthermore,

commercial devices such as retinal functional imager (11), and Heidelberg retinal flowmeter (10), have been modified to perform the same measurements.

Since systemic diseases can cause alterations in the conjunctival microvascular hemodynamics, studying inter-visit variability of the measurements is crucial to determine their sensitivity for detection of changes due to diseases. In fact, understanding the sensitivity is essential for diagnosis, monitoring and assessing treatment efficiency. Previous studies of inter-visit variability of blood flow in native arteriovenous fistula in chronic hemodialysis subjects and oxygen saturation in the retinal vasculature of healthy subjects have showed fluctuation in the measurements (84, 85). In conjunctiva, intra-visit variability of hemodynamics has been demonstrated within one or multiple sessions during a single day (10, 15, 83). Nevertheless, to the best of our knowledge, inter-visit variability of conjunctival microvascular hemodynamics was not reported previously. The purpose of the current study was to determine inter-visit variability of conjunctival microvascular hemodynamics measured quantitatively in non-diabetic and diabetic subjects at clinical stage of diabetic retinopathy (DR).

Materials and Methods

Subjects

This study protocol was approved by an institutional review board of University of Illinois at Chicago. The study was explained to subjects and informed consents were obtained according to the tenets of Declaration of Helsinki. The study population included 17 subjects: 7 non-diabetic control (NC) (4 males and 3 females), 10 with

diabetic retinopathy (DR) (6 males and 4 females). Diagnosis was based on retinal examination performed by retinal specialists. Subjects' age (mean ± SD) were 36±19 years and 57±13 years in NC and DR subjects, respectively (P=0.01). Subjects with stroke or myocardial infarction within 3 months of imaging, active angina, age-related macular degeneration, clinical diagnosis of glaucoma, dry eye syndrome, retinal vascular occlusions, history of intraocular surgery, or cataract surgery within 4 months of imaging were excluded from this study. Before imaging, subjects were asked to sit for roughly 10 minutes to facilitate a cardiovascular and respiratory resting state. During imaging, subjects were seated in front of the slit lamp biomicroscope with their head fixed with a forehead support. An external fixation target was introduced to the fellow eye to minimize eye movements. The same imaging protocol was performed on the selected eye on a follow-up visit. The follow-up durations (Mean±SD) were 11±15 and 22±8 weeks in NC and DR subjects, respectively (P=0.06). Each subject contributed to the study with one eye with a minimum of 3 repeated vessel segments in the 2 visits.

Image acquisition

Image acquisition was performed by our previously established non-invasive imaging system, EyeFlow (83). The system was built upon a traditional slit lamp bio-microscope coupled to a CCD camera (Prosilica GT, AVT, Exton, PA). Imaging was performed on the conjunctival regions temporal to the limbus. Several 1-second high magnification image sequences were recorded at 5.1X with a rate of 50 Hz (exposure of 20 ms). High magnification images were composed of 1360×550 pixels with a pixel resolution of 1.25 μm on the object plane. Contiguous low magnification images of

conjunctival microvasculature were acquired in the single-shot at 2X. Low magnification images were composed of 1024×1360 pixels with a pixel resolution of 3.12 μm on the object plane. High (5.1X) and low magnification (2X) images covered approximately a conjunctival region of 1.7 mm×0.8 mm and 3.2 mm×4.2 mm, respectively.

Image processing and analysis

High magnification image sequences were analyzed quantitatively using our previously developed automated method (83). In summary, from recorded image sequences, on average 17 (range; 6-41) consecutive frames were registered using an intensity based image registration technique to correct for eye motion. A mean image was generated by averaging the registered image sequences. Different size conjunctival microvessels were then segmented using Frangi vesselness filter applied to the mean image. Vessel caliber (D) and axial blood velocity (V) assessment was performed using FWHM and spatial-temporal image (STI) techniques, respectively. The slope of prominent bands in the STI was used to compute V. Average cross-sectional blood velocity (V_s) was computed from measurements of D and V. Blood flow ($Q=V_s\pi D^2/4$) and wall shear rate ($WSR = 8V_s/D$) were computed from V_s and D. Finally, wall shear stress ($WSS = \eta WSR$) was determined based on dynamic blood viscosity (η) which was calculated from clinical hematocrit value as described previously (13, 36).

A conjunctival mosaic image was generated per subject per visit as we described previously (83). Briefly, contiguous low magnification conjunctival microvasculature images were processed using MosaicJ, a semi-automated plug-in for ImageJ (ImageJ 1.48V), to form a mosaic image. A human observer then used the best quality mosaic

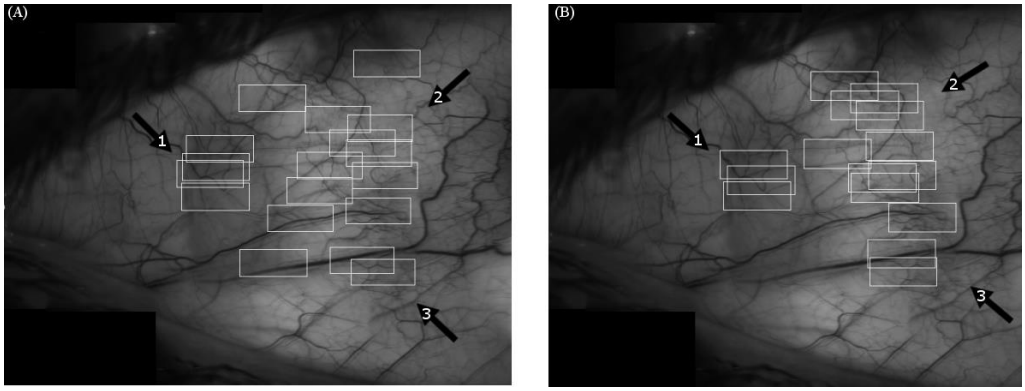

Figure 3.2.1. Example of a conjunctival mosaic image with area of image sequences overlaid by white boxes for (a) the first and (b) the second visits of a NC subject. Overlapping regions between the 2 visits are shown by similarly numbered black arrows. The mosaic image from the first visit was used to locate area of image sequences in both visits.

image from the 2 visits to locate conjunctival microvascular regions covered by each of the registered image sequences. Figure 3.2.1 Shows example of the areas covered by image sequences overlaid on a mosaic image of a NC subject in the 2 visits.

Image sequences acquired from similar conjunctival regions were further explored to find repeated vessel segments with a minimum of approximately 50% overlap between the 2 visits. Conjunctival hemodynamic measurements (D, V, Q, WSR and WSS) were then compared between each pairs of repeated vessel segments to determine inter-visit variability of the measurements. An example of conjunctival image sequences showing the same microvasculature between 2 visits in the same subject as in Figure 3.2.1, is displayed in Figure 3.2.2. Vessel segments were numbered automatically and detected vessel walls were highlighted by red lines, representing D. Direction of RBC

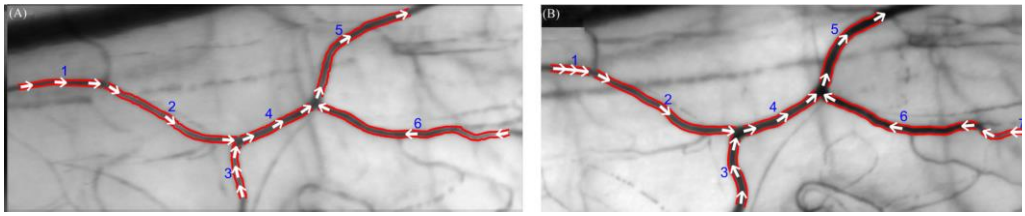

Figure 3.2.2. Example of mean conjunctival microvascular images obtained by averaging registered image sequences for a NC subject in (a) the first and (b) the second visit. Vessel segments were numbered automatically and detected vessel walls were highlighted by red lines, representing D. Direction of RBC movements were shown by white arrows. Vessel segments 1 to 5 were representing repeated microvascular between the 2 visits.

movement within microvasculature which was determined based on sign of slope of prominent bands in the STI is shown by white arrows.

Statistical analysis

Compiled data from all subjects were analyzed using Excel software (Microsoft Corp., Redmond, WA, USA). Inter-visit variability of hemodynamic measurements was quantified in NC subjects as mean and 95% confidence interval (CI) of difference of each repeated measurement, averaged per subject. The percentage number of DR subjects with D, V, Q, WSR and WSS difference beyond CI of NC subjects between the 2 visits was determined.

Results

In NC, a total of 67 repeated vessel segments were identified with D and V ranging from 11 μm to 38 μm and from 0.1 mm/s to 2 mm/s, respectively. In DR, a total

of 48 repeated vessel segments were identified with D and V ranging from 10 μm to 48 μm and from 0.1 mm/s to 2.8 mm/s, respectively.

Inter-visit variability of conjunctival microvascular D is shown in Figure 3.2.3A, with mean difference of 0.2 μm and CI from -0.7 μm to 1.2 μm. As can be seen from 3.2.3A, 60% of DR had D difference beyond normal 95% CI. However, directions of D changes were not consistent across DR subjects. Inter-visit variability of conjunctival microvascular V is shown in Figure 3.2.3B, with mean difference of -0.01 mm/s and CI from -0.3 mm/s to 0.3 mm/s. As can be seen from Figure 3.2.3B, 20% of DR had V difference higher than normal 95% CI.

Inter-visit variability of conjunctival microvascular Q is shown in Figure 3.2.4A, with mean difference of -8 pl/s and CI from -99 pl/s to 83 pl/s. As can be seen from Figure 3.2.4A, 40% of DR had D difference beyond normal 95% CI. Similar to D, directions of Q changes were not consistent across DR subjects. Inter-visit variability of conjunctival microvascular WSR is shown in Figure 3.2.4B with mean difference of -3 s^{-1} and CI from -93 s^{-1} to 87 s^{-1}. As can be seen from Figure 3.2.4B, 20% of DR had WSR difference higher than normal 95% CI. Finally, inter-visit variability of conjunctival microvascular WSS is shown in Figure 3.2.4C, with mean difference of -0.14 dyne/cm^2 and CI from -2 dyne/cm^2 to 2 dyne/cm^2. As can be seen from Figure 3.2.4C, 20% of DR had WSS difference higher than normal 95% CI.

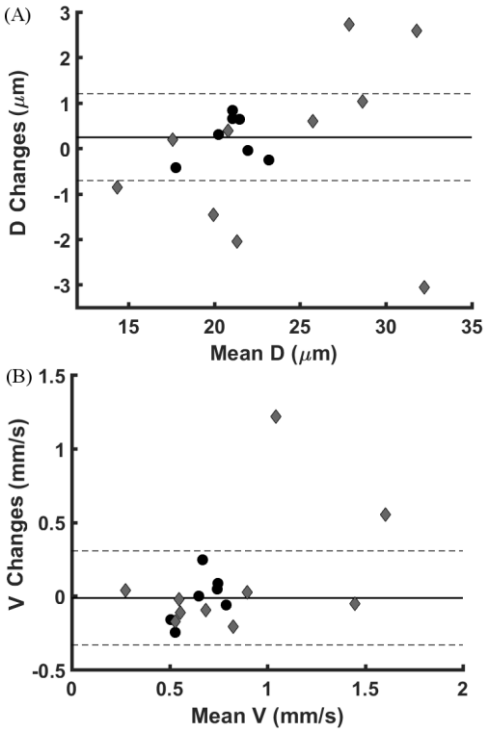

Figure 3.2.3. Inter-visit variability of conjunctival microvascular D (A) and V (B) using Bland and Altman analysis. Mean against inter-visit changes in the hemodynamic measurements, averaged per subjects are shown for NC (black circles) and DR (gray diamond) subjects. Mean of differences (solid line) and 95% CI (dashed lines) of NC subjects are also indicated.

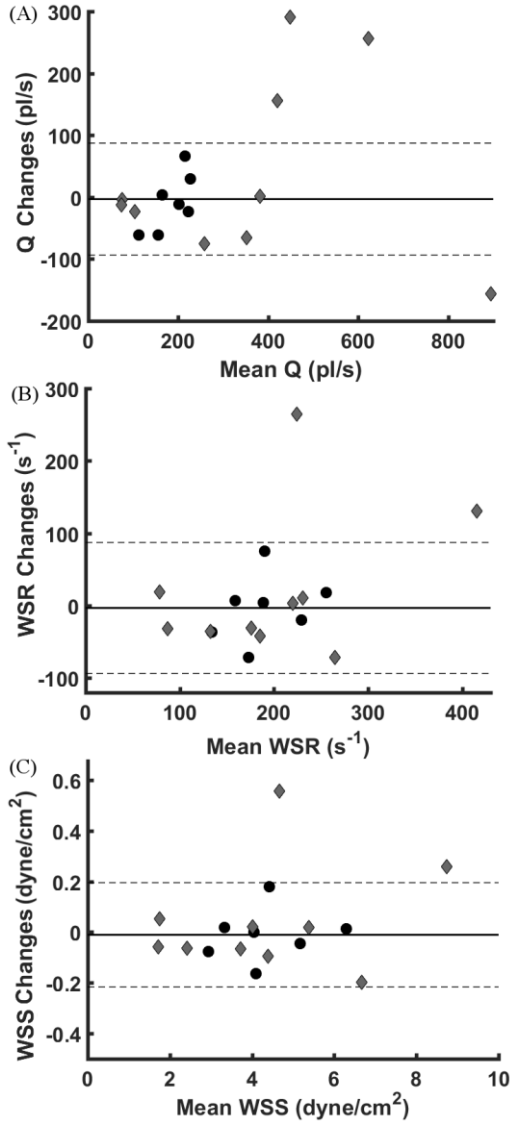

Figure 3.2.4. Inter-visit variability of conjunctival microvascular Q (A), WSR (B) and WSS (C) using Bland and Altman analysis. Mean against inter-visit changes in the hemodynamic measurements, averaged per subjects are shown for NC (black circles) and DR (gray diamond) subjects. Mean of differences (solid line) and 95% CI (dashed lines) of NC subjects are also indicated.

Discussions

Alterations in the conjunctival microvascular hemodynamics can be readily quantified due to ease of microcirculation accessibility within the network (3, 5, 8, 18, 77, 83, 86, 87). Furthermore, conjunctival microcirculation can provide information regarding pathologies and biological conditions that can alter systemic circulation (59, 78, 79, 82). In the current study, inter-visit variability of conjunctival microvascular hemodynamics (D, V, Q, WSR and WSS) was reported in NC and subjects at clinical stage of DR. The results showed, as expected, some DR had higher hemodynamic variability as compared to NC subjects. Therefore, considering measurements variability is essential for discriminating between true hemodynamic alterations and random fluctuations. Additionally, performing multiple repeated measurements may become useful to better characterize hemodynamics in the conjunctival microvascular network.

Previous studies have reported no significant intra-visit variability of conjunctival microvascular hemodynamics (15, 83). However, no previous study, to our knowledge, reported inter-visit variability of conjunctival microvascular hemodynamics in NC and diabetic subjects at clinical stages of DR. The primary conjunctival microvascular hemodynamic representatives are vessel caliber and blood velocity (13, 36). Q and WSR are determined based on D and V (36), and hence their inter-visit variability depend on changes of the 2 primary measurements. WSS however, is affected by dynamic blood viscosity which was shown to increase with progression of DR (88).

D and Q variability were higher in majority of DR than NC subjects (i.e. 60% and 40%). Nevertheless, direction of changes from based line to follow-up visit were not

consistent. The inconsistency could be possibly due to either treatments or physiological response to environmental conditions. To minimize non-pathological variation, subjects were asked to seat for roughly 10 minutes to reach a stable respiratory and circulation state. However, other factors such as diet and stress could have influenced the hemodynamics measurements (89, 90). The inter-visit variability of V, WSR and WSS was higher in 20% to 40% of DR as compared to NC subjects, which could be due to progression of the disease. We showed in a previous study that WSR and WSS decrease due to DR (86). However, a decreasing trend was not observed in the follow-up visit of DR subjects in the current study. It might be that a window larger than 13 to 33 weeks that was used in the current study is required to detect the reduction in WSS and WSR.

The current study had limitations. First, the number of subjects and repeated measurements in each group were limited. In fact, finding same vessels across the visits was difficult due to presence of large number of microvasculature and limited number of image sequences that could be acquired from each subject due to lose of fixation. Nevertheless, a minimum of 3 repeated measurements were obtained per subject to improve reliability of the result. Second, arterioles and venules were not discriminated in the current study since branching of the vessel segments could not be visualized in some of the image sequences, precluding reliable vessel type detection. Nevertheless, measurements were averaged per each eye to minimize variation due to arteriole pulsatile blood flow (69). Future studies can be helpful in determining inter-visit variability of conjunctival microvascular hemodynamics differentially in arterioles and venules. Additionally, future studies with larger number of subjects can be useful for determining the effect of duration of the disease on inter-visit variability of the hemodynamic

measurements in DR subjects. Finally, a larger clinical study can help with determining the range of D that can minimize inter-visit variability of hemodynamics within conjunctival microvascular network. Nevertheless, the current study showed that conjunctival microvascular hemodynamics can be measured reliably in NC subjects. However, slight hemodynamics variability exists between the 2 visits in NC subjects that needs to be considered for discriminating between true alterations from random fluctuations. Also, the hemodynamic measurements in some DR tend to have more variability than NC subjects which could be due to progression of the disease.

IV. ASSESSMENT OF CONJUNCTIVAL MICROVASCULAR HEMODYNAMICS IN STAGES OF DIABETIC MICROVASCULOPATHY

The contents of this chapter have been published as: Khansari, Maziyar M., Justin Wanek, Michael Tan, Charlotte E. Joslin, Jacob K. Kresovich, Nicole Camardo, Norman P. Blair and Mahnaz Shahidi. "Assessment of Conjunctival Microvascular Hemodynamics in Stages of Diabetic Microvasculopathy." Scientific Reports 7 (2017).

Introduction

Diabetes was the seventh cause of death in the US in 2010 (91). The prevalence of diabetes among US adults is projected to increase from 14% in 2010 to 21% by 2050 (92), representing a significant burden on the population. Previous studies have reported a high prevalence of microvascular disease in diabetic subjects (93, 94), and indeed the most common cause of morbidity and mortality among diabetics is related to vasculopathy (95, 96). Alterations in circulation due to diabetes adversely affect various organ systems, causing complications such as, DR, nephropathy, neuropathy, cardiovascular disease, genitourinary problems, amputations and foot ulcers (97). Therefore, assessment of microvascular hemodynamics can be useful for evaluation and monitoring of complications due to diabetes.

Microvascular hemodynamic alterations due to diabetes have been reported in various tissues, including the brain, heart, foot, sublingual tissues, nail fold, retina, and conjunctiva (3, 8, 17, 18, 75, 98-111). Due to the accessibility of the conjunctiva for direct visualization of microcirculation, alterations in the conjunctival microvasculature

due to diabetes have been reported based on determination of a severity index (SI) (3, 8, 18, 110). The SI incorporated several factors, including the number of blood vessels with abnormal morphometry, blood vessel diameter, arteriole to venule ratio, blood velocity and viscosity. However, these studies did not provide assessment of conjunctival hemodynamic alterations at progressive stages of diabetic microvasculopathy.

Since DR stage is thought to parallel progressive levels of diabetic microvasculopathy in other tissues (83, 112), assessment of the conjunctival hemodynamics at stages of DR may become useful for gaining a better understanding of diabetes pathophysiology, and potentially allow diagnostic evaluation of diabetic microvasculopathy. Additionally, conjunctival and retinal hemodynamics may be comparable as suggested by a previous report of similarities in diabetic-related microvasculopathies between the conjunctiva and the retina (109). The purpose of the current study was to provide a comprehensive and quantitative assessment of alterations in conjunctival hemodynamic descriptors at progressive stages of diabetic microvasculopathy by application of our previously established conjunctival microcirculation imaging technique (83).

Materials and Methods

Subjects

The study was approved by an institutional review board of the University of Illinois at Chicago. The study was explained to subjects and written informed consents were obtained from participants according to the tenets of the Declaration of Helsinki.

The cohort consisted of 161 subjects (58 males and 103 females) with ages ranging from 21 to 87 years old. Based on a complete clinical history and ocular examination, including a dilated fundus examination, the subjects were categorized into one of four groups: NC (N=34) and 3 diabetic groups of increasing microvasculopathy severity: no DR (NDR; N=47), non-proliferative DR (NPDR; N=45) and proliferative DR (PDR; N=35). Twelve (5 NDR, 2 NPDR, 5 PDR) and 115 (42 NDR, 43 NPDR, 30 PDR) subjects had type 1 and 2 diabetes, respectively. Exclusion criteria were inability to give informed consent or participate in the study, stroke or myocardial infarction within 3 months of imaging, active angina, dry eye syndrome, conditions that can affect the ocular surface, clinical diagnosis of glaucoma, age-related macular degeneration, retinal vascular occlusions or any other retinal, choroidal or optic nerve disease that could interfere with the staging of DR, history of intraocular surgery within 4 months of imaging, or cataract surgery within 4 months of imaging. Glycated hemoglobin (HbA1c), HCT, systolic blood pressure (SBP), diastolic blood pressure (DBP), and heart rate (HR) were measured at the time of imaging. Mean arterial pressure (MAP) was computed as (SBP+2DBP)/3. Data from one eye per subject was included in the study based on the exclusion criteria, ability to maintain fixation during imaging, and image quality. If both eyes qualified, the eye with the larger number of acquired images was selected. During imaging, a headrest and forehead support was used to stabilize subject's head, and a fixation target was presented to the fellow eye to minimize eye movement. Subjects were asked to suspend blinking during the one-second duration of image acquisition, and then allowed to blink normally.

Image Acquisition

Imaging of the conjunctival microcirculation was performed using our previously described non-invasive optical imaging system (EyeFlow) (83). Briefly, the imaging system comprised a slit lamp biomicroscope and a CCD camera (Prosilica GT, AVT, Exton, PA) for the acquisition of image sequences of RBC motion through the conjunctival microvasculature. The slit lamp light source, fitted with a narrow band optical filter with a transmission wavelength of 540±5 nm, was used to illuminate the conjunctival microvasculature. One-second image sequences were captured from the superficial conjunctival microvasculature at a rate of 50 frames per second with 5.1X magnification. Each image consisted of 1360×550 pixels with a pixel resolution of 1.25 μm on the object plane. This process was repeated to acquire image sequences from multiple non-overlapping conjunctival microvascular regions temporal to the limbus that encompassed up to 10 mm×13 mm areas.

Image Processing and Analysis

Conjunctival image sequences were automatically analyzed with our previously validated method (83), using customized software written in MATLAB (Release 2015b, MathWorks, Inc. Natick, MA, USA). The automated method for measuring conjunctival hemodynamics consisted of several steps including image registration, vessel segmentation, centerline and bifurcation extraction, diameter measurement, blood flow detection and axial blood velocity measurement. Briefly, an intensity-based image registration algorithm was employed to correct for eye movement in image sequences. Frames with blinks, large eye motion, or illumination artifacts were eliminated from each

image sequence, then the longest consecutive number of frames were registered. A time-averaged image was then generated from the registered image set, and Frangi filtering was performed for segmentation of conjunctival vessels. Vessel centerlines were extracted by thinning the segmented vessels, then bifurcation points were identified to define centerlines of all individual vessel segments. To ensure adequate sampling and reliability of measurements, only vessel segments with centerline lengths above 50 microns were included for hemodynamic analysis. Variance filtering was performed on the remaining vessel segments to distinguish vessels with detectable blood flow. D and vessel boundaries were measured by computing the FWHM of intensity profiles, established perpendicular to the centerline direction at every 5 pixels along the microvessel. V was determined by tracking the movement of RBC along the vessel centerline in the registered image sequences using STI (83). The STI showed variation of intensity values along a vessel centerline over time due to RBC motion. V was calculated by determining the slope of the prominent bands in the STI. V_s from D and V, $Q = V_s\pi D^2/4$, $WSR = 8V_s/D$, η from HCT and D, and $WSS = \eta WSR$ were determined using previously described formulas (36, 38).

Microvessels were categorized as arterioles or venules by visualization of the direction of blood flow within the vessels and distinguished if the flow diverged into smaller vessel branches (arteriole) or collected into a larger vessel (venule). If multiple measurements were obtained along the same vessel, data from the vessel segment with the longest centerline were included for analysis. Image acquisition was not synchronized with the heart rate, and hence arteriolar and venular hemodynamic

measurements were obtained at different time points during the cardiac cycle, though hemodynamics in venules are less dependent on the cardiac cycle (70).

Statistical Analysis

Compiled data consisting of one value per hemodynamic descriptor (D, V, Q, WSR and WSS) per vessel per subject were analyzed using Stata version 12 (College Station, TX: StataCorp LP). Demographic and systemic physiologic data were compared among groups using the Chi-Square test or ANOVA. Mean conjunctival hemodynamic descriptors were computed and compared among NC and stages of DR (NDR, NPDR and PDR) using ANOVA. A generalized linear mixed model (GLMM) with random intercepts was used to estimate beta (β) and 95% confidence intervals (CI) and examine associations between DR stage and each hemodynamic descriptor outcome. Fixed effects were analogous to standard regression analysis and estimated directly. The model assumed a Gaussian error distribution. Unadjusted models regressed the DR stage group (categorical) on the hemodynamic descriptors with no additional fixed effects. The random intercepts were established by identification of the individual study participants using their study id number. The adjusted models regressed the DR stage group (categorical), and the following fixed effects: age (continuous), race (categorical), sex (categorical), MAP (continuous), HR (continuous), HCT (continuous) and HbA1C (continuous) on the hemodynamic descriptors. Again, the random intercepts were established by identification of the individual study participants using their study id number. Since race was not matched between groups of subjects, race differences were adjusted in the models according to well-established statistical data analysis

methodologies. Eye examined was not considered as a covariate in the model because it was not associated with hemodynamic descriptors. The association between V (dependent variable) and D (independent variable) was determined in each group and compared to NC subjects while accounting for multiple measurements per subject in both adjusted and unadjusted models. The estimated β value (denoted by slope) derived by the model represented the increase in V per one-unit increase in D. Statistical tests were 2-sided and significance was accepted at $P \leq 0.05$.

Results

Demographic and Physiologic Data

Subjects' demographics and physiologic data are reported in Table 4.1. Sex, MAP, and eyes examined were not different among DR stages ($P \geq 0.3$). However, age, race, HR, HCT, and HbA1C were different ($P \leq 0.03$).

Conjunctival Hemodynamic Descriptors in Arterioles

Conjunctival hemodynamic measurements were obtained in a total of 1861 arterioles. The Mean±SD number of arteriole measurements was 10±5, 9±4, 9±4, and 8±5 in NC, NDR, NPDR, and PDR subjects, respectively. There was no difference in the number of arteriole measurements among the groups of subjects ($P=0.2$).

Mean and SD of unadjusted conjunctival arteriolar D, V, Q, WSR and WSS stratified by DR stage are provided in Table 4.2. D and Q were similar ($P \geq 0.8$), while V, WSR, and WSS were different among DR groups ($P \leq 0.03$).

Estimates of DR stage differences from the statistical model with and without adjusting for age, race, sex, MAP, HR, HCT, and HbA1C are shown in Table 4.3. D and Q were not different between NC and stages of DR with and without adjusting for covariates ($P \geq 0.3$). V, WSR, and WSS were lower in NDR than NC subjects with and without adjusting for covariates ($P \leq 0.01$). Additionally, unadjusted WSR and WSS were lower in NPDR than NC subjects ($P \leq 0.04$), but the adjusted differences were not significant ($P \geq 0.2$). Similarly, unadjusted WSS was lower in PDR than NC subjects ($P=0.05$), but not after adjusting for covariates ($P=0.3$). After adjusting for covariates, V and WSR were lower in NDR as compared to NPDR subjects ($P \leq 0.02$; results not shown in Table 4.3) and V was lower in NDR as compared to PDR subjects ($P=0.02$; results not shown in Table 4.3).

The associations between conjunctival arteriolar V and D stratified by DR stage with and without adjusting for age, race, sex, MAP, HR, HCT, and HbA1C are provided in Table 4.4. After adjusting for covariates, the associations between V and D were significant in NC, NDR, and PDR. The associations between V and D were weaker in NPDR and PDR as compared to NC subjects ($P \leq 0.006$).

Conjunctival Hemodynamic Descriptors in Venules

Conjunctival hemodynamic measurements were obtained in a total of 9027 venules. The Mean±SD number of venule measurements was 24±11, 21±7, 22±8 and 20±7 in NC, NDR, NPDR, and PDR subjects, respectively. There was no difference in the number of venules measurements among the groups of subjects ($P=0.2$).

Mean and SD of unadjusted conjunctival venular D, V, Q, WSR and WSS stratified by DR stage are provided in Table 4.5. D, V and Q were similar among groups ($P \geq 0.08$), whereas WSR and WSS were different ($P \leq 0.05$).

Estimates of DR stage differences from the statistical model with and without adjusting for age, race, sex, MAP, HR, HCT, and HbA1C are shown in Table 4.6. Q was not different between NC and stages of DR with and without adjusting for covariates ($P \geq 0.1$). D was higher in NDR than NC subjects with and without adjusting for covariates ($P \leq 0.03$). WSR and WSS were lower in NDR than NC subjects with and without adjusting for covariates ($P \leq 0.01$). D was higher in NPDR than NC subjects, regardless of the effects of age, race, sex, MAP, HR, HCT, and HbA1C ($P \leq 0.02$). WSR was lower in NPDR than NC subjects after adjusting for covariates ($P=0.05$). WSS was lower in NPDR than NC subjects with and without adjusting for covariates ($P \leq 0.02$). V was lower in PDR than NC subjects after adjusting for covariates ($P=0.04$). WSR and WSS were lower in PDR than NC subjects with and without adjusting for covariates ($P \leq 0.02$). After adjusting for covariates, V and Q were higher in NPDR as compared to PDR subjects ($P \leq 0.04$; results not shown in Table 4.6).

The associations between conjunctival venular V and D stratified by DR stage with and without adjusting for age, race, sex, MAP, HR, HCT, and HbA1C are provided in Table 4.7. After adjusting for covariates, the associations between V and D were significant in all groups. The association between V and D was stronger in NPDR as compared to NC subjects ($P=0.01$).

TABLE 4.1

SUBJECTS' DEMOGRAPHICS AND PHYSIOLOGIC DATA.

	Total (N=161)		NC (N=34)	NDR (N=47)	NPDR (N=45)	PDR (N=35)	P-value
	N	%	%	%	%	%	
Sex							0.3[a]
Male	58	36	24	34	40	46	
Female	103	64	76	66	60	54	
Race							<0.001[a]
AA	74	46	12	62	51	51	
White	48	30	77	21	16	14	
Hispanic	39	24	12	17	33	34	
Eye Examined							0.8[a]
Right	108	67	74	64	64	69	
Left	53	33	27	36	36	31	
Age (years)	57±12		61±11	55±14	58±10	53±9	0.03[b]
MAP (mmHg)	91±13		89±10	92±11	91±13	94±17	0.4[b]
Heart Rate (BPM)	75±11		69±9	73±10	78±12	78±11	0.001[b]
Hematocrit (%)	41±6		44±5	42±5	40±5	37±6	<0.001[b]
HbA1C (%)	7.4±1.9		5.5±0.5	7.4±1.5	8.4±1.7	8.2±2	<0.001[b]
HbA1C (mmol/mol)	57±21		37±6	57±16	68±19	66±22	<0.001[b]

P-values derived by Chi square ([a]) or ANOVA ([b]).

TABLE 4.2

CONJUNCTIVAL HEMODYNAMIC DESCRIPTORS IN ARTERIOLES STRATIFIED BY DR STAGE.

Hemodynamic	NC (N=34)	NDR (N=47)	NPDR (N=45)	PDR (N=35)	P-value*
D (μm)					
Mean±SD	18±5	19±4	18±4	18±5	0.9
[Min–Max]	[6–61]	[7–53]	[7–47]	[7–58]	
V (mm/s)					
Mean±SD	0.70±0.23	0.54±0.22	0.62±0.24	0.64±0.27	0.03
[Min–Max]	[0.08–3.02]	[0.07–24]	[0.07–3.27]	[0.08–3.44]	
Q (pl/s)					
Mean±SD	144±118	124±98	135±90	146±115	0.8
[Min–Max]	[5–1672]	[3–2306]	[4–1234]	[2.6–1566]	
WSR (s^{-1})					
Mean±SD	280±115	193±87	232±109	245±106	0.003
[Min–Max]	[15–2288]	[18–1310]	[15–1365]	[24–1563]	
WSS (dyne/cm^2)					
Mean±SD	8.6±5.0	5.4±3.2	6.2±3.3	6.6±3.7	0.003
[Min–Max]	[0.03–3.2]	[0.03–6.3]	[0.03–5.0]	[0.04–6.0]	
Arterioles sample size					
Mean±SD	10±5	9±4	9±4	8±5	0.2
[Min–Max]	[4–32]	[4–33]	[4–27]	[3–31]	

*P-value determined by ANOVA.

TABLE 4.3

COMPARISON OF CONJUNCTIVAL HEMODYNAMIC DESCRIPTORS IN ARTERIOLES BETWEEN NC AND DR SUBJECTS IN UNADJUSTED (MODEL 1) AND ADJUSTED (MODEL 2) MODELS.

	D (μm)		V (mm/s)		Q (pl/s)		WSR (s^{-1})		WSS (dyne/cm^2)	
	β	P	β	P	β	P	β	P	β	P
Intercept	18	<0.001	0.69	<0.001	144	<0.001	278	<0.001	8.6	<0.001
Model 1: DR Stage Effect*										
NC	Ref.	Ref.	Ref.	Ref.	Ref.	Ref.	Ref.	Ref.	Ref.	Ref.
NDR	0.7	0.5	-0.16	<0.001	-21	0.3	-87	<0.001	-3.2	<0.001
NPDR	0.7	0.4	-0.07	0.2	-6	0.8	-47	0.04	-2.4	0.01
PDR	0.4	0.7	-0.04	0.4	8	0.7	-32	0.2	-1.8	0.05
Intercept	21	<0.001	0.98	<0.001	575	<0.001	755	<0.001	19.3	<0.001
Model 2: DR Stage Effect**										
NC	Ref.	Ref.	Ref.	Ref.	Ref.	Ref.	Ref.	Ref.	Ref.	Ref.
NDR	0.1	0.9	-0.11	0.01	-16	0.4	-60	<0.001	-2.2	<0.001
NPDR	0.8	0.4	0.02	0.7	14	0.5	-15	0.5	-1.1	0.2
PDR	0.9	0.4	0.00	0.1	13	0.6	-18	0.4	-0.9	0.3

*Unadjusted.

**Adjusted for age, race, sex, mean arterial pressure, heart rate, hematocrit, and hemoglobin A1C.

TABLE 4.4

COMPARISON OF ASSOCIATION BETWEEN CONJUNCTIVAL V AND D IN ARTERIOLES BETWEEN NC AND DR SUBJECTS IN UNADJUSTED (MODEL 1) AND ADJUSTED (MODEL 2) MODELS. SLOPES OF THE REGRESSION LINES RELATING V AND D ARE PROVIDED.

	Slope (s^{-1})	95% CI	P-value*
Model 1: DR Stage Effect			
NC	3	-4–9	Ref
NDR	11[a]	6–15	0.05[b]
NPDR	3	-2–9	0.9
PDR	5	-1–11	0.5
Model 2: DR Stage Effect			P-value**
NC	15[a]	7–22	Ref
NDR	19[a]	14–24	0.1
NPDR	5	-1–11	0.001[b]
PDR	10[a]	3–17	0.006[b]

[a]Significant association between V and D.
[b]Association between V and D significantly different than NC (ref).
*Unadjusted.
**Adjusted for age, race, sex, mean arterial pressure, heart rate, hematocrit, and hemoglobin A1C.

TABLE 4.5

CONJUNCTIVAL HEMODYNAMIC DESCRIPTORS IN VENULES STRATIFIED BY DR STAGE.

Hemodynamic	NC (N=34)	NDR (N=47)	NPDR (N=45)	PDR (N=35)	P-value*
D (μm)					
Mean±SD	20±2	21±3	21±3	20±3	0.08
[Min–Max]	[6–75]	[7–71]	[7–68]	[7–74]	
V (mm/s)					
Mean±SD	0.59 ±0.17	0.54±0.17	0.57±0.13	0.52±0.19	0.3
[Min–Max]	[0.06–4.55]	[0.07–4.39]	[0.05–6.34]	[0.04–4.9]	
Q (pl/s)					
Mean±SD	175 ± 64	175 ± 79	195 ± 61	173 ± 94	0.5
[Min–Max]	[3–3197]	[3–7855]	[3–5408]	[3–7937]	
WSR (s^{-1})					
Mean±SD	183±56	154±47	164±52	153 ± 52	0.05
[Min–Max]	[15–2218]	[17–1406]	[10–2722]	[13–1405]	
WSS (dyne/cm^2)					
Mean±SD	4.8 ±1.8	3.8±1.2	3.9±1.6	3.6±1.3	0.005
[Min–Max]	[0.03–9.88]	[0.03–4]	[0.02–9.5]	[0.02–5.6]	
Venules sample size					
Mean±SD	24±11	21±7	22±8	20±7	0.2
[Min–Max]	[14–108]	[26–101]	[19–150]	[18–81]	

*P-value determined by ANOVA.

TABLE 4.6

COMPARISON OF CONJUNCTIVAL HEMODYNAMIC DESCRIPTORS IN VENULES BETWEEN NC AND DR SUBJECTS IN UNADJUSTED (MODEL 1) AND ADJUSTED (MODEL 2) MODELS.

	D (μm)		V (mm/s)		Q (pl/s)		WSR (s^{-1})		WSS (dyne/cm^2)	
	β	P	β	P	β	P	β	P	β	P
Intercept	20	<0.001	0.59	<0.001	173	<0.001	183	<0.001	4.8	<0.001
Model 1: DR Stage Effect*										
NC	Ref.	Ref.	Ref.	Ref.	Ref.	Ref.	Ref.	Ref.	Ref.	Ref.
NDR	1.2	0.03	-0.05	0.2	5	0.8	-29	0.01	-1.1	0.001
NPDR	1.4	0.02	-0.01	0.7	25	0.1	-19	0.1	-0.9	0.008
PDR	0.4	0.52	-0.06	0.1	4	0.8	-29	0.02	-1.2	<0.001
Intercept	19	<0.001	0.49	0.004	151	0.05	185	0.001	3.4	0.03
Model 2: DR Stage Effect**										
NC	Ref.	Ref.	Ref.	Ref.	Ref.	Ref.	Ref.	Ref.	Ref.	Ref.
NDR	1.4	0.03	-0.06	0.2	7	0.7	-33	0.01	-1.1	0.004
NPDR	2.1	0.006	-0.03	0.6	26	0.2	-29	0.05	-1.1	0.02
PDR	1.1	0.19	-0.11	0.04	-6	0.8	-47	0.003	-1.4	0.002

*Unadjusted.

**Adjusted for age, race, sex, mean arterial pressure, heart rate, hematocrit, and hemoglobin A1C.

TABLE 4.7

ASSOCIATION BETWEEN CONJUNCTIVAL V AND D IN VENULES BETWEEN NC AND DR SUBJECTS IN UNADJUSTED (MODEL 1) AND ADJUSTED (MODEL 2) MODELS. SLOPES OF THE REGRESSION LINES RELATING V AND D ARE PROVIDED.

	Slope (s^{-1})	95% CI	P-value*
Model 1: DR Stage Effect			
NC	18[a]	16–21	Ref
NDR	18[a]	16–19	0.6
NPDR	22[a]	20–23	0.01[b]
PDR	21[a]	19–23	0.1
Model 2: DR Stage Effect			
NC	18[a]	16–21	Ref
NDR	18[a]	16–19	0.5
NPDR	22[a]	20–23	0.01[b]
PDR	21[a]	19–23	0.1

[a]Significant association between V and D.
[b]Association between V and D significantly different than NC (ref).
*Unadjusted.
**Adjusted for age, race, sex, mean arterial pressure, heart rate, hematocrit, and hemoglobin A1C.

Discussion

In the current study, a comprehensive and quantitative assessment of alterations in hemodynamic descriptors (D, V, Q, WSR and WSS) within the conjunctival network was reported differentially in arterioles and venules at progressive stages of DR. In arterioles, V was reduced in NDR subjects, consistent with a previous finding (17), though arterioles and venules were not differentiated in this study. Arteriolar WSR were reduced only in NDR subjects, suggestive of a potential early marker of diabetic microvasculopathy. Conjunctival microvascular hemodynamic abnormalities were more frequent in venules than arterioles, similar to a previous report that used a non-quantitative method (111). In venules, vasodilation was observed in NDR and NPDR subjects, consistent with previously studies (9, 113), though these studies did not differentiate dilation in arterioles and venules and reported vasodilation in the entire conjunctival microvascular network. Increased vascular endothelial growth factor (VEGF) expression is known to cause vasodilation (114, 115), and VEGF expression has been previously reported to be elevated in conjunctival macrophages, epithelial, endothelial, and fibroblast cells in NPDR and PDR subjects (116). Therefore, the finding of venular vasodilation in NPDR may be attributed, at least in part, to the elevation of VEGF expression. Further combined studies of vascular caliber and VEGF levels are needed to investigate the potential effect of VEGF expression on conjunctival vasodilation. In venules, WSR was reduced at all stages of DR, which is likely attributed to the observed vasodilation in NDR and NPDR subjects, and decreased V in PDR subjects. Reduction in V is supported by previously reported increased blood viscosity in diabetic subjects (117).

There is no previous study, to the best of our knowledge, that reported alterations in conjunctival Q in a quantitative manner due to diabetes. In the current study, no Q alteration was detected in the conjunctival arterioles or venules of DR as compared to NC subjects. This finding is in agreement with a previous study that compared the nail fold microcirculation between diabetic and non-diabetic subjects (118). However, previous studies of the retinal circulation have reported conflicting results of increased Q in early DR (98), unaltered Q in NDR or early DR (99), decreased Q in NPDR (100), decreased Q in PDR (101), and unaltered Q in PDR (102). Future studies are needed to evaluate Q in both retina and conjunctiva of the same subjects to determine whether conjunctival and retinal Q are related.

WSS is an important hemodynamic parameter in cardiovascular pathophysiology (119), and affects endothelial functions, such as migration of leukocytes, adhesion, control of vessel diameter, cytoskeletal structure, and energy metabolism (119-122). WSS is generally lower in subjects at risk of vascular diseases (123), and causes vessel wall remodeling and pathophysiology (124, 125). Reduced WSS in the retinal arterioles of subjects with early DR (126), and in the carotid and branchial arteries of diabetic subjects (71, 127) was previously reported. No previous study, to our knowledge, has reported WSS in conjunctival microcirculation of diabetic subjects. In the current study, WSS was lower in conjunctival arterioles of NDR subjects and in venules at all stages of DR, as compared to non-diabetic subjects.

Reduced WSS may promote endothelial dysfunction (126), and contribute to the development of microvasculopathy and DR (128, 129). Furthermore, previous studies

have found an association of reduced WSS with increased vascular cellular adhesion molecules-1 (VCAM-1) (130, 131) and upregulation in the expression of VCAM-1 and intercellular adhesion molecules-1 (ICAM-1) in DR which leads to leukocytes accumulation in the retinal microcirculation (132-134). Therefore, assessment of WSS in the conjunctival microcirculation may be potentially useful for evaluating microcirculatory abnormalities due to diabetes with and without clinical DR.

Murray's law (135), predicts a linear relationship between V and D under a normal physiological condition. The large sample size in the current study allowed us to test the linearity of this relationship in the conjunctival microcirculation. A positive linear association was found between V and D in both arterioles and venules in NC subjects. This finding is in agreement with a previous study that showed a trend of increased V with larger D (69). Furthermore, alterations in the dependence of V on D were present in NPDR and PDR subjects that suggest physiological abnormalities in conjunctival arterioles and venules at clinical stages of DR.

In the current study, the number of venules was greater than arterioles which is primarily due to the conjunctiva anatomy in which arterioles are less numerous than venules, as previously reported (3, 8). The lower sampling of arterioles could also be attributed by the fact that arterioles tend to have lower image contrast compared to venules. Despite the difference in vessel sampling, the findings of the current study are based on a very large sample size of approximately ten thousand arterioles and venules.

There were limitations in the current study. First, the imaging system was not synchronized with the cardiac cycle to account for velocity changes in arterioles due to

pulsatility which was reported previously (70). However, variability of V measurements due to pulsatility was reduced by averaging multiple arteriole measurements per subject. In the future, synchronization of imaging system with the cardiac cycle will enable assessment of conjunctival hemodynamics at peak systolic and diastolic blood pressure and should improve reliability of arteriole measurements. Second, identification of arterioles and venules was performed manually. Although human error in the identification of vessel type cannot be completely eliminated, the error was likely minimal since the direction of blood flow was clearly visualized in the image sequences. Third, motion of RBC was detectable in superficial vessels that were in the focal plane of the instrument and between 6 and 70 microns in diameter.

In summary, in non-clinical DR, arteriolar V was decreased and venular D was increased, while venular V was decreased in advanced DR and D was increased in clinical DR. At all stages of DR, venular WSS was decreased. Future studies are needed to determine the association between retinal and conjunctival hemodynamic alterations and substantiate the value of conjunctival microcirculation imaging as a surrogate for screening and monitoring of DR. Additionally, further investigation is warranted to relate alterations in conjunctival microvascular hemodynamic descriptors with incidence of complications due to diabetic microvasculopathy. Overall, assessment of conjunctival hemodynamic alterations has the potential for diagnostic evaluation and longitudinal monitoring of diabetic microvasculopathy complications.

V. AUTOMATED FINE STRUCTURE IMAGE ANALYSIS FOR DISCRIMINATION OF DIABETIC RETINOPATHY STAGE USING CONJUNCTIVAL AND RETINAL MICROVASCULATURE IMAGES

The contents of this chapter have been published as: Khansari, Maziyar M., William O'Neill, Richard Penn, Felix Chau, Norman P. Blair and Mahnaz Shahidi. "Automated fine structure image analysis method for discrimination of diabetic retinopathy stage using conjunctival microvasculature images." Biomedical optics express 7, no. 7 (2016): 2597-2606.

1. An Automated Fine Structure Image Analysis Method for Discrimination of Diabetic Retinopathy Stage Using Conjunctival Microvasculature Images

Introduction

Diabetic retinopathy (DR) is the leading cause of vision loss in working age adults in the US (91). DR is considered a microvascular disease and the earliest signs of microvasculopathies occur at the level of the small blood vessels or capillaries. In fact, retinal tissue ischemia due to capillary non-perfusion and macular edema due to increased vascular permeability cause vision loss in DR. Currently, discrimination of stages of DR is based on clinical visual examination of the retinal tissue for signs of microaneurysms, hard exudates, hemorrhages, and other pathologies. Additionally, clinical fluorescein angiography (FA) allows visualization of retinal vascular perfusion and leakage, and optical coherence tomography (OCT) provides quantitative assessment of retinal

thickening due to macular edema. In recent years, several research imaging techniques have been developed to assess retinal microvasculature abnormalities in diabetic subjects (20-25). Furthermore, methods for fractal analysis have been developed that relate the pattern of major retinal blood vessels to age, blood pressure, and diabetes (136-138). Recently, OCTA has become available for imaging of the retinal microvasculature (46, 139). Application of this technology to DR subjects has demonstrated alterations in the retinal microvasculature, including capillary non-perfusion, microaneurysms, and pre-retinal neovascularization (140-142).

Since diabetes is a systemic disease, it is expected that microvasculopathies present in the retinal tissue to be also evident, at least in part, in the microvasculature of other tissues. One such tissue is the conjunctiva, a densely vascularized mucus membrane covering the sclera of the eye with a unique advantage of accessibility for direct visualization and non-invasive imaging. Indeed, several studies have evaluated and reported microvascular abnormalities in the conjunctiva of diabetic subjects, similar to those reported in the retinal tissue (16-18, 76, 109, 113, 143).

Several techniques have been developed for imaging of the conjunctival microvasculature, including retinal functional imager (11), orthogonal polarization spectral imaging (12), slit lamp biomicroscopy (13, 36), and intravital microscopy (3, 62). Furthermore, conjunctival microvasculature has been assessed quantitatively using automated (83), and semi-automated (13, 83), software. However, methods for discrimination health and disease based on evaluation of conjunctival microvasculature have not been reported. In the current study, we present application of a method (19), for

fine structure analysis of conjunctival microvasculature images for discriminating subjects at progressive stages of DR.

Materials and Methods

Subjects

The study was approved by an institutional board of the University of Illinois at Chicago. The study was explained to subjects and informed consents were obtained with accordance to declaration of Helsinki. A total of 76 subjects participated in the study. The subjects underwent a dilated retinal examination by a retinal specialist who used the conventional clinical categories to classify each retina as NC (N=22), NDR (N=17), NPDR (N=17) or PDR (N=20). The subjects were 27 males and 49 females. Images of one eye of each subject were included. The subjects' ages (Mean±SD) were 63±12 years, 57±13 years, 62±8 years and 53±10 years in NC, NDR, NPDR and PDR groups, respectively (P=0.02). PDR subjects were significantly younger than NC subjects (P=0.03).

Image Acquisition

Imaging was performed using our previously described system EyeFlow (83), consisting of a slit lamp biomicroscope (2X magnification) coupled to a CCD camera (Prosilica GT, AVT, Exton, PA). Active camera sensor size was 8.8 mm×6.6 mm with a fill factor of 100%, and approximate quantum efficiency of 50%. The conjunctiva was illuminated by white light passed through a green filter (540±4 nm) which enhanced image contrast. Each image was 1024×1360 pixels at 3.12 μm/pix on the object plane,

and thus covered a 3.2 mm×4.2 mm area of the conjunctiva. Contiguous conjunctival microvasculature images with approximately 10% overlap were acquired at regions temporal to the limbus.

Image Processing

Conjunctival microvasculature images were montaged to generate a single mosaic image using MosaicJ software, a semi-automated image processing plug-in for ImageJ (ImageJ 1.48V). Final adjustments to generate a seamless mosaic image were performed by the plug-in. The mosaic image displayed a conjunctival microvasculature region up to 9.6 mm×12.6 mm area. An example of a cropped conjunctival mosaic image in a diabetic (PDR) subject is shown in Figure 5.1.1. Presence of light illumination artifacts and image blur due to eye movement precluded the use of entire mosaic for analysis. Thus, from the mosaic image, a conjunctival region of interest (ROI) (1000×1000 pixels) covering a 3.1 mm×3.1 mm area was selected. The ROI showed a dense vascularized region with good focus and devoid of illumination artifacts. Examples of 2 selected ROIs are outlined by squares overlaid on the mosaic image shown in Figure 5.1.1.

Automated Image Discrimination

Conjunctival image discrimination was performed based on a previously reported fine structure image analysis method (19), using a customized algorithm written in MATLAB (Release 2015b, MathWorks, Inc., Natick, MA, USA). The motivation for the method is the long and successful history of time series analysis (TSA) in being able to

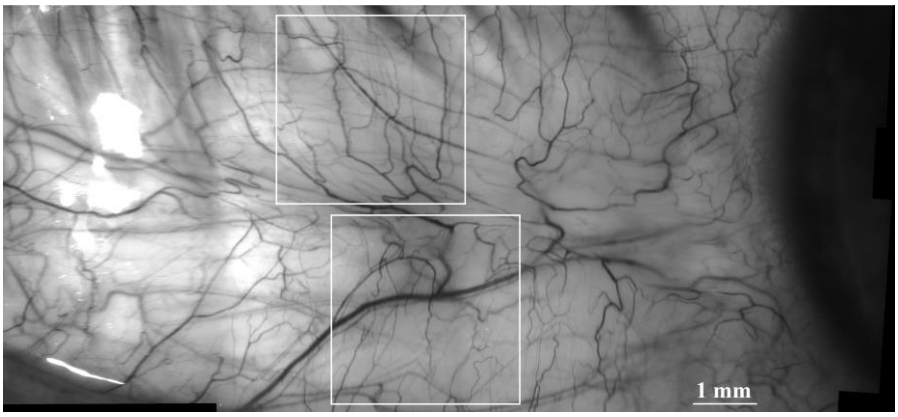

Figure 5.1.1. An example of a cropped mosaic image of the conjunctiva of a diabetic (PDR) subject. Regions with light illumination artifacts and blur are visualized. Two 3.1 mm×3.1 mm regions of interest (ROIs) that were selected for analysis are outlined by squares.

rigorously model multiple time series data which are visually indistinguishable (144). The mathematical basis of TSA is ordinary differential equations identified by applying OLS regression to difference equation approximations (145). It is shown in (19), that images can be considered as solutions to partial difference equations such as the general autoregressive one given in Equation (5.1.1). Further, it is shown that a Kronecker matrix-to-vector transformation applied to Equation (5.1.1) results in an OLS format of the equation to which TSA can be applied (45). Briefly, pixels of each conjunctival ROI were shifted by 1 or 2 pixels row-wise, column-wise, and along the diagonal to yield 8 unique combinations of the original image. Shifting the pixels allows evaluation of fluctuation in intensity values over a pixel's neighborhood. Since these shifts are at most 2 pixels out of a thousand, each image appears visually identical, quite analogous to the TSA visual experience. Each of the shifted images was vectorized by stacking columns

of the 2D image into a 1D vector which occupied one column of a matrix. A new column of ones was incorporated to the foremost left column of this matrix to account for sample means which improved discrimination because it removes the parameter estimation bias attributable to a nonzero sample mean (144). The model image was defined as the weighted sum of shifted images, as shown in Equation (5.1.1).

$$y_{i,j} = \sum_{k=0}^{2} \sum_{l=0}^{2} b_{k,l} y_{i-k,j-l} + u_{i,j} \quad (5.1.1)$$

where $y_{i,j}$ is the modeled image, $y_{i-k,j-l}$ are the shifted images, b_{kl} are coefficients to be estimated, and $u_{i,j}$ is a 2D random process error with zero mean. The OLS regression was performed to compute coefficients b_{kl} by minimizing the variance of $u_{i,j}$. If y_0 is the vectorized matrix $y_{i,j}$ and $X = [x_0\ x_1 \ldots\ x_8]$ a matrix of vectorized $y_{i-k,j-l}$ shifted images and x_0 a columns of ones, then the vector b of b_{kl} parameters can be determined as shown in Equation (5.1.2).

$$b = (X^T X)^{-1} X^Y y_0 \quad (5.1.2)$$

Computed OLS coefficients for images in each group of size N_i, i = NC, NDR, NPDR, and PDR were assembled into matrices (of size N_i subjects by 9 estimated b_{kl} parameters) to be use for discrimination. For every 2 groups of subjects, FLD was employed to compute a projection vector (v) which projects b_{kl} parameters of each image onto a scalar z-projection axis. The maximum separation of sample means of projections was obtained with v which satisfied the FLD eigenvector identity (46). For 2 comparison groups of images, N_1 and N_2 subjects, let their respective OLS coefficients be assembled in matrices B_1 and B_2. The "pooled sample" or combined matrix B_p is B_1 stacked on B_2. For an n by k matrix B with n samples of k parameters let B_m be B with its column

sample means subtracted. Then the estimated covariance matrix of B is $\Omega=B_m^T B_m/(n-1)$. The optimizing projection vector v satisfies the eigenvector identity of the B_1, B_2, and B_p covariance matrices was computed using Equation (5.1.3).

$$(n_1\Omega_p - n_2\Omega_1 - n_3\Omega_1)v = \Upsilon_1(n_2\Omega_1 + n_3\Omega_2)v \quad (5.1.3)$$

where γ_1 is the only non-zero eigenvalue, $n_1 = N_1+N_2-1$, $n_2 = N_1-1$, and $n_3 = N_2-1$. The FLD vector v maximizes the absolute difference between the sample means of 2 groups normalized by the sum of the covariance of each group.

The K-S test was used to verify that z-projections in each group were normally distributed (46), hence allowing the use of KLD statistics. KLD statistics are a special case of the Neyman-Pearson log-likelihood ratio hypothesis test. Applied to 2 normally distributed z-projection density functions, $f_1(z)$ and $f_2(z)$, for example as seen in Figure 5.1.2 through Figure 5.1.4, KLD statistics are values of a discrimination function L(z) given by Equation (5.1.4).

$$L_{1,2}(z) = \text{Ln}\left(\frac{f_1(z)}{f_2(z)}\right) = \text{Ln}\left(\frac{s_2}{s_1}\right) + \frac{(z-m_2)^2}{2s_2^2} - \frac{(z-m_1)^2}{2s_1^2} \quad (5.1.4)$$

where m_i and s_i, i = 1,2 are sample means and SD of the hypothesized z-projection distributions. If the 2 groups are perfectly separated, L1 values for all cases in group 1 will be positive and L2 values for all cases in group 2 will be negative and $L_{2,1}=-L_{1,2}$. Misclassified group 1 z-projections have negative L1 values and misclassified group 2 z-projections have positive L2 values. The larger L1 value is for a group 1 the more likely it is a true positive and the smaller L2 value is for a group 2 the more likely it is a true negative.

The automated method was applied to images obtained in 4 groups of subjects, namely, NC (group 1), NDR (group 2), NPDR (group 3), and PDR (group 4). This resulted in comparison of 6 group pairs. The discrimination rate of each group pair was calculated by the ratio of number of misclassifications to the total number of cases.

Image Discrimination Validation

Two tests were performed to establish the validity of the method. First, the effect of ROI selection on the discrimination rate was investigated by applying the method twice for discrimination of all group pairs, using 2 different non-overlapping ROIs for each subject. Second, a negative control test was performed by applying the discrimination method to subgroups of group 1 (NC). The subgroups (groups 1a and 1b) were created by randomly dividing the group 1 into 2 groups of equal size.

Human Observer Image Discrimination

Expert retinal specialists with experience in retinal vascular diseases served as human observers and performed image discrimination. The human observers were masked to the grouping of the subjects and the result of the automated discrimination method. They visually inspected images of the conjunctival microvasculature in paired groups and assigned each image to one of the 2 groups. The discrimination rates were calculated similar to the automated method.

Results

The K-S test verified normal distribution of z-projections in all groups ($p<0.0001$). Figure 5.1.2 shows probability densities of z-projections, and the KLD

statistics between non-diabetic and diabetic groups. Figure 5.1.2A, displays discrimination results between group 1 (NC) and group 2 (NDR). The automated method discrimination rate was 72% (28/39) with 4 and 7 misclassifications in group 1 and group 2, respectively. The range of L1 values for correctly discriminated cases in group 1 was between 0 and 2. The range of L2 values for correctly discriminated cases in group 2 was between -5 and 0. Figure 5.1.2B, displays discrimination results between group 1 (NC) and group 3 (NPDR). The automated method discrimination rate was 90% (35/39) with 2 misclassifications in each group. The range of L1 values for correctly discriminated cases in group 1 was between 0 and 9. The range of L3 values for correctly discriminated cases in group 3 was between -3 and 0. Figure 5.1.2C, displays discrimination results between group 1 (NC) and group 4 (PDR). The automated method discrimination rate was 95% (40/42) with 0 and 2 misclassifications in group 1 and group 4, respectively. The range of L1 values for correctly discriminated cases in group 1 was between 0 and 5. The range of L4 values for correctly discriminated cases in group 4 was between -11 and 0.

As listed in Table 5.1.1, using a second set of ROIs, the discrimination rates were 72%, 85%, and 93% between group 1 (NC) and group 2 (NDR) and between group 1 (NC) and group 3 (NPDR) and between group 1 (NC) and group 4 (PDR), respectively. The difference between discrimination rates determined using different ROIs was on average 2%. As expected, the discrimination rate was lowest between NC and NDR with no retinopathy, and highest between NC and PDR with the most advanced retinopathy.

Figure 5.1.3 shows probability densities of z-projections, and the KLD statistics between diabetic groups. Figure 5.1.3A, displays discrimination results between group 2 (NDR) and group 3 (NPDR). The automated method discrimination rate was 91% (31/34) with 1 and 2 misclassifications in group 2 and group 3, respectively. The range of L2 values for correctly discriminated cases in group 2 was between 0 and 6. The range of L3 values for correctly discriminated cases in group 3 was between -11 and 0. Figure 5.1.3B, displays discrimination results between group 2 (NDR) and group 4 (PDR). The automated method discrimination rate was 84% (31/37) with 2 and 4 misclassifications in group 2 and group 4, respectively. The range of L2 values for correctly discriminated cases in group 2 was between 0 and 4. The range of L4 values for correctly discriminated cases in group 4 was between -7 and 0. Figure 5.1.3C, displays discrimination results between group 3 (NPDR) and group 4 (PDR). The automated method discrimination rate was 95% (35/37) with 0 and 2 misclassifications in group 3 and group 4, respectively. The range of L3 values for correctly discriminated cases in group 3 was between 0 and 3. The range of L4 values for correctly discriminated cases in group 4 was between -23 and 0.

As listed in Table 5.1.1, using a second set of ROIs, the discrimination rates were 82%, 82%, and 97% between group 1 (NDR) and group 3 (NPDR) and between group 2 (NDR) and group 4 (PDR) and between group 3 (NPDR) and group 4 (PDR), respectively. The difference between discrimination rates determined using different ROIs was on average 4%.

Results of discrimination obtained by the negative control test in group 1a (NC) and group 1b (NC) is shown in Figure 5.1.4. The automated method discrimination rate was 54% (12/22) with 6 and 4 misclassifications in group 1a and group 1b, respectively. The range of L1a values for correctly discriminated cases in group 1a was between 0 and 4. The range of L1b values for correctly discriminated cases in group 1b was between -2 and 0.

Conjunctival image discrimination rates derived by the automated method and both human observers are summarized in Table 5.1.1. The 2 human observers' discrimination rates between NC and each of 3 diabetic groups, NDR, NPDR, and PDR, were 56% and 56%, 56% and 59%, and 45% and 67%, respectively. The human observers' discrimination rates comparing NDR with NPDR and NDR with PDR were 59% and 62% and 62% and 57%, respectively. Comparison of NPDR and PDR groups yielded discrimination rates of 59% and 54% for the 2 observers. The human observers' discrimination rates were on average 56% and 59%, meaning similar to discriminating images by chance. The discrimination rates derived by the automated method were consistently higher than those determined by both human observers.

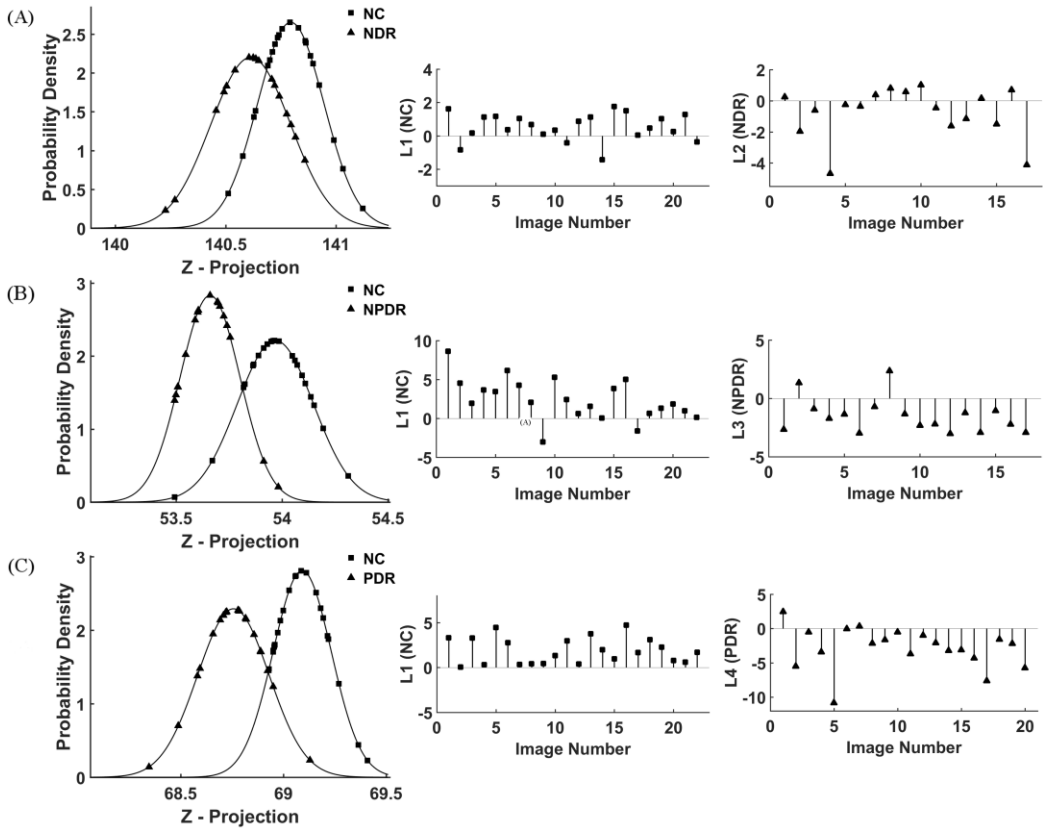

Figure 5.1.2. Probability densities of z-projections, and L1, L2, L3, and L4 values between non-diabetic subjects (NC, squares) and diabetic subjects (NDR, NPDR, and PDR, triangles). (A) NC group 1 and NDR group 2, (B) NC group 1 and NPDR group 3, (C) NC group 1 and PDR group 3. Misclassified cases in group 1 have negative L1 values and misclassified cases in groups 2, 3, and 4 have positive L2, L3 and L4 values, respectively. The larger L1 values and the smaller L2, L3 and L4 values denote more likely true positive and true negative cases, respectively.

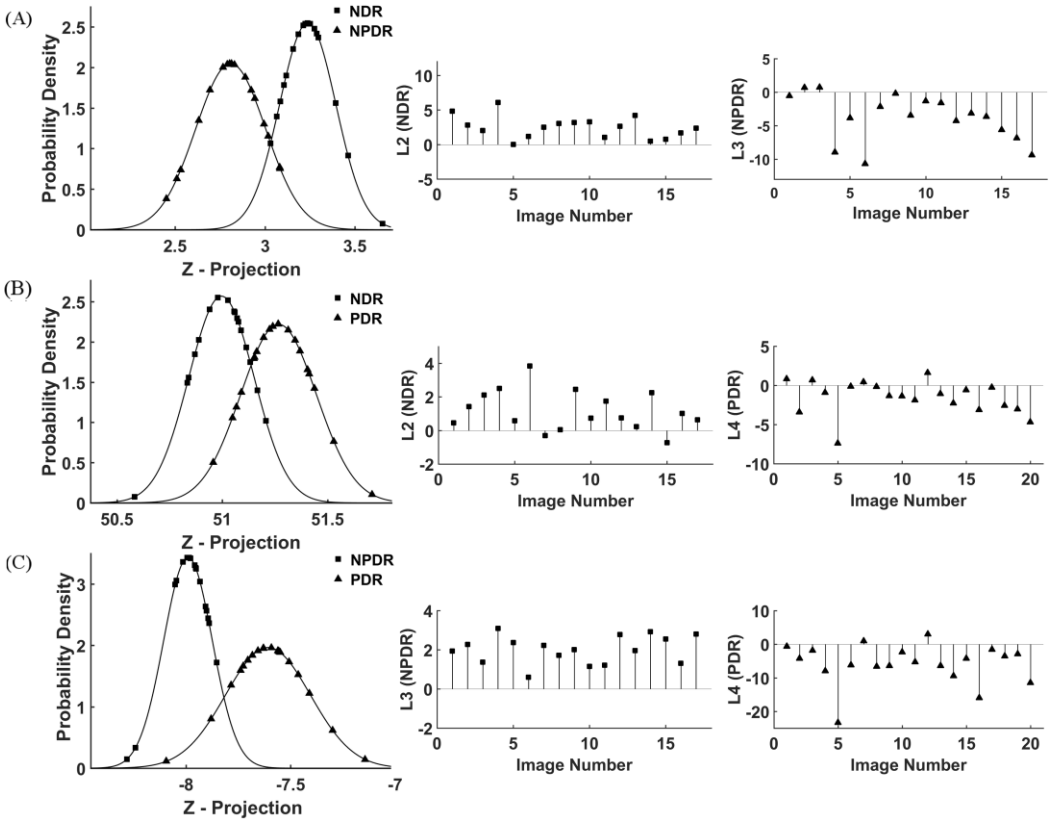

Figure 5.1.3. Probability densities of z-projections, and L2, L3, and L4 values between diabetic groups. (A) NDR group 2 (squares) and NPDR group 3 (triangles). Misclassified cases in groups 2 and 3 have negative L2 values and positive L3 values, respectively. (B) NDR group 2 (squares) and PDR group 4 (triangles). Misclassified cases in groups 2 and 4 have negative L2 values and positive L4 values, respectively. (C) NPDR group 3 (squares) and PDR group 4 (triangles). Misclassified cases in groups 3 and 4 have negative L3 values and positive L4 values, respectively. The larger L2 values denote more likely true positive cases and the smaller L3 and L4 values denote more likely true negative cases, except for comparison of groups 3 and 4, in which the larger L3 values denote more likely true positive cases.

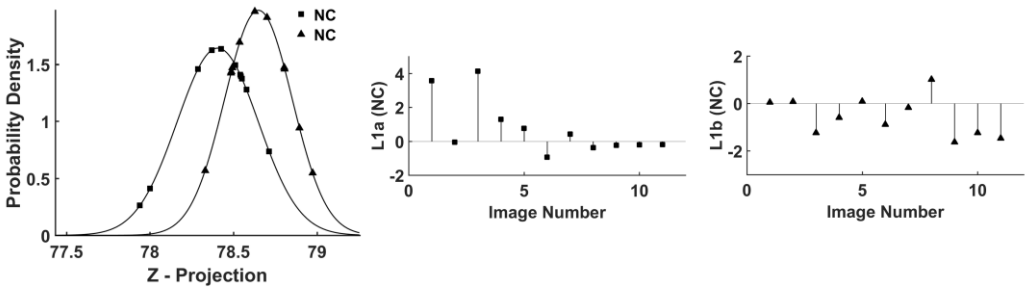

Figure 5.1.4. Probability densities of z-projections, and L1a, L1b values between non-diabetic groups. Images in NC subjects were randomly stratified into 2 groups of equal size, group 1a (squares) and group 1b (triangles). Misclassified cases in groups 1a and 1b have negative L1a values and positive L1b values, respectively. The larger L1a values and the smaller L1b values denote more likely true positive and true negative cases, respectively.

TABLE 5.1.1

DISCRIMINATION RATES DERIVED BY THE AUTOMATED METHOD AND BOTH HUMAN OBSERVERS.

Group Pairs	Total Number of Images	Discrimination Rate (%) Automated Method	Discrimination Rate (%) Human Observer
NC-NDR	39	72 (72[a])	56 (56[b])
NC-NPDR	39	90 (85[a])	56 (59[b])
NC-PDR	42	95 (93[a])	45 (67[b])
NDR-NPDR	34	91 (82[a])	59 (62[b])
NDR-PDR	37	84 (82[a])	62 (57[b])
NPDR-PDR	37	95 (97[a])	59 (54[b])
NC-NC	22	54	N/A

[a]Determined using a different set of selected ROIs.
[b]Determined by the second human observer.

Discussion

Assessment of the conjunctival microvasculature can potentially provide information about microvascular abnormalities due to systemic vascular diseases. In the current study, we demonstrated application of an automated method for discrimination of conjunctival microvasculature images according to stages of DR. Furthermore, quantitative assessment of the strength of discrimination (i.e. the likelihood that an image is correctly discriminated) was demonstrated using KLD statistics. The automated method was validated by first demonstrating the discrimination is independent of the selected ROIs, and second, by showing a considerably lower discrimination rate between 2 groups of control subjects.

The accuracy of discriminating PDR subjects was over 90% by the automated method, similar to the previously reported application of the method for classification of MRI between normal and demented brain (19). The discrimination rates of the automated method for clinical and non-clinical DR were over 80% and 70%, respectively. All automated discrimination rates were higher than rates determined by the human observers. The lower discrimination rate obtained by the human observer suggests that the automated method can identify alterations in the microvasculature undetected by a trained observer.

Since DR is a progressive microvascular disease, it is important to detect and monitor the presence of abnormalities at early stages of retinopathy. Current clinical techniques require dilated retinal exam by a specialist, which may not be accessible or affordable to many diabetic people. The availability of a non-invasive conjunctival

microvasculature imaging and an automated image analysis technique can be potentially useful for quick and frequent screening of subjects and referral to specialist for monitoring and treatment.

Previous studies have reported conjunctival microvascular alterations in diabetic subjects (16-18, 76, 109, 143). However, the current study is the first to our knowledge to apply a fine structure analysis method for discrimination of conjunctival microvasculature images according to DR stages. Compared to retinal examination, conjunctival imaging takes a few seconds, does not require pupil dilation, and is more cost efficient. Another advantage of the method is the rapid image analysis which required less than 4 seconds to analyze all images in the group pairs on a 1.3 GHz system with 8 GB RAM. This enables classification of very large image datasets.

The discrimination method detects global alterations that are not visually detectable in the microvascular network to determine the probability that an image belongs to a certain group. The method consists of in-depth mathematical and statistical analysis of pixel-by-pixel intensity variations in the entire image, enabling a computer-based discrimination to detect features and their pattern that may not be visually discernable by human observers. Considering each pixel as an independent variable, each image contains 10^6 features that can contribute to image classification. Therefore, the automated method of image discrimination is different from trained retinal specialists who examine the gross anatomy of blood vessels such as vessel dilation, obliteration, and increased tortuosity. For example, the method may detect features such as vessel wall thickening and stiffening which are not evident by visual inspection of images, but can

influence the results obtained by the automated discrimination method. Future studies by simulating specific microvasculopathies are needed to determine the image features that influence automated image discrimination rates. Additionally, the application of the method requires good conjunctival image quality which can be affected by eye movement and curvature. A potential solution is to incorporate a more rapid image acquisition system coupled with an autofocus lens. In the current study, there was a significant difference in age between NC and PDR subjects. Future studies are needed to determine the effects of age and other confounding factors on the discrimination results. Finally, further studies in larger sample sizes are needed to validate these preliminary results and also establish the sensitivity of the method for screening of DR subjects. Nevertheless, the findings of the current demonstrated the feasibility of successful application of an automated image analysis method to the conjunctival microvasculature images for discrimination of stages of DR. Due to the accessibility of conjunctiva for direct imaging, this method shows promise for DR screening and monitoring.

2. Discrimination of Subclinical Stage of Diabetic Retinopathy from Normal Controls Using Fine Structure Analysis of Retinal Fundus Images

Introduction

Diabetic retinopathy (DR) is the leading cause of vision loss among working age adults in the US and the EU (146, 147). A population-based study showed that the prevalence of DR in subjects with over 15 years of diabetes is over 97% (148). Although DR is a vision-threatening disease, its progression can be substantially controlled with early diagnosis, intensive glycemic management and other systemic treatments (149-151). Microaneurysms and dot hemorrhages are the earliest signs of DR by conventional clinical means. Nevertheless, the ocular therapeutics are generally administered after occurrence of damage and functional deficits to the retina (152, 153), which require advanced treatments such as laser, intravitreal steroid, intravitreal anti-VEGF or vitreous surgery (154). These treatments, however, carry risks (155). Therefore, it would be valuable to have less invasive treatments that can be used in earlier subclinical DR. By subclinical, we mean a stage in DR development when retinal alterations are present, but not detectable by direct visualization. Detection of retinal vascular alterations at this early stage can also prompt early, more intensive systemic treatment to prevent other complications such as renal disease, amputations, heart disease and neuropathy. Nevertheless, subclinical DR detection is challenging since there are no clinically visible signs to be used for diagnosis.

Computerized clinical DR detection by processing retinal images for detection of microvasculopathies such as microaneurysms, hemorrhages, hard exudates and leakage

have been proposed (156-159). Additionally, capillary drop out was shown to be a useful marker of early DR (160). In diabetic subjects without DR (NDR), capillary density and foveal avascular zone (FAZ) size alterations were reported (161). However, these findings were not detected in another study (162). Previous studies have also reported alterations in diameter, tortuosity, branching angles and length to diameter ratio of retinal vasculature in subclinical DR (154, 163). However, to the best of our knowledge, automatic subclinical DR detection based on retinal fundus images was not reported previously.

The usefulness of DR screening based on automated analysis of retinal vascular images for detection of abnormalities and their severity was reported previously (164). Therefore, development of automated techniques for detecting subclinical pathologies due to diabetes may also become valuable. Such a diagnosis allows early treatment and monitoring complications of the disease. Additionally, detection of retinal vascular alterations in subclinical DR can serve as a marker for presence of vascular disease through the body organs. In fact, diabetic-related microvascular alterations in various tissues such as brain, nail fold, retina, conjunctiva and sublingual have been reported previously (16, 98, 106, 165, 166). We showed in a previous study that fine structure analysis of conjunctival microvascular images can be useful for quantitative DR stage discrimination (83). Indeed, it was shown that the method is highly sensitive to changes such as vasodilation, vaso-obliteration, and vaso-constriction in the microvascular network (86). The purpose of the current study was to examine application of the fine structure analysis (19) for quantitative discrimination of subjects with subclinical DR from normal controls.

Materials and Methods

Image acquisition

An institutional review board of the University of Illinois at Chicago approved the current study. The study was explained to the subjects and informed consents were obtained in accordance to the declaration of Helsinki. A total of 33 subjects including 6 females and 27 males participated in the study. Subjects underwent a comprehensive clinical and retinal examination and were classified into non-diabetic control (NC; N=16) and diabetic without clinical retinopathy (NDR; N=17). Subjects' age (Mean±SD) were 56±9 years and 53±10 years in NC and NDR subjects, respectively (P=0.2).

Image acquisition and processing

Imaging was performed by a commercially available fundus camera system with a 60º field of view. Images were acquired in color and each one consisted of 2392×2048 pixels covering optic nerve head and the macula. A circular area of interest (ROI) with 3.6 mm (1000 pixels) radius centered on the fovea was selected from each fundus image and converted to grayscale for analysis. Selection of this area allowed analysis of consistent regions between the subjects and was based on the assumption that retinal vascular alterations in subclinical stage of DR are more likely to be detectable in smaller vessels and capillaries (154). Examples of selected ROIs outlined by a yellow circle overlaid on the fundus images and converted to grayscale of the ROIs in a NC and a NDR subject are shown in Figure 5.2.1.

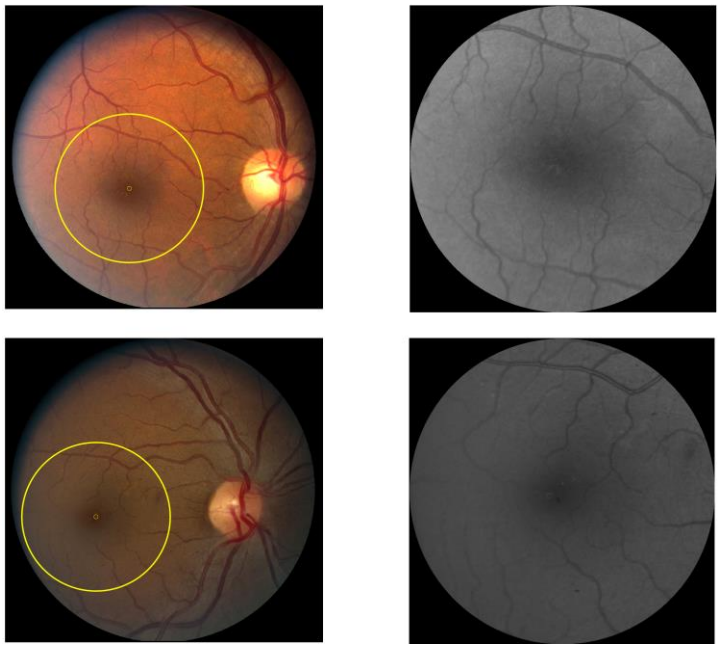

(A) **(B)**

Figure 5.2.1. (A) Examples of selected ROIs from fundus images of a NC (Top row) and a NDR (Bottom row) subject. A circular ROI with diameter of 3.6 mm centered on the fovea that was selected for discrimination analysis is outlined by a yellow circle (left column). (B) Converted grayscale images of the ROIs in the NC and NDR subjects.

Fundus image discrimination was performed by a previously described fine structure image analysis method using a custom algorithm written in MATLAB (Release 2015b, MathWorks, Inc., Natick, MA, USA) (19). Detail description of the method was published previously (19), and has been provided in chapter 5.1 of the current thesis. Similar to chapter 5.1, the discrimination rate was determined as percentage ratio of the number of correctly discriminated images to the total number of the images in the NC and NDR groups.

Human Observer Image Discrimination

An experienced retinal specialist masked to subjects' diagnosis and the result obtained by the automated discrimination served as human observer and performed image discrimination. Each of the images was visually inspected and assigned to one of the 2 groups. The discrimination rate for the human observer was calculated using the same formula as that used for the automated method.

Results

The K-S test results showed that the distribution of z-projects in NC and NDR subjects were normal ($P<0.001$). The automated discrimination rate was 88% (29/33) with 1 and 3 misclassifications in NC and NDR subjects, respectively. The KLD statistics between the NC and NDR subjects are shown in Figure 5.2.2. The range of L_1 values for correctly classified images in group 1 was between 0.1 and 4, while the range of L_2 values for correctly classified images in group 2 was between -0.2 and -6. Discrimination rate by the human observer between NC and NDR subjects was 45%.

Discussion

In the current study, application of an automated image discrimination method (19) based on fine structure analysis of retinal images was performed for quantitative subclinical DR discrimination. Additionally, the likelihood of accurate discrimination for each of the images in the 2 groups of subjects was demonstrated.

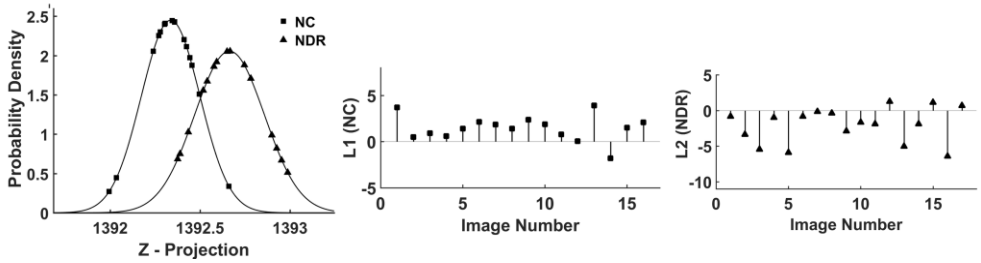

Figure 5.2.2. Probability density of z-projections, L_1 and L_2 values between non-diabet control (NC; group 1) and diabetic without retinopathy (NDR; group 2) subjects. Correctly classified images in group 1 had positive L_1 values, while correctly classified images in group 2 had negative (L_2) values. The larger L_1 value for an image in group and the smaller L_2 value for an image in group 2 are indicators of more likely true posit and more likely true negative discrimination, respectively.

The rate of subclinical DR discrimination using the automated technique was higher than the rate obtained by the human observer, suggesting that the method can detect retinal alterations which cannot be visualized by a trained observer. Detection of abnormalities in this early stage may prompt assessment of optimized glycemic control and possibly new treatment to prevent or delay DR progression. Moreover, these early stage alterations may suggest presence of abnormalities in other critical organs such as brain or heart. Thus, the method shows promises to improve monitoring and managing diabetic-related disorders throughout the body. Furthermore, early subclinical DR diagnosis can reduce the expenses by providing better disease management and precluding costly treatment due to progression of the disease.

DR is a progressive complication of diabetes that leads to blindness if not treated promptly (167). However micro and macro-maculopathies are usually present with

varying level of severity at the time of diagnosis (168). Therefore, comprehensive dilated retinal examination on a regular basis has been recommended for people with diabetes for early detection and treatment to avoid further complications. Changes in inter-capillary area, capillary density and FAZ size were shown to be correlated with progression of DR (154, 169, 170). Furthermore, retinal imaging by an adaptive optics system combined with a confocal scanning laser ophthalmoscope (171) showed a significant increase in tortuosity of retinal arteriovenous channels at subclinical DR (154). Additionally, previous studies have shown changes in retinal oxygenation, resistive index and blood flow in NDR subjects (169, 170, 172). These and other retinal physiological alterations can cause vasodilation, vessel wall stiffening, and mild tortuosity alterations in subclinical DR which may not be visually detected by traditional clinical evaluations. However, techniques such as the fine structure analysis which use all the information in the image rather than specific microvasculopathies can be useful for detecting subclinical DR.

We believe that shortly after diabetes, abnormalities begin to develop and reach a threshold over years manifested by DR. The fine structure analysis is highly sensitive to these early abnormalities, and hence provides early diagnosis on the course of the disease. Moreover, the KLD statistics provide quantitative representation of severity of abnormalities rather than only on an ordinal scale. Furthermore, the algorithm has the advantage of requiring short computational time (e.g. less than 5 seconds on a 1.3 GHz system with 8 GB RAM). High efficiency of the technique provides substantial potential for its application on very large image sets. In fact, the method can become useful for

subclinical DR detection in near future with the expected increase in prevalence of diabetes and shortage in the number of qualified screening health care providers (173).

It is important to note that it is unlikely that the fine structure method detects subclinical DR in early days of diabetes since diabetic-related abnormalities develop over time (174). It is probable that for some period there is no abnormality in the retina that can be picked by the method. In fact, conversion from normal to abnormal based on the fine structure analysis would be useful encouraging information for subjects to make extra effort to attain glycemic control.

In the current study, a region including retinal microvasculature in the macula was selected for analysis to include mostly smaller caliber vessels that are more vulnerable to the disease than the larger ones (154). Additionally, selection of this region allowed analysis of a consistent area among the subjects. In future, inclusion of different size retinal regions in the analysis can be useful for determining the effect of region on the discrimination rate. Furthermore, the effect of other pathologies such as hypertension that can be associated to diabetes was not considered in the current study. Future studies are warranted to assess the effects of present pathologies in addition to diabetes on the discrimination rate. Also, to further confirm the results of the current study, a future study with a larger number of subjects needs to be undertaken. Future longitudinal studies are also needed to determine the predictive value of the method. Nevertheless, the finding of the current convincingly showed potential for the fine structure analysis to detect subclinical DR based on retinal vascular images.

VI. A METHOD FOR QUANTITATIVE ASSESSMENT OF RETINAL VESSEL TORTUOSITY IN OPTICAL COHERENCE TOMOGRAPHY ANGIOGRAPHY APPLIED TO SICKLE CELL RETINOPATHY

The contents of this chapter have been published as: Maziyar M. Khansari, William O'Neill, Jennifer Lim and Mahnaz Shahidi. "Method for Quantitative Assessment of Retinal Vessel Tortuosity in Optical Coherence Tomography Angiography Applied to Sickle Cell Retinopathy." Biomedical Optics Express, 8(8), (2017): 3796-3806

Introduction

Sickle cell disease (SCD) is a genetic life-long chronic illness (175), characterized by sickle shape erythrocytes (176). Sickle cell retinopathy (SCR) is a major complication of SCD which is known to affect peripheral and macular retinal vascular beds and can lead to vision loss in the progressed stages due to focal nonperfusion and formation of new vessels (57, 177). Furthermore, frequent presence of retinal hemorrhages, schisis cavities and black sunbursts have been reported to be associated with SCR (57, 177).

Fluorescein angiography (FA) has been used as a gold standard in the past decades for clinical evaluation of microvasculopathy due to SCR (178). However, FA has been mainly performed for advanced proliferative stages of SCR and is known to be non-quantitative and invasive with limited applicability for subjects with small pupil (179). Previous studies using spectral domain optical coherence tomography in SCR

showed temporal and central macular thinning (180, 181), and indeed macular thinning was found to be associated with proliferative SCR (181). Lately, OCTA became available and offered an alternative to FA by providing high-resolution non-invasive imaging of capillary network in different retinal layers (182-184). Recent studies in SCR using OCTA in parafoveal regions showed microvasculopathies such as decreased superficial and deep retinal capillary density (48, 58, 178), enlarged foveal avascular zone (FAZ) (48, 178, 185), capillary non-perfused areas (178, 186) and disruption of the perifoveal anastomotic capillary arcade (178).

Tortuosity is an important geometric vessel parameter which has been considered as a risk factor of multiple retinal pathologies (26), and increased vessel tortuosity is known to be among the first microvascular alterations due to many retinopathies such as DR (27). In SCR, increased retinal vessels tortuosity has been observed, but not considered as a pathognomonic sign. Non-specific increased tortuosity has been reported in more than 32% of SCR subjects by qualitative analysis of large retinal vessels (187). Furthermore, increased tortuosity of major retinal vessels has been commonly observed in a majority of SCR subjects with HbS/HbS (SS) genotype (57, 58). Finally, a recent analysis of OCTA images of parafoveal regions showed vessel tortuosity is more sensitive than thickness for SCR detection (48).

There is no widely accepted mathematical definition for tortuosity (188), and tortuosity evaluation has been mainly performed subjectively by clinicians. However, sensitivity and repeatability of visual tortuosity evaluation is limited due to high inter-observer variability (47), and indeed qualitative evaluation is inefficient for large studies.

Quantitative assessment of tortuosity alterations has been reported in various retinal pathologies (27-30), using one or combination of distance measure (DM) (i.e. the ratio of vessel length to its chord length) (27, 28, 30, 48), curvature or integral of curvature (26, 29, 31, 49) and number of inflection points (33, 53). However, these methods are limited since they cannot always accurately estimate vessel tortuosity (26-31, 48, 53, 189-191), or are scale-dependent (33, 49). More recently, a measure of tortuosity based on slope chain coding (SCC) was proposed which is invariant to rigid transformations (192). However, as suggested in (193), SCC depends on length of linear elements which needs to be carefully selected for accurate tortuosity quantification.

In the current study, a method for assessment of retinal vessel touristy is proposed and shown to be invariant to rigid transformations and perform better than previous tortuosity metrics when compared with the evaluation of human observers. VTI does not require any parameter tuning, is computationally efficient and more sensitive to changes in vessel curvature than methods that rely only on DM. Additionally, OCTA images in both parafoveal and perifoveal regions were analyzed for detection of alterations in retinal vessel tortuosity due to SCR.

Materials and Methods

The study was approved by an institutional review board at University of Illinois at Chicago. Informed consents were obtained from subjects in accordance to the tenets of Declaration of Helsinki. The study was performed in 2 cohorts of subjects based on size of the imaged retinal region (i.e. 6 mm×6 mm (perifoveal); 3 mm×3 mm (parafoveal)). Perifoveal comprised 41 subjects (13 males and 28 females) with ages ranging from 15 to

62 years. Parafoveal comprised 10 subjects (5 males and 5 females) with ages ranging from 27 to 56 years. Based on a complete clinical history and ocular examination, subjects were categorized into 2 groups of NC (N=12; 7 OD and 5 OS) or SCR (N=29; 15 OD and 14 OS) in perifoveal region, and NC (N=5; 1 OD and 4 OS) or SCR (N=5; 3 OD and 2 OS) in parafoveal region. Three NC and 2 SCR subjects were in both cohorts. Subjects demographics and clinical data has been shown in Table 6.2. Exclusion criteria were inability to give informed consent or participate in the study, diabetes mellitus, glaucoma, or any other retinal disease. Each subject contributed data to the study by one eye with the best image quality.

Image acquisition

Imaging was performed by a commercially available OCTA instrument (Optovue Inc, Fremont, California, USA). The laser wavelength was 840±45 nm with an axial scan rate and axial scan depth resolution of 70 KHz and 5 µm, respectively. B scans were acquired from identical retinal locations to generate blood flow map based on motion of RBC. Each B-scan was comprised of 304 A scans. Images of the superficial retinal vessels and capillary network were generated in perifoveal (6 mm×6 mm) and parafoveal (3 mm×3 mm) regions centered on the fovea. The superficial layer was defined by the Optovue software and displayed the retinal vasculature in the nerve fiber and ganglion cell layers with minimal flow projection and shading effects.

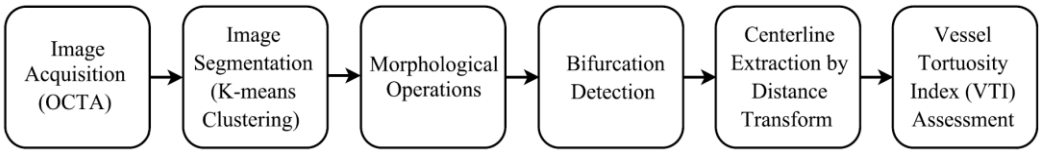

Figure 6.1. Flow chart depicting steps for VTI assessment in retinal vessels in OCTA.

Image processing and analysis

Assessment of superficial retinal vessel tortuosity was performed using several image-processing steps as shown in Figure 6.1. The algorithms were developed in MATLAB (Release 2015b, MathWorks, Inc., Natick, MA, USA) with image processing toolbox version 9.0.

Vessel segmentation

Segmentation of vessels in the perifoveal and the perifoveal regions in OCTA was performed using a k-means clustering algorithm (194), similar to a previous study in which human observers performed the classification based on Horton-Strahler schemes (195). K-means clustering is an iterative process for dividing data into k clusters where k is a positive integer. Clusters were found to minimize the least square error as shown in Equation (6.1).

$$E = \sum_{j=1}^{k} \sum_{x_i \in c_i} \|x_i - \mu_i\|^2 \quad (6.1)$$

where E is the error, x is intensity value of pixels, and μ is the centroid of clusters. The algorithm starts with K randomly selected initial centroids. The distance between intensity value of each pixel to the centroids was computed to assign the pixel to a cluster

with the closest centroid. A new set of clusters were computed in the next iteration based on assignment of pixels to the clusters in the previous one. This process was repeated to the point that the centroids were not changed between 2 consecutive iterations. The k-means clustering algorithm was used in the current study with k equals to 2 for classifying pixels either as vessel or background pixels to generate a binary image.

The binary image obtained from the k-means clustering was enhanced by a series of morphological operations. Filling was performed to eliminate any hole within the vessels, thickening was performed to bridge between separated vessel branches, objects smaller than 100 pixels, computed by counting the number of pixels in each binary object, were removed to eliminate noise and capillaries. Finally, dilation was performed using a disk shape structuring element to smooth vessel walls. Vessel centerlines between each pair of bifurcation points were extracted using distance transform through manual endpoint selection. The vessel endpoints were selected by simultaneous visualization of the grayscale and binary images in 2 separate windows. The grayscale image was used to identify bifurcations and the binary image was used to more accurately locate them with respect to the vessel boundaries and centerline. Cubic smoothing spline was utilized with a regularization parameter of 0.01 to obtain an adequate centerline and avoid aliasing. Vessel tortuosity index (VTI) was then computed for each of the centerlines as described in the following section.

Vessel tortuosity assessment

The most frequent tortuosity measures found in the literature were based on DM which is the ratio of arch length to chord length of a vessel segment (27-30). Despite the

fact that DM is a simple and quick approach for vessel tortuosity quantification, there are circumstances where it fails to accurately determine the tortuosity due to its simplicity (190). A tortuosity measure by combination of DM and number of inflection points was suggested by Bulliet *et al* (53), which was shown not always match with visual perception of tortuosity (33). Additionally, tortuosity density index (DT) defined as multiplication of number of inflection points with sum of DM determined between points of changes in centerline curvature was proposed by Grisan *et al* (33). The main drawback of this method was scale dependency.

Tortuosity measures based on curvature or integral of curvature have been proposed and applied in various pathologies (26, 31, 191). Hart *et al*, showed that the sum of squared curvatures along retinal vessel centerline perfectly match with tortuosity perception of experts for classifying their data set into tortuous and non-tortuous blood vessels (26). However, these methods can lead to misrepresentation of vessel tortuosity without considering changes in the sign of the curve, which is an important parameter used by clinicians for tortuosity evaluation (33).

Tortuosity assessment based on local angle changes was proposed previously (55, 56, 196). Grisan *et al*, showed limitation of these methods which computed the same tortuosity for a semi-circumference and a curve obtained by juxtaposition of its 2 arcs. The 2 have the same mean angle changes but different tortuosity.

A method based on SD of distribution of vessel centerline incremental lateral displacement was proposed earlier by Wenn *et al* (197). Nevertheless, their method does

not consider the magnitude of the curve, which plays an important role in clinical evaluation of vessel tortuosity.

Recently, Lisowaka *et al,* compared performance of 5 different retinal vessel tortuosity measures against sampling rates of vessel centerlines on a public data set (193). Performance comparison of DM (26), DT (33), SCC (193) and 2 curvature based measures (26) showed that the overall performance of DT was good, but not always the best. They suggested that attention to numerical details and standardization is essential before choosing a tortuosity index. Further details on available tortuosity measures is beyond the scope of the current study and can be found elsewhere (33, 190).

Comparatively little work has been conducted for quantitative assessment of retinal vessel tortuosity in OCTA. The VTI presented in the current study is sensitive to small changes in tortuosity, and hence is suitable for detecting tortuosity alterations in retinal vessels in OCTA. For each point along the centerline, the angle (θ) between a line tangent to the centerline and a reference axis was determined. SD of absolute θ values (SD_θ) along each centerline was computed, representing variation of local angle changes. The number of critical points at which the first derivative of centerlines vanishes (N) was quantified for each centerline based on frequency of changes in sign of the slope of the tangent lines. The N value was set to 1 for centerlines with no critical point to avoid zero tortuosity due to the lack of critical points. Inflection points at which the second derivative of centerlines vanishes (Ip) along the centerline were identified by detecting changes in the sign of curvature (k) where k was calculated using Equation (6.2). Magnitude of vessel centerline (M) was estimated as mean ratio of arch length (L_A) to

cord length (L_C) between pairs of inflection points including centerline end points as shown in Equation (6.3).

$$k(l) = \frac{\frac{dx(l)}{dl}\frac{d^2y(l)}{dl^2} - \frac{d^2x(l)}{dl^2}\frac{dy(l)}{dl}}{\left(\left(\frac{dx(l)}{dl}\right)^2 + \left(\frac{dy(l)}{dl}\right)^2\right)^{3/2}} \tag{6.2}$$

$$M = \frac{1}{Ip+2}\sum_{i=1}^{Ip+2}\frac{L_{Ai}}{L_{Ci}} \tag{6.3}$$

The tortuosity index was multiplied by vessel length (L_A) since L_A increases with tortuosity, and was normalized by vessel chord length (L_c) to allow comparison of vessel segments with variable chord length. The mathematical derivation and visual demonstration of VTI is given in Equation (6.4), and Figure 6.2, respectively.

$$VTI = \frac{0.1.SD_\theta.N.M.L_A}{L_C} \tag{6.4}$$

VTI is unitless similar to previous tortuosity metrics (26, 33, 193). The minimum value for VTI is equal to 0 for an ideal straight line with zero SD of local angle changes. In theory, there is no maximum value for VTI since it increases with higher variation in angles, number of critical points, and the magnitude of curve. However, VTI in OCTA was generally lower than 1. NC and SCR example of perifoveal OCTA, vessel segmentation, and extracted centerlines for tortuosity analysis are shown in Figure 6.3.

VTI Validation

VTI was validated by (i) using sinusoidal curves with variable magnitudes and angular frequencies, and (ii) by quantitative comparison against performance of human observers (MS, WO and MK).

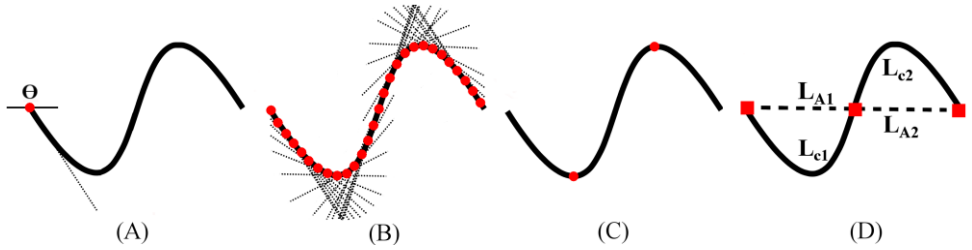

Figure 6.2. Visual demonstration of parameters extracted from a vessel centerline for VTI computation. (A) Angle between a line tangent to the centerline and a reference axis for the first centerline point. (B) Tangent lines for points along the centerline. SD of angles between each tangent line and the reference axis was computed. (C) Critical points (red circles) were determined based on changes in sign of slope of the tangent lines. (D) Magnitude of curve as ratio of arch length (L_A) to the chord length (L_C) between pairs of inflection points including centerline end points (red squares).

Two sets of sinusoidal curves were generated, the first set had constant angular frequency (1.25 rad/sec) and variable magnitudes between 0 and 6. The second set had constant magnitude of 1 and variable angular frequencies between 0 rad/sec and 6.3 rad/sec. A dependable tortuosity index should rise with increasing magnitude and increasing angular frequency coequal with visual perception of tortuosity.

Quantitative comparison of VTI and human observers' grading was performed using a set of 25 sinusoidal curves generated from randomly selected magnitudes between 0.1 and 5, and randomly selected angular frequencies between 0.6 rad/sec and 4 rad/sec. The random magnitudes and frequencies were generated using Mersenne Twister pseudo-random number generator (198). VTI and 4 previously established tortuosity indices, namely DI, T_{nl} (199), DM and integral of absolute curvature (T_c) were

computed for the curves and sorted in an ascending order. Similarly, human observers visually evaluated the curves and arranged them in an ascending order.

Statistical analysis

Statistical analysis was performed using SPSS (version 22, SPSS, Chicago, IL, USA) and statistical analysis codes written in MATLAB applied separately to data from the perifoveal and parafoveal regions. The association between VTI and performance of the human observers was determined using Spearman's rank correlation. Subjects' demographics were compared using Chi-square or t-test. Correlation between VTI and age in NC subjects was assessed using weighted Pearson's correlation analysis. Finally, generalized least squares (GLS) was used to determine the effect of disease (NC and SCR) on VTI with and without adjusting for covariates (age (continuous) and race (categorical)). Statistical significance was accepted at $P \leq 0.05$.

Results

VTI Validation

The validation tests using sinusoidal curves showed that VTI increased exponentially with increasing magnitudes and angular frequencies. The Spearman's rank correlation statistics for comparison of VTI and the 4 previous methods with performance of human observers is shown in Table 6.1. VTI was correlated better with all human observers' evaluations than tortuosity indices derived from previously established methods.

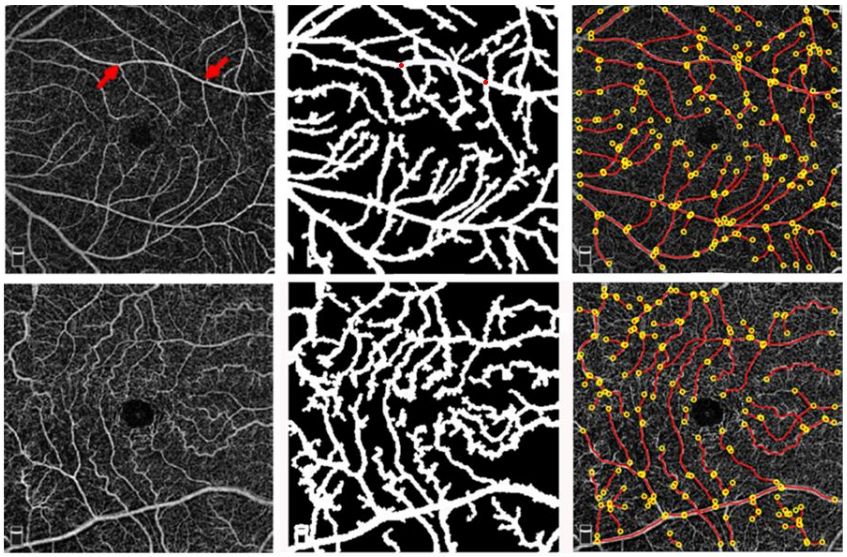

Figure 6.3. (A) OCTA images acquired in a NC (top row) and SCR (bottom row) subject in perifoveal regions. Example of a vessel segment endpoints is shown with red arrows (A; top row) (B) Vessel segmentation using k-means clustering. Example of a vessel segment endpoints selected on the binary image for centerline extraction are shown by red dots (B; top row). (C) Vessel endpoints (yellow circles) and centerlines (red lines) for VTI assessment. Mean VTI in the perifoveal region in the NC and SCR subjects were 0.41 and 0.71, respectively.

Demographic Data

Subjects' demographics are summarized in Table 6.2. In perifoveal region, age and eye examined were not different among NC and SCR subjects ($P \geq 0.3$), while sex and race were different ($P < 0.03$). In parafoveal, age, sex and eye examined were not different among NC and SCR subjects ($P \geq 0.2$), while race was different ($P = 0.008$).

TABLE 6.1

SPEARMAN'S RANK CORRELATION OF HUMAN OBSERVES VS 5 TORTUOSITY MEASURES FROM A SET OF 25 RANDOMLY GENERATED SINUSOIDAL CURVES. VTI (VESSEL TORTUOSITY INDEX), DENSITY INDEX (DI), NON-LINEAR CURVATURE (T_{NL}), DISTANCE MEASURE (DM), AND INTEGRAL OF ABSOLUTE CURVATURE (T_C).

Tortuosity Measure	Observer 1	Observer 2	Observer 3
VTI	0.89	0.91	0.93
DI	0.88	0.91	0.91
T_{nl}	0.88	0.86	0.90
DM	0.82	0.77	0.80
T_c	0.74	0.77	0.81

TABLE 6.2

SUBJECT'S DEMOGRAPHICS. M AND F ARE ABBREVIATIONS FOR MALE AND FEMALE, RESPECTIVELY. W, AA AND A STAND FOR WHITE, AFRICAN AMERICAN AND ASIAN, RESPECTIVELY. OD AND OS ARE RIGHT AND LEFT EYE, RESPECTIVELY. SS, SC, AND SB STAND FOR SICKLE CELL GENOTYPE HBS/HBS, HBS/HBC, AND HBS/BETA THALASSEMIA, RESPECTIVELY.

	Perifoveal			Parafoveal		
	NC (N=12)	SCR (N=29)	P-value	NC (N=5)	SCR (N=5)	P-value
Sex (M/F)	7/5	6/23	0.03[a]	3/2	2/3	0.9[a]
Race (W/AA/A)	11/0/1	0/29/0	<0.001[a]	4/0/1	0/5/0	0.008[a]
Eye (OD/OS)	7/5	15/14	0.7[a]	1/4	3/2	0.5[a]
Age (years)	37±12	35±14	0.3[b]	41±10	48±12	0.2[b]
SCR Type (SS/SC/Sβ)	17/9/3				2/2/1	
SCD Stage (O/I/II/III/IV)	1/1/19/7/1				0/0/3/1/1	

P-value determined by Chi-square ([a]) or t-test ([b]).

VTI in perifoveal and parafoveal regions

In the perifoveal region, VTI was assessed in 1026 and 2444 vessel segments in NC and SCR subjects, respectively. Mean VTI per subject ranged from 0.25 to 0.9 in perifoveal region. There was a negative correlation between VTI and age in NC subjects ($r=-0.4$, $P<0.001$, $N=12$). Finally, VTI was significantly higher in SCR (0.61 ± 0.11) than NC (0.31 ± 0.04) subjects with or without age and race adjustment ($P<0.001$).

In the parafoveal region, VTI was assessed in 181 and 154 vessel segments in NC and SCR subjects, respectively. Mean VTI per subject ranged from 0.3 to 0.9 in parafoveal region. Finally, VTI was significantly higher in SCR (0.69 ± 0.18) than NC (0.40 ± 0.04) subjects with or without age and race adjustment ($P\leq0.001$).

Discussion

In the current study, a quantitative vessel tortuosity index was formulated by extracting multiple parameters from vessel centerline. This method is similar to human observer's evaluation because variation of local angle changes, number of critical points, and magnitude of curve, each contribute to visual perception of tortuosity and were included in VTI formula. The method was applied to OCTA images obtained in perifoveal and parafoveal retinal regions and tortuosity alterations in superficial retinal vessels due to SCR were demonstrated.

VTI increased exponentially with higher magnitude and angular frequency of sinusoidal curves, consistent with visual perception of tortuosity. More importantly, VTI was shown to match with visual perception of tortuosity and its performance was better

than other commonly used methods such as DI and DM. Furthermore, VTI has several advantages for assessment of retinal microvasculature. First, it is invariant to rigid transformations such as translation, rotation, and scaling because these transformations have no influence on any of its components (SD_θ, N, M, L_A/L_c). This is important since rigid transformations are common in clinical applications in which different instruments with variable setting are used for image acquisition. Second, VTI was normalized with respect to chord length which is necessary for detection of tortuosity alterations in retinal tissue which is densely vascularized and contains vessels with variable lengths. Third, VTI incorporates vessel length which can contribute to tortuosity. In fact, retinal vessels can become tortuous due to longitudinal stretching or shortening of distance between their tethering points (26, 200). Although the pathophysiology of vascular stretching is not well established, the assumption is that the tone of smooth vascular muscles which determines vessel length and consequently tortuosity can be altered by mediators, blood gas and metabolism due to pathology (201).

The proposed and many previously established methods do not account for the influence of vessel caliber on tortuosity. Therefore, the findings may misrepresent tortuosity of the entire network since small caliber and highly tortuous vessels can increase the overall tortuosity of the network. Attempts have been made to consider vessel width information in retinal tortuosity quantification (49), and to detect type of tortuosity alteration in 3D models of intracerebral vessels (53). However, large clinical studies are required to determine the effect of vessel size on clinical perception of tortuosity to provide a deterministic weight factor to aggregate the impact of vessel size on tortuosity of the network. Although the effect of vessel caliber was not considered in

the VTI formula, the k-mean clustering algorithm used in the current study automatically eliminated capillaries with diameter smaller than 20 μm, and hence tortuosity was assessed in relatively larger size vessels within the network which are mainly evaluated by clinicians for detection of tortuosity alterations.

In the current study, increased retinal vessel tortuosity due to SCR was reported in perifoveal and parafoveal regions. This finding is in agreement with previous qualitative (57, 58, 187) and quantitative (48) reports of increased retinal vessels tortuosity in SCR. Despite the report of a moderate increase (17%) in tortuosity of parafoveal vessels (48), we found a marked increase in tortuosity in both the perifoveal (98%) and parafoveal (70%) regions. The difference in findings can be attributable to differences in techniques.

Retinal vessels tortuosity in the perifoveal region was negatively correlated with age in NC subjects, consistent with a previous study (32) that quantified tortuosity in major retinal arterioles and venules. This finding suggests that age has an independent effect on retinal vessel tortuosity and needs to be matched in future studies for detection of retinal tortuosity alterations.

There were some limitations in the current study. Accurate junction point (i.e. bifurcation and crossover) detection in retinal images is crucial for tortuosity evaluation since they define vessel course and their misdetection can result in inaccurate tortuosity measure. In the current study, a human observer (MK) visually inspected images and selected junction points. Despite FA and FP where bifurcation points can be more easily detected as shown in (202, 203), presence of numerous junction points and a dense

capillary network in OCTA increases complexity and decreases reliability of automatic junction point detection. Future research is warranted for developing methods for automatic junction point detection in OCTA which can improve the efficiency and increase repeatability of tortuosity assessment. Retinal arteries and veins were not separated since there is no reliable method to distinguish between them in OCTA. In fact, previous studies have shown that there is a difference in tortuosity of arteries and veins (32). Nevertheless, tortuosity measurements were averaged per subject in the current study to reduce variability due to vessel type. Additionally, we assumed the parameters used in the VTI formula had equal weight toward tortuosity and indeed the strong correlation between VTI and initiative perception of tortuosity further confirmed this hypothesis. Nevertheless, large clinical studies are useful to determine the effect of each parameter on visual perception of tortuosity and make adjustment if necessary. In the current study, the feasibility of application of the method was demonstrated in a relatively uniform population of subjects, predominately with SS genotype and stage II retinopathy. Future studies in larger cohorts of subjects are needed to investigate the effect of genotype and stage of SCR on tortuosity alterations. Additionally, future studies would be useful to investigate the relation of blood vessel tortuosity alterations with other retinal vascular and anatomical abnormalities detected by multimodal imaging (204).

Assessment of retinal vessel tortuosity alterations shows promise for clinical diagnostic evaluation and longitudinal monitoring of microvasculopathies due to SCR. Furthermore, the method presented in the current study can be potentially applied to microvascular images of other tissues for quantitative assessment of vessel tortuosity.

VII. CITED LITERATURE

1. Wanek, J., B. Gaynes, J.I. Lim, R. Molokie, and M. Shahidi, Human bulbar conjunctival hemodynamics in hemoglobin SS and SC disease. *American journal of hematology*, 2013. 88(8): p. 661-664.
2. Kord Valeshabad, A., J. Wanek, R. Zelkha, J.I. Lim, N. Camardo, B. Gaynes, and M. Shahidi, Conjunctival microvascular haemodynamics in sickle cell retinopathy. *Acta ophthalmologica*, 2015. 93(4).
3. Cheung, A.T., P.C. Chen, E.C. Larkin, P.L. Duong, S. Ramanujam, F. Tablin, and T. Wun, Microvascular abnormalities in sickle cell disease: a computer-assisted intravital microscopy study. *Blood*, 2002. 99(11): p. 3999-4005.
4. Paton, D., The conjunctival sign of sickle-cell disease: Further observations. *Archives of Ophthalmology*, 1962. 68(5): p. 627-632.
5. Smith, M.M., P.C. Chen, C.-S. Li, S. Ramanujam, and A.T. Cheung, Whole blood viscosity and microvascular abnormalities in Alzheimer's Disease. *Clinical hemorheology and microcirculation*, 2009. 41(4): p. 229-239.
6. To, W., V. O'Brien, A. Banerjee, A. Gutierrez, J. Li, P. Chen, and A. Cheung, Real-time studies of hypertension using non-mydriatic fundus photography and computer-assisted intravital microscopy. *Clinical hemorheology and microcirculation*, 2013. 53(3): p. 267-279.
7. Gaynes, B., P.Y. TENG, J. Wanek, and M. Shahidi, Feasibility of conjunctival hemodynamic measurements in rabbits: reproducibility, validity, and response to acute hypotension. *Microcirculation*, 2012. 19(6): p. 521-529.
8. Cheung, A.T., P.C. Chen, E. Miguelino, C.-S. Li, and S. Devaraj, Correlation of microvascular abnormalities and endothelial dysfunction in Type-1 Diabetes Mellitus (T1DM): a real-time intravital microscopy study. *Clinical hemorheology and microcirculation*, 2009. 42(4): p. 285-295.
9. Cheung, A.T., S. Ramanujam, D.A. Greer, L.F. Kumagai, and T.T. Aoki, Microvascular abnormalities in the bulbar conjunctiva of patients with type 2 diabetes mellitus. *Endocrine Practice*, 2001. 7(5): p. 358-363.
10. Duench, S., T. Simpson, L.W. Jones, J.G. Flanagan, and D. Fonn, Assessment of variation in bulbar conjunctival redness, temperature, and blood flow. *Optometry & Vision Science*, 2007. 84(6): p. 511-516.
11. Jiang, H., Y. Ye, D.C. DeBuc, B.L. Lam, T. Rundek, A. Tao, Y. Shao, and J. Wang, Human conjunctival microvasculature assessed with a retinal function imager (RFI). *Microvascular research*, 2013. 85: p. 134-137.
12. van Zijderveld, R., C. Ince, and R.O. Schlingemann, Orthogonal polarization spectral imaging of conjunctival microcirculation. *Graefe's Archive for Clinical and Experimental Ophthalmology*, 2014. 252(5): p. 773-779.

13. Shahidi, M., J. Wanek, B. Gaynes, and T. Wu, Quantitative assessment of conjunctival microvascular circulation of the human eye. *Microvascular research*, 2010. 79(2): p. 109-113.

14. Jiang, H., J. Zhong, D.C. DeBuc, A. Tao, Z. Xu, B.L. Lam, C. Liu, and J. Wang, Functional slit lamp biomicroscopy for imaging bulbar conjunctival microvasculature in contact lens wearers. *Microvascular research*, 2014. 92: p. 62-71.

15. Xu, Z., H. Jiang, A. Tao, S. Wu, W. Yan, J. Yuan, C. Liu, D.C. DeBuc, and J. Wang, Measurement variability of the bulbar conjunctival microvasculature in healthy subjects using functional slit lamp biomicroscopy (FSLB). *Microvascular research*, 2015. 101: p. 15-19.

16. To, W.J., D.G. Telander, M.E. Lloyd, P.C. Chen, and A.T. Cheung, Correlation of conjunctival microangiopathy with retinopathy in type-2 diabetes mellitus (T2DM) patients. *Clinical hemorheology and microcirculation*, 2011. 47(2): p. 131-141.

17. Cheung, A.T., A.R. Price, P.L. Duong, S. Ramanujam, J. Gut, E.C. Larkin, P.C. Chen, and D.M. Wilson, Microvascular abnormalities in pediatric diabetic patients. *Microvasc Res*, 2002. 63(3): p. 252-8.

18. Devaraj, S., A.T. Cheung, I. Jialal, S.C. Griffen, D. Nguyen, N. Glaser, and T. Aoki, Evidence of increased inflammation and microcirculatory abnormalities in patients with type 1 diabetes and their role in microvascular complications. *Diabetes*, 2007. 56(11): p. 2790-2796.

19. O'Neill, W., R. Penn, M. Werner, and J. Thomas, A theory of fine structure image models with an application to detection and classification of dementia. *Quantitative imaging in medicine and surgery*, 2015. 5(3): p. 356.

20. Lombardo, M., M. Parravano, S. Serrao, P. Ducoli, M. Stirpe, and G. Lombardo, Analysis of retinal capillaries in patients with type 1 diabetes and nonproliferative diabetic retinopathy using adaptive optics imaging. *Retina*, 2013. 33(8): p. 1630-1639.

21. Antal, B. and A. Hajdu, An ensemble-based system for microaneurysm detection and diabetic retinopathy grading. *IEEE transactions on biomedical engineering*, 2012. 59(6): p. 1720-1726.

22. Fleming, A.D., K.A. Goatman, S. Philip, G.J. Williams, G.J. Prescott, G.S. Scotland, P. McNamee, G.P. Leese, W.N. Wykes, and P.F. Sharp, The role of haemorrhage and exudate detection in automated grading of diabetic retinopathy. *British Journal of Ophthalmology*, 2010. 94(6): p. 706-711.

23. Bernardes, R., S. Nunes, I. Pereira, T. Torrent, A. Rosa, D. Coelho, and J. Cunha-Vaz, Computer-assisted microaneurysm turnover in the early stages of diabetic retinopathy. *Ophthalmologica*, 2009. 223(5): p. 284.

24. Abràmoff, M.D., J.C. Folk, D.P. Han, J.D. Walker, D.F. Williams, S.R. Russell, P. Massin, B. Cochener, P. Gain, and L. Tang, Automated analysis of retinal images

for detection of referable diabetic retinopathy. *JAMA ophthalmology*, 2013. 131(3): p. 351-357.

25. Cheung, C.Y.L., W. Hsu, M.L. Lee, J.J. Wang, P. Mitchell, Q.P. Lau, H. Hamzah, M. Ho, and T.Y. Wong, A new method to measure peripheral retinal vascular caliber over an extended area. *Microcirculation*, 2010. 17(7): p. 495-503.
26. Hart, W.E., M. Goldbaum, B. Côté, P. Kube, and M.R. Nelson, Measurement and classification of retinal vascular tortuosity. *International journal of medical informatics*, 1999. 53(2): p. 239-252.
27. Sasongko, M., T. Wong, T. Nguyen, C. Cheung, J. Shaw, and J. Wang, Retinal vascular tortuosity in persons with diabetes and diabetic retinopathy. *Diabetologia*, 2011. 54(9): p. 2409-2416.
28. Koreen, S., R. Gelman, M.E. Martinez-Perez, L. Jiang, A.M. Berrocal, D.J. Hess, J.T. Flynn, and M.F. Chiang, Evaluation of a computer-based system for plus disease diagnosis in retinopathy of prematurity. *Ophthalmology*, 2007. 114(12): p. e59-e67.
29. Hughes, A.D., E. Martinez-Perez, A.-S. Jabbar, A. Hassan, N.W. Witt, P.D. Mistry, N. Chapman, A.V. Stanton, G. Beevers, and R. Pedrinelli, Quantification of topological changes in retinal vascular architecture in essential and malignant hypertension. *Journal of hypertension*, 2006. 24(5): p. 889-894.
30. Gelman, R., M.E. Martinez-Perez, D.K. Vanderveen, A. Moskowitz, and A.B. Fulton, Diagnosis of plus disease in retinopathy of prematurity using Retinal Image multiScale Analysis. *Investigative ophthalmology & visual science*, 2005. 46(12): p. 4734-4738.
31. Smedby, Ö., N. Högman, S. Nilsson, U. Erikson, A.G. Olsson, and G. Walldius, Two-dimensional tortuosity of the superficial femoral artery in early atherosclerosis. *Journal of vascular research*, 1993. 30(4): p. 181-191.
32. Cheung, C.Y.-l., Y. Zheng, W. Hsu, M.L. Lee, Q.P. Lau, P. Mitchell, J.J. Wang, R. Klein, and T.Y. Wong, Retinal vascular tortuosity, blood pressure, and cardiovascular risk factors. *Ophthalmology*, 2011. 118(5): p. 812-818.
33. Grisan, E., M. Foracchia, and A. Ruggeri, A novel method for the automatic grading of retinal vessel tortuosity. *IEEE Transactions on Medical Imaging*, 2008. 27(3): p. 310-319.
34. Pavlou, A.T. and H.G. WOLFF, The bulbar conjunctival vessels in occlusion of the internal carotid artery. *AMA archives of internal medicine*, 1959. 104(1): p. 53-60.
35. Koutsiaris, A.G., Volume flow estimation in the precapillary mesenteric microvasculature in vivo and the principle of constant pressure gradient. *Biorheology*, 2005. 42(6): p. 479-491.
36. Koutsiaris, A.G., S.V. Tachmitzi, N. Batis, M.G. Kotoula, C.H. Karabatsas, E. Tsironi, and D.Z. Chatzoulis, Volume flow and wall shear stress quantification in

the human conjunctival capillaries and post-capillary venules in vivo. *Biorheology*, 2007. 44(5-6): p. 375-386.

37. Lee, J. and Y. Fung, Modeling experiments of a single red blood cell moving in a capillary blood vessel. *Microvascular research*, 1969. 1(3): p. 221-243.

38. Pries, A.R., T.W. Secomb, T. Gessner, M.B. Sperandio, J.F. Gross, and P. Gaehtgens, Resistance to blood flow in microvessels in vivo. *Circulation research*, 1994. 75(5): p. 904-915.

39. Alahi, A., R. Ortiz, and P. Vandergheynst. Freak: Fast retina keypoint. *in Computer vision and pattern recognition (CVPR), 2012 IEEE conference on*. 2012. Ieee.

40. Pournaras, C.J., E. Rungger-Brändle, C.E. Riva, S.H. Hardarson, and E. Stefansson, Regulation of retinal blood flow in health and disease. *Progress in retinal and eye research*, 2008. 27(3): p. 284-330.

41. Kolb, H., E. Fernandez, and R. Nelson, Webvision: The Organization of the Retina and Visual System. Salt Lake City (UT): University of Utah Health Sciences Center; 1995.

42. Saint-Geniez, M. and P.A. D'amore, Development and pathology of the hyaloid, choroidal and retinal vasculature. *International Journal of Developmental Biology*, 2004. 48(8-9): p. 1045-1058.

43. Anderson Jr, B., Ocular effects of changes in oxygen and carbon dioxide tension. *Transactions of the American Ophthalmological Society*, 1968. 66: p. 423.

44. Wong, T.Y., R. Klein, B.E. Klein, J.M. Tielsch, L. Hubbard, and F.J. Nieto, Retinal microvascular abnormalities and their relationship with hypertension, cardiovascular disease, and mortality. *Survey of ophthalmology*, 2001. 46(1): p. 59-80.

45. Magnus, J.R., Linear structures. *Griffin's statistical monographs and courses*, 1988(42).

46. Barton, D.E., *Biometrics*, 1963. 19(1): p. 194-196.

47. Kagan, A., E. Aureli, and J. Dobree, A note on signs in the fundus oculi and arterial hypertension: conventional assessment and significance. *Bulletin of the World Health Organization*, 1966. 34(6): p. 955.

48. Alam, M., D. Thapa, J.I. Lim, D. Cao, and X. Yao, Quantitative characteristics of sickle cell retinopathy in optical coherence tomography angiography. *Biomedical Optics Express*, 2017. 8(3): p. 1741-1753.

49. Bhuiyan, A., B. Nath, K. Ramamohanarao, R. Kawasaki, and T.Y. Wong, Automated analysis of retinal vascular tortuosity on color retinal images. *Journal of medical systems*, 2012. 36(2): p. 689-697.

50. Lotmar, W., A. Freiburghaus, and D. Bracher, Measurement of vessel tortuosity on fundus photographs. *Graefe's Archive for Clinical and Experimental Ophthalmology*, 1979. 211(1): p. 49-57.

51. Heneghan, C., J. Flynn, M. O'Keefe, and M. Cahill, Characterization of changes in blood vessel width and tortuosity in retinopathy of prematurity using image analysis. *Medical image analysis*, 2002. 6(4): p. 407-429.

52. Martinez-Perez, M.E., A. Highes, A.V. Stanton, S.A. Thorn, N. Chapman, A.A. Bharath, and K.H. Parker, Retinal vascular tree morphology: a semi-automatic quantification. *IEEE Transactions on Biomedical Engineering*, 2002. 49(8): p. 912-917.

53. Bullitt, E., G. Gerig, S.M. Pizer, W. Lin, and S.R. Aylward, Measuring tortuosity of the intracerebral vasculature from MRA images. *IEEE transactions on medical imaging*, 2003. 22(9): p. 1163-1171.

54. Patasius, M., V. Marozas, A. Lukosevicius, and D. Jegelevicius. Evaluation of tortuosity of eye blood vessels using the integral of square of derivative of curvature. *in EMBEC*. 2005.

55. Chandrinos, K., M. Pilu, R. Fisher, and P. Trahanias, Image processing techniques for the quantification of atherosclerotic changes. 1998: Department of Artificial Intelligence, University of Edinburgh.

56. Kheng, G., An automatic diabetic retinal image screening system book chapter in medical data mining and knowledge discovery. *Edited by Krzysztof Cios*, 2001. 29: p. 181-210.

57. Welch, R.B. and M.F. Goldberg, Sickle-cell hemoglobin and its relation to fundus abnormality. *Archives of ophthalmology*, 1966. 75(3): p. 353-362.

58. Han, I.C., M. Tadarati, and A.W. Scott, Macular vascular abnormalities identified by optical coherence tomographic angiography in patients with sickle cell disease. *JAMA ophthalmology*, 2015. 133(11): p. 1337-1340.

59. Ohtani, N., Laser Doppler flowmetry of the bulbar conjunctiva as a monitor of the cerebral blood flow. *[Zasshi][Journal]. Nihon Kyobu Geka Gakkai*, 1996. 44(9): p. 1721-1728.

60. Valeshabad, A.K., J. Wanek, F. Mukarram, R. Zelkha, F.D. Testai, and M. Shahidi, Feasibility of assessment of conjunctival microvascular hemodynamics in unilateral ischemic stroke. *Microvascular research*, 2015. 100: p. 4-8.

61. Schaser, K.-D., U. Settmacher, G. Puhl, L. Zhang, T. Mittlmeier, J. Stover, B. Vollmar, M. Menger, P. Neuhaus, and N. Haas, Noninvasive analysis of conjunctival microcirculation during carotid artery surgery reveals microvascular evidence of collateral compensation and stenosis-dependent adaptation. *Journal of vascular surgery*, 2003. 37(4): p. 789-797.

62. Cheung, A.T., R.V. Perez, and P.C. Chen, Improvements in diabetic microangiopathy after successful simultaneous pancreas-kidney transplantation: A computer-assisted intravital microscopy study on the conjunctival microcirculation1, 2. *Transplantation*, 1999. 68(7): p. 927-932.

63. Wang, L., J. Yuan, H. Jiang, W. Yan, H.R. Cintrón-Colón, V.L. Perez, D.C. DeBuc, W.J. Feuer, and J. Wang, Vessel Sampling and Blood Flow Velocity Distribution With Vessel Diameter for Characterizing the Human Bulbar Conjunctival Microvasculature. *Eye & contact lens*, 2016. 42(2): p. 135-140.

64. Frangi, A.F., W.J. Niessen, K.L. Vincken, and M.A. Viergever. Multiscale vessel enhancement filtering. *in International Conference on Medical Image Computing and Computer-Assisted Intervention*. 1998. Springer.

65. Lam, L., S.-W. Lee, and C.Y. Suen, Thinning methodologies-a comprehensive survey. *IEEE Transactions on pattern analysis and machine intelligence*, 1992. 14(9): p. 869-885.

66. A. Fong, Skeleton intersection detection. 2003: p. Available: http://www.mathworks.com/matlabcentral/fileexchange/

67. Pedersen, L., M. Grunkin, B. Ersbøll, K. Madsen, M. Larsen, N. Christoffersen, and U. Skands, Quantitative measurement of changes in retinal vessel diameter in ocular fundus images. *Pattern Recognition Letters*, 2000. 21(13): p. 1215-1223.

68. Bresenham, J.E., Algorithm for computer control of a digital plotter. *IBM Systems journal*, 1965. 4(1): p. 25-30.

69. Koutsiaris, A.G., Pulsatility Index quantification in the human precapillary arterioles of the eye. *Microvascular research*, 2016. 106: p. 36-38.

70. Koutsiaris, A.G., S.V. Tachmitzi, P. Papavasileiou, N. Batis, M.G. Kotoula, A.D. Giannoukas, and E. Tsironi, Blood velocity pulse quantification in the human conjunctival pre-capillary arterioles. *Microvascular research*, 2010. 80(2): p. 202-208.

71. Nagaoka, T. and A. Yoshida, Noninvasive evaluation of wall shear stress on retinal microcirculation in humans. *Investigative ophthalmology & visual science*, 2006. 47(3): p. 1113-1119.

72. Paparde, A., K. Nēringa-Martinsone, L. Plakane, and J.I. Aivars, Nail fold capillary diameter changes in acute systemic hypoxia. *Microvascular research*, 2014. 93: p. 30-33.

73. Dababneh, L., F. Cikach, L. Alkukhun, R.A. Dweik, and A.R. Tonelli, Sublingual microcirculation in pulmonary arterial hypertension. *Annals of the American Thoracic Society*, 2014. 11(4): p. 504-512.

74. Top, A.P., E.A. Buijs, P.H. Schouwenberg, M. van Dijk, D. Tibboel, and C. Ince, The microcirculation is unchanged in neonates with severe respiratory failure after the initiation of ECMO treatment. *Critical care research and practice*, 2012. 2012.

75. Dobbe, J.G., G.J. Streekstra, B. Atasever, R. Van Zijderveld, and C. Ince, Measurement of functional microcirculatory geometry and velocity distributions using automated image analysis. *Medical & biological engineering & computing*, 2008. 46(7): p. 659.

76. Owen, C.G., R.S. Newsom, A.R. Rudnicka, S.A. Barman, E.G. Woodward, and T.J. Ellis, Diabetes and the tortuosity of vessels of the bulbar conjunctiva. *Ophthalmology*, 2008. 115(6): p. e27-e32.

77. Kord Valeshabad, A., J. Wanek, F. Mukarram, R. Zelkha, F.D. Testai, and M. Shahidi, Feasibility of assessment of conjunctival microvascular hemodynamics in unilateral ischemic stroke. *Microvasc Res*, 2015. 100: p. 4-8.

78. Tamosuitis, T., A. Pranskunas, N. Balciuniene, V. Pilvinis, and E.C. Boerma, Conjunctival microcirculatory blood flow is altered but not abolished in brain dead patients: a prospective observational study. *BMC neurology*, 2016. 16(1): p. 1.

79. Schaser, K.D., U. Settmacher, G. Puhl, L. Zhang, T. Mittlmeier, J.F. Stover, B. Vollmar, M.D. Menger, P. Neuhaus, and N.P. Haas, Noninvasive analysis of conjunctival microcirculation during carotid artery surgery reveals microvascular evidence of collateral compensation and stenosis-dependent adaptation. *Journal of vascular surgery*, 2003. 37(4): p. 789-797.

80. Ditzel, J., Haemorheological factors in the development of diabetic microangiopathy. *The British journal of ophthalmology*, 1967. 51(12): p. 793-803.

81. Tarr, J.M., K. Kaul, M. Chopra, E.M. Kohner, and R. Chibber, Pathophysiology of diabetic retinopathy. *ISRN ophthalmology*, 2013. 2013.

82. Yin, L., Z. Yang, H. Yu, J. Qian, S. Zhao, J. Wang, X. Wu, J. Cahoon, and W. Tang, Changes in Sublingual Microcirculation is Closely Related with that of Bulbar Conjunctival Microcirculation in a Rat Model of Cardiac Arrest. *Shock (Augusta, Ga.)*, 2016. 45(4): p. 428-433.

83. Khansari, M.M., W. O'Neill, R. Penn, F. Chau, N.P. Blair, and M. Shahidi, Automated fine structure image analysis method for discrimination of diabetic retinopathy stage using conjunctival microvasculature images. *Biomedical Optics Express*, 2016. 7(7): p. 2597-2606.

84. Valek, M., F. Lopot, S. Dusilova-Sulkova, and V. Polakovic, Physiologic variability of vascular access blood flow for hemodialysis. *Blood purification*, 2008. 26(5): p. 468-472.

85. O'Connell, R.A., A.J. Anderson, S.L. Hosking, A.H. Batcha, and B.V. Bui, Test-retest reliability of retinal oxygen saturation measurement. *Optometry and Vision Science*, 2014. 91(6): p. 608-614.

86. Khansari, M.M., W. O'Neill, R. Penn, N.P. Blair, F. Chau, and M. Shahidi. An automated image processing method for classification of diabetic retinopathy stages from conjunctival microvasculature images. *in SPIE Medical Imaging*. 2017. International Society for Optics and Photonics.

87. Koutsiaris, A.G., S.V. Tachmitzi, and N. Batis, Wall shear stress quantification in the human conjunctival pre-capillary arterioles in vivo. *Microvascular research*, 2013. 85: p. 34-39.

88. Lowe, G., I. Ghafour, J. Belch, C. Forbes, W. Foulds, and A. MacCuish, Increased blood viscosity in diabetic proliferative retinopathy. *Diabetes research (Edinburgh, Scotland)*, 1986. 3(2): p. 67-70.

89. Davis, N., S. Katz, and J. Wylie-Rosett, The effect of diet on endothelial function. *Cardiology in review*, 2007. 15(2): p. 62-66.

90. Cohen, B.E., D. Edmondson, and I.M. Kronish, State of the art review: depression, stress, anxiety, and cardiovascular disease. *American journal of hypertension*, 2015. 28(11): p. 1295-1302.

91. Centers for Disease Control and Prevention, National diabetes statistics report: estimates of diabetes and its burden in the United States, 2014. 2014. *Atlanta (GA): US Department of Health and Human Services*, 2014.

92. Boyle, J.P., T.J. Thompson, E.W. Gregg, L.E. Barker, and D.F. Williamson, Projection of the year 2050 burden of diabetes in the US adult population: dynamic modeling of incidence, mortality, and prediabetes prevalence. *Population health metrics*, 2010. 8(1): p. 1.

93. Haffner, S.M., S. Lehto, T. Rönnemaa, K. Pyörälä, and M. Laakso, Mortality from coronary heart disease in subjects with type 2 diabetes and in nondiabetic subjects with and without prior myocardial infarction. *New England journal of medicine*, 1998. 339(4): p. 229-234.

94. Stehouwer, C.D., H.A. Fischer, A.W. Van Kuijk, B.C. Polak, and A.J. Donker, Endothelial dysfunction precedes development of microalbuminuria in IDDM. *Diabetes*, 1995. 44(5): p. 561-564.

95. Algenstaedt, P., C. Schaefer, T. Biermann, A. Hamann, B. Schwarzloh, H. Greten, W. Rüther, and N. Hansen-Algenstaedt, Microvascular alterations in diabetic mice correlate with level of hyperglycemia. *Diabetes*, 2003. 52(2): p. 542-549.

96. Squadrito, G. and D. Cucinotta, The late complications of diabetes mellitus. *Annali italiani di medicina interna: organo ufficiale della Societa italiana di medicina interna*, 1990. 6(1 Pt 2): p. 126-136.

97. American Diabetes Association, Diagnosis and classification of diabetes mellitus. *Diabetes care*, 2010. 33(Supplement 1): p. S62-S69.

98. Feke, G.T., H. Tagawa, A. Yoshida, D.G. Goger, J.J. Weiter, S.M. Buzney, and J.W. McMeel, Retinal circulatory changes related to retinopathy progression in insulin-dependent diabetes mellitus. *Ophthalmology*, 1985. 92(11): p. 1517-1522.

99. Lorenzi, M., G.T. Feke, E. Cagliero, L. Pitler, D.A. Schaumberg, F. Berisha, D.M. Nathan, and J.W. McMeel, Retinal haemodynamics in individuals with well-controlled type 1 diabetes. *Diabetologia*, 2008. 51(2): p. 361-364.

100. Bursell, S.E., A.C. Clermont, B.T. Kinsley, D.C. Simonson, L.M. Aiello, and H.A. Wolpert, Retinal blood flow changes in patients with insulin-dependent diabetes mellitus and no diabetic retinopathy. *Invest Ophthalmol Vis Sci*, 1996. 37(5): p. 886-97.

101. Cuypers, M.H., J.S. Kasanardjo, and B.C. Polak, Retinal blood flow changes in diabetic retinopathy measured with the Heidelberg scanning laser Doppler flowmeter. *Graefes Arch Clin Exp Ophthalmol*, 2000. 238(12): p. 935-41.

102. Grunwald, J.E., C.E. Riva, S.H. Sinclair, A.J. Brucker, and B.L. Petrig, Laser Doppler velocimetry study of retinal circulation in diabetes mellitus. *Archives of Ophthalmology*, 1986. 104(7): p. 991-996.

103. Rayman, G., A. Hassan, and J.E. Tooke, Blood flow in the skin of the foot related to posture in diabetes mellitus. *Br Med J (Clin Res Ed)*, 1986. 292(6513): p. 87-90.

104. Terry, E.N., E.J. Messina, M.S. Schwartz, W. Redisch, and J.M. Steele, Manifestation of diabetic microangiopathy in nailfold capillaries. *Diabetes*, 1967. 16(8): p. 595-7.

105. Tooke, J.E., D.D. Sandeman, and A.C. Shore, Microvascular hemodynamics in hypertension and diabetes. *J Cardiovasc Pharmacol*, 1991. 18 Suppl 2: p. S51-3.

106. Mooradian, A.D., Central nervous system complications of diabetes mellitus—a perspective from the blood–brain barrier. *Brain Research Reviews*, 1997. 23(3): p. 210-218.

107. Mcdonagh, P. and J.Y. Hokama, Microvascular perfusion and transport in the diabetic heart. *Microcirculation*, 2000. 7(3): p. 163-181.

108. Wahlqvist, M., I. Relf, K. Myers, and C. Lo, Diabetes and Macrovascular Disease: Risk Factors for Human Nutrition. *'Clinical Nutrition*, 1984. 38: p. 175-I84.

109. Stuebiger, N., W. Smiddy, J. Wang, H. Jiang, and D.C. DeBuc, Assesment of Conjunctival Microangiopathy in a Patient with Diabetes Mellitus Using the Retinal Function Imager. *Journal of clinical & experimental ophthalmology*, 2015. 6(1).

110. Burgansky-Eliash, Z., A. Barak, H. Barash, D.A. Nelson, O. Pupko, A. Lowenstein, A. Grinvald, and A. Rubinstein, Increased retinal blood flow velocity in patients with early diabetes mellitus. *Retina*, 2012. 32(1): p. 112-9.

111. Ditzel, J. and U. Sagild, Morphologic and Hemodynamic Changes in the Smaller Blood Vessels in Diabetes Mellitus: The Degenerative and Hemodynamic Changes in the Bulbar Conjunctiva of Normotensive Diabetic Patients. *New England Journal of Medicine*, 1954. 250(14): p. 587-594.

112. Margetis, P.I., M.H. Antonelou, I.K. Petropoulos, L.H. Margaritis, and I.S. Papassideri, Increased protein carbonylation of red blood cell membrane in diabetic retinopathy. *Experimental and molecular pathology*, 2009. 87(1): p. 76-82.

113. Owen, C.G., R.S. Newsom, A.R. Rudnicka, T.J. Ellis, and E.G. Woodward, Vascular response of the bulbar conjunctiva to diabetes and elevated blood pressure. *Ophthalmology*, 2005. 112(10): p. 1801-8.

114. Facemire, C.S., A.B. Nixon, R. Griffiths, H. Hurwitz, and T.M. Coffman, Vascular endothelial growth factor receptor 2 controls blood pressure by regulating nitric oxide synthase expression. *Hypertension (Dallas, Tex.: 1979)*, 2009. 54(3): p. 652-658.

115. Henry, T.D., B.H. Annex, G.R. McKendall, M.A. Azrin, J.J. Lopez, F.J. Giordano, P.K. Shah, J.T. Willerson, R.L. Benza, D.S. Berman, C.M. Gibson, A. Bajamonde, A.C. Rundle, J. Fine, E.R. McCluskey, and V. Investigators, The VIVA trial: Vascular endothelial growth factor in Ischemia for Vascular Angiogenesis. *Circulation*, 2003. 107(10): p. 1359-1365.

116. Citirik, M., N. Berker, H. Haksever, U. Elgin, and H. Ustun, Conjunctival impression cytology in non-proliferative and proliferative diabetic retinopathy. *International journal of ophthalmology*, 2014. 7(2): p. 321-325.

117. Schmid-Schönbein, H. and E. Volger, Red-cell aggregation and red-cell deformability in diabetes. *Diabetes*, 1975. 25(2 SUPPL): p. 897-902.

118. Chao, C.Y.L., Y.-P. Zheng, and G.L.Y. Cheing, The association between skin blood flow and edema on epidermal thickness in the diabetic foot. *Diabetes technology & therapeutics*, 2012. 14(7): p. 602-609.

119. Koutsiaris, A.G., Wall shear stress in the human eye microcirculation in vivo, segmental heterogeneity and performance of in vitro cerebrovascular models. *Clinical hemorheology and microcirculation*, 2015(Preprint): p. 1-20.

120. Ando, J. and K. Yamamoto, Vascular mechanobiology endothelial cell responses to fluid shear stress. *Circulation Journal*, 2009. 73(11): p. 1983-1992.

121. Cucullo, L., M. Hossain, V. Puvenna, N. Marchi, and D. Janigro, The role of shear stress in Blood-Brain Barrier endothelial physiology. *BMC neuroscience*, 2011. 12(1): p. 1.

122. Palmiotti, C.A., S. Prasad, P. Naik, K.M.D. Abul, R.K. Sajja, A.H. Achyuta, and L. Cucullo, In vitro cerebrovascular modeling in the 21st century: current and prospective technologies. *Pharmaceutical research*, 2014. 31(12): p. 3229-3250.

123. Jiang, Y., K. Kohara, and K. Hiwada, Low wall shear stress in carotid arteries in subjects with left ventricular hypertrophy. *American journal of hypertension*, 2000. 13(8): p. 892-898.

124. Zarins, C.K., M.A. Zatina, D.P. Giddens, D.N. Ku, and S. Glagov, Shear stress regulation of artery lumen diameter in experimental atherogenesis. *Journal of Vascular Surgery*, 1987. 5(3): p. 413-420.

125. Gibbons, G.H. and V.J. Dzau, The emerging concept of vascular remodeling. *New England Journal of Medicine*, 1994. 330(20): p. 1431-1438.

126. Nagaoka, T., E. Sato, A. Takahashi, H. Yokota, K. Sogawa, and A. Yoshida, Impaired retinal circulation in patients with type 2 diabetes mellitus: retinal laser Doppler velocimetry study. *Investigative ophthalmology & visual science*, 2010. 51(12): p. 6729-6734.

127. Irace, C., C. Carallo, A. Crescenzo, C. Motti, M.S. De Franceschi, P.L. Mattioli, and A. Gnasso, NIDDM is associated with lower wall shear stress of the common carotid artery. *Diabetes*, 1999. 48(1): p. 193-197.

128. Sheetz, M.J. and G.L. King, Molecular understanding of hyperglycemia's adverse effects for diabetic complications. *Jama*, 2002. 288(20): p. 2579-2588.

129. Horio, N., A. Clermont, A. Abiko, T. Abiko, B. Shoelson, S.-E. Bursell, and E. Feener, Angiotensin AT1 receptor antagonism normalizes retinal blood flow and acetylcholine-induced vasodiliation in normotensive diabetic rats. *Diabetologia*, 2004. 47(1): p. 113-123.

130. Ando, J., H. Tsuboi, R. Korenaga, Y. Takada, N. Toyama-Sorimachi, M. Miyasaka, and A. Kamiya, Shear stress inhibits adhesion of cultured mouse endothelial cells to lymphocytes by downregulating VCAM-1 expression. *American Journal of Physiology-Cell Physiology*, 1994. 267(3): p. C679-C687.

131. Miyahara, S., J. Kiryu, K. Yamashiro, K. Miyamoto, F. Hirose, H. Tamura, H. Katsuta, K. Nishijima, A. Tsujikawa, and Y. Honda, Simvastatin inhibits leukocyte accumulation and vascular permeability in the retinas of rats with streptozotocin-induced diabetes. *The American journal of pathology*, 2004. 164(5): p. 1697-1706.

132. Miyamoto, K., S. Khosrof, S.-E. Bursell, R. Rohan, T. Murata, A.C. Clermont, L.P. Aiello, Y. Ogura, and A.P. Adamis, Prevention of leukostasis and vascular leakage in streptozotocin-induced diabetic retinopathy via intercellular adhesion molecule-1 inhibition. *Proceedings of the National Academy of Sciences*, 1999. 96(19): p. 10836-10841.

133. McLeod, D.S., D.J. Lefer, C. Merges, and G.A. Lutty, Enhanced expression of intracellular adhesion molecule-1 and P-selectin in the diabetic human retina and choroid. *The American journal of pathology*, 1995. 147(3): p. 642.

134. Joussen, A.M., V. Poulaki, N. Mitsiades, B. Kirchhof, K. Koizumi, S. Döhmen, and A.P. Adamis, Nonsteroidal anti-inflammatory drugs prevent early diabetic retinopathy via TNF-α suppression. *The FASEB journal*, 2002. 16(3): p. 438-440.

135. Murray, C.D., The Physiological Principle of Minimum Work: I. The Vascular System and the Cost of Blood Volume. *Proc Natl Acad Sci U S A*, 1926. 12(3): p. 207-14.

136. Grauslund, J., A. Green, R. Kawasaki, L. Hodgson, A.K. Sjølie, and T.Y. Wong, Retinal vascular fractals and microvascular and macrovascular complications in type 1 diabetes. *Ophthalmology*, 2010. 117(7): p. 1400-1405.

137. Liew, G., J.J. Wang, N. Cheung, Y.P. Zhang, W. Hsu, M.L. Lee, P. Mitchell, G. Tikellis, B. Taylor, and T.Y. Wong, The retinal vasculature as a fractal:

methodology, reliability, and relationship to blood pressure. *Ophthalmology*, 2008. 115(11): p. 1951-1956. e1.

138. Azemin, M.Z.C., D.K. Kumar, T.Y. Wong, J.J. Wang, P. Mitchell, R. Kawasaki, and H. Wu, Age-related rarefaction in the fractal dimension of retinal vessel. *Neurobiology of Aging*, 2012. 33(1): p. 194. e1-194. e4.

139. Jia, Y., S.T. Bailey, T.S. Hwang, S.M. McClintic, S.S. Gao, M.E. Pennesi, C.J. Flaxel, A.K. Lauer, D.J. Wilson, and J. Hornegger, Quantitative optical coherence tomography angiography of vascular abnormalities in the living human eye. *Proceedings of the National Academy of Sciences*, 2015. 112(18): p. E2395-E2402.

140. Ishibazawa, A., T. Nagaoka, A. Takahashi, T. Omae, T. Tani, K. Sogawa, H. Yokota, and A. Yoshida, Optical coherence tomography angiography in diabetic retinopathy: a prospective pilot study. *American journal of ophthalmology*, 2015. 160(1): p. 35-44. e1.

141. Hwang, T.S., S.S. Gao, L. Liu, A.K. Lauer, S.T. Bailey, C.J. Flaxel, D.J. Wilson, D. Huang, and Y. Jia, Automated quantification of capillary nonperfusion using optical coherence tomography angiography in diabetic retinopathy. *JAMA ophthalmology*, 2016. 134(4): p. 367-373.

142. Zhang, M., J. Wang, A.D. Pechauer, T.S. Hwang, S.S. Gao, L. Liu, L. Liu, S.T. Bailey, D.J. Wilson, and D. Huang, Advanced image processing for optical coherence tomographic angiography of macular diseases. *Biomedical optics express*, 2015. 6(12): p. 4661-4675.

143. Worthen, D.M., B.M. Fenton, P. Rosen, and B. Zweifach, Morphometry of diabetic conjunctival blood vessels. *Ophthalmology*, 1981. 88(7): p. 655-657.

144. Box, J. and G.M. Jenkins, Reinsel. time series analysis, forecasting and control. *Tercera. NJ: Prentice Hall, Englewood Cliffs, NJ, USA*, 1994.

145. Draper, N. and H. Smith, Applied regression analysis. Series in probability and mathematical statistics. *Wiley*, 1981.

146. Abràmoff, M.D., J.M. Reinhardt, S.R. Russell, J.C. Folk, V.B. Mahajan, M. Niemeijer, and G. Quellec, Automated early detection of diabetic retinopathy. *Ophthalmology*, 2010. 117(6): p. 1147-1154.

147. Centers for Disease Control and Prevention, National diabetes fact sheet: national estimates and general information on diabetes and prediabetes in the United States, 2011. *Atlanta, GA: US Department of Health and Human Services, Centers for Disease Control and Prevention*, 2011. 201(1).

148. Klein, R., B.E. Klein, S.E. Moss, M.D. Davis, and D.L. DeMets, The Wisconsin Epidemiologic Study of Diabetic Retinopathy: II. Prevalence and risk of diabetic retinopathy when age at diagnosis is less than 30 years. *Archives of ophthalmology*, 1984. 102(4): p. 520-526.

149. Diabetes Control and Complications Trial Research, The effect of intensive treatment of diabetes on the development and progression of long-term complications in insulin-dependent diabetes mellitus. *N Engl j Med*, 1993. 1993(329): p. 977-986.

150. DCCT Research, and Group, Intensive diabetes therapy and ocular surgery in type 1 diabetes. *N Engl J Med*, 2015. 2015(372): p. 1722-1733.

151. Harper, C.A., J. O'Day, and H.R. Taylor, Early detection of diabetic retinopathy. *The Medical journal of Australia*, 1995. 162(10): p. 536-538.

152. Ho, A.C., I.U. Scott, S.J. Kim, G.C. Brown, M.M. Brown, M.S. Ip, and F.M. Recchia, Anti–vascular endothelial growth factor pharmacotherapy for diabetic macular edema: a report by the American Academy of Ophthalmology. *Ophthalmology*, 2012. 119(10): p. 2179-2188.

153. Early Treatment Diabetic Retinopathy Study Research, Treatment techniques and clinical guidelines for photocoagulation of diabetic macular edema: Early Treatment Diabetic Retinopathy Study report number 2. *Ophthalmology*, 1987. 94(7): p. 761-774.

154. Tam, J., K.P. Dhamdhere, P. Tiruveedhula, S. Manzanera, S. Barez, M.A. Bearse, A.J. Adams, and A. Roorda, Disruption of the retinal parafoveal capillary network in type 2 diabetes before the onset of diabetic retinopathy. *Investigative ophthalmology & visual science*, 2011. 52(12): p. 9257-9266.

155. Merani, R. and A.P. Hunyor, Endophthalmitis following intravitreal anti-vascular endothelial growth factor (VEGF) injection: a comprehensive review. *International journal of retina and vitreous*, 2015. 1(1): p. 9.

156. Niemeijer, M., B. Van Ginneken, J. Staal, M.S. Suttorp-Schulten, and M.D. Abràmoff, Automatic detection of red lesions in digital color fundus photographs. *IEEE Transactions on medical imaging*, 2005. 24(5): p. 584-592.

157. Niemeijer, M., B. Van Ginneken, M.J. Cree, A. Mizutani, G. Quellec, C.I. Sánchez, B. Zhang, R. Hornero, M. Lamard, and C. Muramatsu, Retinopathy online challenge: automatic detection of microaneurysms in digital color fundus photographs. *IEEE transactions on medical imaging*, 2010. 29(1): p. 185-195.

158. Staal, J., M.D. Abràmoff, M. Niemeijer, M.A. Viergever, and B. Van Ginneken, Ridge-based vessel segmentation in color images of the retina. *IEEE transactions on medical imaging*, 2004. 23(4): p. 501-509.

159. Zhang, B., F. Karray, Q. Li, and L. Zhang, Sparse Representation Classifier for microaneurysm detection and retinal blood vessel extraction. *Information Sciences*, 2012. 200: p. 78-90.

160. Schottenhamml, J., E.M. Moult, S. Ploner, B. Lee, E.A. Novais, E. Cole, S. Dang, C.D. Lu, L. Husvogt, and N.K. Waheed, An Automatic, Intercapillary Area-based Algorithm For Quantifying Diabetes-related Capillary Dropout Using Optical Coherence Tomography Angiography. *Retina*, 2016. 36: p. S93-S101.

161. Talisa, E., A.T. Chin, M.A. Bonini Filho, M. Adhi, L. Branchini, D.A. Salz, C.R. Baumal, C. Crawford, E. Reichel, and A.J. Witkin, Detection of microvascular changes in eyes of patients with diabetes but not clinical diabetic retinopathy using optical coherence tomography angiography. *Retina*, 2015. 35(11): p. 2364-2370.

162. Goudot, M.M., A. Sikorav, O. Semoun, A. Miere, C. Jung, B. Courbebaisse, M. Srour, J.G. Freiha, and E.H. Souied, Parafoveal OCT Angiography Features in Diabetic Patients without Clinical Diabetic Retinopathy: A Qualitative and Quantitative Analysis. *Journal of Ophthalmology*, 2017. 2017.

163. Sasongko, M.B., J.J. Wang, K.C. Donaghue, N. Cheung, P. Benitez-Aguirre, A. Jenkins, W. Hsu, M.-L. Lee, and T.Y. Wong, Alterations in retinal microvascular geometry in young type 1 diabetes. *Diabetes care*, 2010. 33(6): p. 1331-1336.

164. Prentašić, P. and S. Lončarić, Detection of exudates in fundus photographs using deep neural networks and anatomical landmark detection fusion. *Computer Methods and Programs in Biomedicine*, 2016. 137: p. 281-292.

165. SI, X.-m., J.-h. TAN, M.-y. GAO, C.-c. WANG, D. SHI, and S. SHI, Clinical significance of sublingual vein in patients with diabetes mellitus. *Liaoning Journal of Traditional Chinese Medicine*, 2008. 7: p. 006.

166. Rayman, G., A. Hassan, and J. Tooke, Blood flow in the skin of the foot related to posture in diabetes mellitus. *Br Med J (Clin Res Ed)*, 1986. 292(6513): p. 87-90.

167. Kollias, A.N. and M.W. Ulbig, Diabetic retinopathy: early diagnosis and effective treatment. *Deutsches Arzteblatt International*, 2010. 107(5): p. 75.

168. Shashank, R.J., A. Das, V. Vijay, and V. Mohan, Challenges in diabetes care in India: sheer numbers, lack of awareness and inadequate control. *Journal of Association of Physicians of India*, 2008. 56(6): p. 443-450.

169. Geyer, O., M. Neudorfer, T. Snir, M. Goldstein, T. Rock, D.M. Silver, and E. Bartov, Pulsatile ocular blood flow in diabetic retinopathy. *Acta Ophthalmologica Scandinavica*, 1999. 77(5): p. 522-525.

170. Dimitrova, G., S. Kato, Y. Tamaki, H. Yamashita, M. Nagahara, M. Sakurai, S. Kitano, and H. Fukushima, Choroidal circulation in diabetic patients. *Eye*, 2001. 15(5): p. 602-607.

171. Tam, J., J.A. Martin, and A. Roorda, Noninvasive visualization and analysis of parafoveal capillaries in humans. *Investigative ophthalmology & visual science*, 2010. 51(3): p. 1691-1698.

172. Khoobehi, B., K. Firn, H. Thompson, M. Reinoso, and J. Beach, Retinal arterial and venous oxygen saturation is altered in diabetic patientsretinal oxygen saturation trend in diabetes. *Investigative ophthalmology & visual science*, 2013. 54(10): p. 7103-7106.

173. Bethesda, M., National institute of diabetes and digestive and kidney diseases. *National Diabetes Statistics*, 2007.

174. Riddle, M.C., The transition from oral agents to combination insulin/oral therapy. *Type 2 Diabetes Mellitus*, 2008: p. 169-181.

175. Serjeant, G.R. and B.E. Serjeant, Sickle cell disease. Vol. 3. 1992: Oxford university press New York.

176. Lei, H. and G.E. Karniadakis, Quantifying the rheological and hemodynamic characteristics of sickle cell anemia. *Biophysical journal*, 2012. 102(2): p. 185-194.

177. Fadugbagbe, A., R. Gurgel, C. Mendonca, R. Cipolotti, A. dos Santos, and L. Cuevas, Ocular manifestations of sickle cell disease. *Annals of tropical paediatrics*, 2010. 30(1): p. 19-26.

178. Minvielle, W., V. Caillaux, S.Y. Cohen, F. Chasset, O. Zambrowski, A. Miere, and E.H. Souied, Macular microangiopathy in sickle cell disease using optical coherence tomography angiography. *American journal of ophthalmology*, 2016. 164: p. 137-144. e1.

179. Spaide, R.F., J.M. Klancnik, and M.J. Cooney, Retinal vascular layers imaged by fluorescein angiography and optical coherence tomography angiography. *JAMA ophthalmology*, 2015. 133(1): p. 45-50.

180. Hoang, Q.V., F.Y. Chau, M. Shahidi, and J.I. Lim, Central macular splaying and outer retinal thinning in asymptomatic sickle cell patients by spectral-domain optical coherence tomography. *American journal of ophthalmology*, 2011. 151(6): p. 990-994. e1.

181. Murthy, R.K., S. Grover, and K.V. Chalam, Temporal macular thinning on spectral-domain optical coherence tomography in proliferative sickle cell retinopathy. *Archives of ophthalmology*, 2011. 129(2): p. 247-249.

182. Jia, Y., O. Tan, J. Tokayer, B. Potsaid, Y. Wang, J.J. Liu, M.F. Kraus, H. Subhash, J.G. Fujimoto, and J. Hornegger, Split-spectrum amplitude-decorrelation angiography with optical coherence tomography. *Optics express*, 2012. 20(4): p. 4710-4725.

183. Nagiel, A., S.R. Sadda, and D. Sarraf, A promising future for optical coherence tomography angiography. *JAMA ophthalmology*, 2015. 133(6): p. 629-630.

184. Lumbroso, B., D. Huang, Y. Jia, C.J. Chen, M. Rispoli, A. Romano, and N.K. Waheed, Clinical OCT Angiography Atlas. 2015: JP Medical Ltd.

185. Sanfilippo, C.J., M.A. Klufas, D. Sarraf, and I. Tsui, Optical coherence tomography angiography of sickle cell maculopathy. *Retinal Cases and Brief Reports*, 2015. 9(4): p. 360-362.

186. Chalam, K. and K. Sambhav, Optical coherence tomography angiography in retinal diseases. *Journal of ophthalmic & vision research*, 2016. 11(1): p. 84.

187. Emerson, G.G. and G.A. Lutty, Effects of sickle cell disease on the eye: clinical features and treatment. *Hematology/oncology clinics of North America*, 2005. 19(5): p. 957-973.

188. Annunziata, R., A. Kheirkhah, S. Aggarwal, P. Hamrah, and E. Trucco, A fully automated tortuosity quantification system with application to corneal nerve fibres in confocal microscopy images. *Medical image analysis*, 2016. 32: p. 216-232.

189. Wolffsohn, J.S., G.A. Napper, S.M. Ho, A. Jaworski, and T.L. Pollard, Improving the description of the retinal vasculature and patient history taking for monitoring systemic hypertension. *Ophthalmic and Physiological Optics*, 2001. 21(6): p. 441-449.

190. Kalitzeos, A.A., G.Y. Lip, and R. Heitmar, Retinal vessel tortuosity measures and their applications. *Experimental eye research*, 2013. 106: p. 40-46.

191. Hart, W.E., M. Goldbaum, B. Cote, P. Kube, and M.R. Nelson. Automated measurement of retinal vascular tortuosity. *in Proceedings of the AMIA Annual Fall Symposium*. 1997. American Medical Informatics Association.

192. Bribiesca, E., A measure of tortuosity based on chain coding. *Pattern Recognition*, 2013. 46(3): p. 716-724.

193. Lisowska, A., R. Annunziata, G.K. Loh, D. Karl, and E. Trucco. An experimental assessment of five indices of retinal vessel tortuosity with the RET-TORT public dataset. *in Engineering in Medicine and Biology Society (EMBC), 2014 36th Annual International Conference of the IEEE*. 2014. IEEE.

194. Hartigan, J.A., Clustering algorithms. 1975.

195. Wang, Q., S. Chan, J.Y. Yang, B. You, Y.X. Wang, J.B. Jonas, and W.B. Wei, Vascular density in retina and choriocapillaris as measured by optical coherence tomography angiography. *American journal of ophthalmology*, 2016. 168: p. 95-109.

196. Eze, C., R. Gupta, and D. Newman, A comparison of quantitative measures of arterial tortuosity using sine wave simulations and 3D wire models. *Physics in medicine and biology*, 2000. 45(9): p. 2593.

197. Wenn, C. and D. Newman, Arterial tortuosity. *Australasian physical & engineering sciences in medicine*, 1990. 13(2): p. 67-70.

198. Matsumoto, M. and T. Nishimura, Mersenne twister: a 623-dimensionally equidistributed uniform pseudo-random number generator. *ACM Transactions on Modeling and Computer Simulation (TOMACS)*, 1998. 8(1): p. 3-30.

199. Aghamohamadian-Sharbaf, M., H.R. Pourreza, and T. Banaee, A novel curvature-based algorithm for automatic grading of retinal blood vessel tortuosity. *IEEE journal of biomedical and health informatics*, 2016. 20(2): p. 586-595.

200. Dougherty, G. and J. Varro, A quantitative index for the measurement of the tortuosity of blood vessels. *Medical engineering & physics*, 2000. 22(8): p. 567-574.

201. Bracher, D., Changes in peripapillary tortuosity of the central retinal arteries in newborns. *Graefe's Archive for Clinical and Experimental Ophthalmology*, 1982. 218(4): p. 211-217.

202. Calvo, D., M. Ortega, M.G. Penedo, and J. Rouco, Automatic detection and characterisation of retinal vessel tree bifurcations and crossovers in eye fundus images. *Computer methods and programs in biomedicine*, 2011. 103(1): p. 28-38.

203. Tavakoli, M., R.P. Shahri, H. Pourreza, A. Mehdizadeh, T. Banaee, and M.H.B. Toosi, A complementary method for automated detection of microaneurysms in fluorescein angiography fundus images to assess diabetic retinopathy. *Pattern Recognition*, 2013. 46(10): p. 2740-2753.

204. Falavarjani, K.G., A.W. Scott, K. Wang, I.C. Han, X. Chen, M. Klufas, J.-P. Hubschman, S.D. Schwartz, S.R. Sadda, and D. Sarraf, Correlation Of Multimodal Imaging In Sickle Cell Retinopathy. *Retina*, 2016. 36: p. S111-S117.

VIII. STATEMENT OF FUNDING

The work in this thesis was supported by national institute of health (NIH) grants DK010439, EY017918 and EY001792; Senior Scientific (i.e. Dr. Mahnaz Shahidi) Investigator Award by Research to Prevent Blindness (RPB); an unrestricted departmental award from University of Illinois at Chicago, department of ophthalmology and visual sciences.

IX. APPENDIX

Copyright permissions for re-use of published material from journals of Scientific Reports-Nature, IEEE transaction on medical imaging (TMI) and Biomedical Optics Express (OSA) are included in the following.

RightsLink®

Home | Create Account | Help

Title: Automated Assessment of Hemodynamics in the Conjunctival Microvasculature Network
Author: Maziyar M. Khansari
Publication: Medical Imaging, IEEE Transactions on
Publisher: IEEE
Date: Feb. 2016

LOGIN
If you're a copyright.com user, you can login to RightsLink using your copyright.com credentials. Already a RightsLink user or want to learn more?

Thesis / Dissertation Reuse

The IEEE does not require individuals working on a thesis to obtain a formal reuse license, however, you may print out this statement to be used as a permission grant:

Requirements to be followed when using any portion (e.g., figure, graph, table, or textual material) of an IEEE copyrighted paper in a thesis:

1) In the case of textual material (e.g., using short quotes or referring to the work within these papers) users must give full credit to the original source (author, paper, publication) followed by the IEEE copyright line © 2011 IEEE.
2) In the case of illustrations or tabular material, we require that the copyright line © [Year of original publication] IEEE appear prominently with each reprinted figure and/or table.
3) If a substantial portion of the original paper is to be used, and if you are not the senior author, also obtain the senior author's approval.

Requirements to be followed when using an entire IEEE copyrighted paper in a thesis:

1) The following IEEE copyright/ credit notice should be placed prominently in the references: © [year of original publication] IEEE. Reprinted, with permission, from [author names, paper title, IEEE publication title, and month/year of publication]
2) Only the accepted version of an IEEE copyrighted paper can be used when posting the paper or your thesis on-line.
3) In placing the thesis on the author's university website, please display the following message in a prominent place on the website: In reference to IEEE copyrighted material which is used with permission in this thesis, the IEEE does not endorse any of [university/educational entity's name goes here]'s products or services. Internal or personal use of this material is permitted. If interested in reprinting/republishing IEEE copyrighted material for advertising or promotional purposes or for creating new collective works for resale or redistribution, please go to http://www.ieee.org/publications_standards/publications/rights/rights_link.html to learn how to obtain a License from RightsLink.

If applicable, University Microfilms and/or ProQuest Library, or the Archives of Canada may supply single copies of the dissertation.

BACK CLOSE WINDOW

Dear Maziyar M. Khansari,

Thank you for contacting The Optical Society.

For the use of material from [1] Maziyar M Khansari, William O'Neill, Richard Penn, Felix Chau, Norman P Blair, and Mahnaz Shahidi, "Automated fine structure image analysis method for discrimination of diabetic retinopathy stage using conjunctival microvasculature images," Biomed. Opt. Express 7, 2597-2606 (2016) and [2] Method for quantitative assessment of retinal vessel tortuosity in optical coherence tomography angiography applied to sickle cell retinopathy, (accepted for publication):

As long as the copyrighted material is included within the body, section or chapter, of the thesis, and is not posted separate from the thesis, OSA considers your requested use of its copyrighted materials to be permissible within the author rights granted in the Copyright Transfer Agreement submitted by the requester on acceptance for publication of his/her manuscript. It is requested that the **Author Accepted** (or preprint) version be the version included within the thesis and that a complete citation of the original material be included in any publication. This permission assumes that the material was not reproduced from another source when published in the original publication.

Let me know if you have any questions.

Kind Regards,

Rebecca Robinson

Rebecca Robinson

July 25, 2017

Authorized Agent, The Optical Society

X. VITA

NAME:	Maziyar Mohammadtalab Khansari
EDUCATION:	B.S., Electrical and Electronics Engineering, Azad University, Iran, 2010
	M.S., Electrical and Computer Engineering, University of Illinois at Chicago, Illinois, 2014
	Ph.D., Bioengineering, University of Illinois at Chicago, Illinois, 2017
TEACHING:	Departments of Bioengineering, University of Illinois at Chicago, Illinois, 2014
	Departments of Electrical and Electronics Engineering, University of Illinois at Chicago, Illinois, 2012-2014
HONORS:	CCTS Pre-Doctoral PECTS Scholarship, University of Illinois at Chicago, Illinois, 2016
	Graduate Council Travel Award and Student Travel Presenter's Award, University of Illinois at Chicago, Illinois, 2015 and 2017
	Designated Program Committee for the IEEE Conference on Technologies for Sustainability (SushTech 2017)
PEER REVIEWER:	Journal of Ophthalmic & Vision Research
	Journal of Artificial Intelligence & Data Mining
	International Workshops on Material Science & Mechanical Engineering
	Bioengineering Student Journal, University of Illinois at Chicago
MEMBERSHIPS:	Institute of Electrical and Electronics Engineering (IEEE)
	American Association for the Advancement of Science (AAAS)
	Society of Photographic Instrumentation Engineers (SPIE)
	Association for Research in Vision and Ophthalmology (ARVO)
	Engineers Without Borders USA (EWB)

ABSTRACTS:

Maziyar M. Khansari, Jennifer Lim and Mahnaz Shahidi, “A Method for Quantitative Assessment of Retinal Vessel Tortuosity Applied to Sickle Cell Retinopathy Tortuosity Imaged by Optical Coherence Tomography Angiography”. Association for Research in Vision and Ophthalmology (ARVO) , Baltimore, MD, 2017.

Maziyar M Khansari, William O’Neill, Richard Penn, Norman P. Blair, Felix Chau and Mahnaz Shahidi. “An automated image processing method for classification stages of diabetic retinopathy using conjunctival microvasculature images”. Society of Photographic Instrumentation Engineers (SPIE), Orlando, FL, 2017.

Maziyar M Khansari, Michael Robert Tan and Mahnaz Shahidi. "An image analysis method for conjunctival microvascular network oximetry." Association for Research in Vision and Ophthalmology (ARVO), Seattle, WA, 2016.

Maziyar M Khansari, Justin Wanek, Anthony E. Felder, Nicole Camardo, and Mahnaz Shahidi. "Automated assessment of hemodynamics in the conjunctival microvasculature network." Association for Research in Vision and Ophthalmology (ARVO), Denver, CO, 2015.

PUBLICATIONS:

Maziyar M Khansari, Justin Wanek, Anthony E. Felder, Nicole Camardo and Mahnaz Shahidi. "Automated assessment of hemodynamics in the conjunctival microvasculature network." IEEE transactions on medical imaging, 35, no. 2 (2016): 605-611.

Maziyar M Khansari, William O’Neill, Richard Penn, Felix Chau, Norman P. Blair and Mahnaz Shahidi. "Automated fine structure image analysis method for discrimination of diabetic retinopathy stage using conjunctival microvasculature images." Biomedical Optics Express 7, no. 7 (2016): 2597-2606.

Maziyar M Khansari, Justin Wanek, Michael Tan, Charlotte E. Joslin, Jacob K. Kresovich, Nicole Camardo, Norman P. Blair and Mahnaz Shahidi. "Assessment of Conjunctival Microvascular Hemodynamics in Stages of Diabetic Microvasculopathy." Scientific Reports 7 (2017).

Maziyar M Khansari, William O’Neill, Jennifer Lim and Mahnaz Shahidi. “Method for quantitative assessment of retinal

vessel tortuosity in optical coherence tomography angiography applied to sickle cell retinopathy.” Biomedical Optics Express 8, no. 8 (2017): 3796-3806.

Maziyar M Khansari, Lioudmila V. Sorokina, Prithviraj Mukherjee, Farrukh Mukhtar, Mostafa Rezazadeh Shirdar, Mahnaz Shahidi and Tolou Shokuhfar, “Classification of Hydrogels Based on Their Source: A Review and Application in Stem Cell Regulation”, JMOJ, (2017): 1-8.

Maziyar M Khansari, William O’Neill, Richard Penn, Norman P. Blair, and Mahnaz Shahidi. "Automated fine structure image analysis method for discrimination of non-diabetic retinopathy using fundus images." Ready for submission.

Maziyar M Khansari, Michael Tan, Norman P. Blair and Mahnaz Shahidi. "Inter-visit variability of conjunctival microvascular hemodynamics in healthy and subjects with diabetic retinopathy." Ready for submission.